Review article

A review of novel green adsorbents as a sustainable alternative for the remediation of chromium (VI) from water environments

Amna Anjum [a], Shaukat Ali Mazari [a,**], Zubair Hashmi [a], Abdul Sattar Jatoi [a], Rashid Abro [a], Abdul Waheed Bhutto [a], Nabisab Mujawar Mubarak [b,***], Mohammad Hadi Dehghani [c,d,e,*], Rama Rao Karri [b], Amir Hossein Mahvi [c,e], Simin Nasseri [c,d]

[a] Department of Chemical Engineering, Dawood University of Engineering and Technology, Karachi, 74800, Pakistan
[b] Petroleum and Chemical Engineering, Faculty of Engineering, Universiti Teknologi Brunei, Bandar Seri Begawan, BE1410, Brunei Darussalam
[c] Department of Environmental Health Engineering, School of Public Health, Tehran University of Medical Sciences, Tehran, Iran
[d] Center for Water Quality Research, Institute for Environmental Research, Tehran University of Medical Sciences, Tehran, Iran
[e] Institute for Environmental Research, Center for Solid Waste Research, Tehran University of Medical Sciences, Tehran, Iran

ARTICLE INFO

ABSTRACT

The presence of heavy metal, chromium (VI), in water environments leads to various diseases in humans, such as cancer, lung tumors, and allergies. This review comparatively examines the use of several adsorbents, such as biosorbents, activated carbon, nanocomposites, and polyaniline (PANI), in terms of the operational parameters (initial chromium (VI) concentration (C_o), temperature (T), pH, contact time (t), and adsorbent dosage) to achieve the Langmuir's maximum adsorption capacity (q_m) for chromium (VI) adsorption. The study finds that the use of biosorbents (fruit bio-composite, fungus, leave, and oak bark char), activated carbons (HCl-treated dry fruit waste, polyethyleneimine (PEI) and potassium hydroxide (KOH) PEI-KOH alkali-treated rice waste-derived biochar, and KOH/hydrochloric acid (HCl) acid/base-treated commercial), iron-based nanocomposites, magnetic manganese-multiwalled carbon nanotubes nanocomposites, copper-based nanocomposites, graphene oxide functionalized amino acid, and PANI functionalized transition metal are effective in achieving high Langmuir's maximum adsorption capacity (q_m) for chromium (VI) adsorption, and that operational parameters such as initial concentration, temperature, pH, contact time, and adsorbent dosage significantly affect the Langmuir's maximum adsorption capacity (q_m). Magnetic graphene oxide functionalized amino acid showed the highest experimental and pseudo-second-order kinetic model equilibrium adsorption capacities. The iron oxide functionalized calcium carbonate ($IO@CaCO_3$) nanocomposites showed the highest heterogeneous adsorption capacity. Additionally, Syzygium cumini bark biosorbent is highly effective in treating tannery industrial wastewater with high levels of chromium (VI).

* Corresponding author. Department of Environmental Health Engineering, School of Public Health, Tehran University of Medical Sciences, Tehran, Iran.
** Corresponding author.
*** Corresponding author.
E-mail addresses: shaukatmazari@gmail.com (S.A. Mazari), mubarak.yaseen@gmail.com (N.M. Mubarak), hdehghani@tums.ac.ir (M.H. Dehghani).

1. Introduction

Wastewater is becoming more challenging worldwide, especially in developing countries, due to rapid industrial and agricultural development, urbanization, and lifestyle changes [1–3]. Wastewater containing heavy metals is toxic, carcinogenic, and highly water-soluble, which originates from various sources such as fixing agents, metal complex dyes, pesticides, fertilizers, bleaching agents, mordants, pigments, etc. [4]. Moreover, heavy metals in wastewater and industrial effluents pose significant environmental concerns to human and marine life [5]. The heavy metals of the most concern [6] include chromium, nickel, mercury, lead, cadmium, zinc, arsenic, and copper, as represented in Fig. 1.

Chromium (Cr), a commonly known heavy metal, is extensively used in various applications such as chrome plating, catalysts, leather tanning, electroplating, glass industries, textile industries, petroleum refineries, wood preservation, etc. [7,8]. It is found in aqueous solution/industrial wastewater in two states - trivalent (Cr(III)) and hexavalent (Cr(VI)) [9]. Hexavalent chromium (Cr(VI)), which exists primarily as the chromate ion (CrO_4^{2-}), can penetrate the cellular membranes about 500–1000 times more effectively as compared to the Cr(III) [10,11]. For example, dyes containing several toxic heavy metals (especially chromium) are vigorously used in textile industries to impart color to the products/raw materials [12–14]. Examples of the various industries contributing to Cr(VI) pollution are summarized in Fig. 2 [15,16].

The discharge of industrial effluents from various sources containing Cr(VI) into the water bodies poses a risk to aquatic life because of its toxic and corrosive nature. It is quickly collected and bio-magnified in the species through fish [17]. It leads to an enhanced mortality rate, mucous secretion, scale erosion, discoloration, abnormal swimming and osmoregulatory function disruption in fishes [18,19]. Thus, Cr(VI) enters the terrestrial food chain and gets into humans through fish in extremely bio-magnified amounts. It poses various health-related issues like genotoxicity, liver damage, kidney damage, neurotoxicity, lung cancer, asthma, immunotoxicity, skin ulcers, mutagenic, teratogenic, and carcinogenic [20–25]. Furthermore, Cr(VI) is the cause of various health issues such as hepatopathy, skin irritation, lung cancer, and pulmonary congestion [26,27]. The rats reportedly undergo functional and structural abnormalities of the thyroid and pituitary glands due to Cr(VI) injection [28]. Thus, an effective technique for Cr(VI) remediation from wastewater should be adopted.

The international regulatory body "World Health Organization," commonly known as WHO, has set 50 μg L^{-1} as a Cr(VI) limit in drinking water to avoid endangered drinking water and human health [29]. Hence, developing effective technologies and strategies to remove Cr(VI) from wastewater is essential.

1.1. Conventional methods available for chromium removal

Like other heavy metals, Cr(VI) cannot be eliminated from the environment. However, the toxicity of Cr(VI) can be reduced using two approaches, i.e., reduction of Cr(VI) to the lesser toxic Cr(III) and reduction of the concentration of Cr(VI) by adsorption on an adsorbent surface. Moreover, both approaches can reduce the toxicity caused by Cr(VI). There are several conventional methods available for Cr(VI) remediation. Kalidhasan and co-authors reviewed these methods [30], shown in Table 1 [31–61].

1.2. Importance of adsorption and novel adsorbents

In past research, various techniques have been developed and reported in the literature for removing Cr(VI) from wastewater, such as ion exchange, solvent extraction, membrane-filtration, electrochemical method, physical and chemical precipitation, and
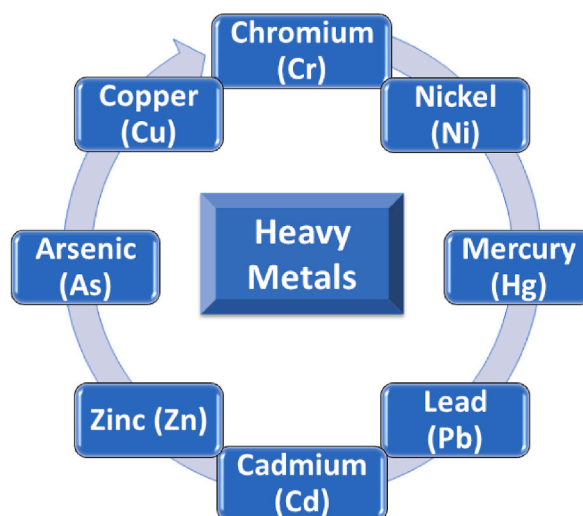

Fig. 1. Exhibition of primary heavy metals of concern.

adsorption [9,78–82]. Adsorption is the most commonly used technology to remove toxic pollutants from wastewater due to its simple design, easy operational conditions, and environmentally friendly approach [83–86], high effectiveness [87], broad applicability [88] and relatively economical [1,89]. Furthermore, it offers design flexibility and helps produce superior-quality treated effluent [90]. In addition, the adsorption process is invertible; hence, desorption can regenerate the adsorbents [86,91,92]. In the recent twenty years, several adsorbents have been extensively used to remove Cr(VI) from wastewater, such as activated carbon [93], mesoporous materials, metal and metal oxide, bio-adsorbents, polymer-based adsorbents [8,79,94–97], nano adsorbents [30], zeolite [31], chitosan [32] and biochar [33,34]. However, these adsorbents possess the drawbacks of lower adsorption efficiency. Thus, it is highly desirable to discover novel adsorbents with improved adsorption capacity [35,36].

This study focuses on the comparative analysis of the maximum adsorption capacity of various adsorbents such as biosorbents, biomass-derived activated carbon, nanocomposites, and PANI for chromium removal from the wastewater while observing the Langmuir adsorption isotherm. The homogeneity and heterogeneity of the adsorbent surfaces have been analyzed using the best fitting on Langmuir and Freundlich adsorption isotherm models. The adsorption kinetics modelling of chromium adsorption using different adsorbents has also been discussed to analyze adsorption dynamics. The effect of dosage, metal concentration, pH, temperature, and contact time on the Langmuir adsorption capacity has also been analyzed. The data has been compiled from various sources for this selective list of adsorbents.

2. Application of adsorption isotherms

Adsorption isotherms provide quality information related to the nature of the adsorbent interaction and the specified relation between the adsorbate (heavy metal) concentration and its degree of accumulation onto the adsorbent at a specific time temperature [98,99]. Hence, it can help optimize the use of adsorbents [98,99] and design purposes [99]. Several available adsorption isotherm models describe the equilibrium of adsorption, including Langmuir, Freundlich, Tempkin, and Redlich–Peterson (R–P) [100]. The best adsorption isotherm can be judged by correlation coefficients and R^2 values [99].

Langmuir and Freundlich adsorption isotherm models are often used to characterize the connection between the quantity adsorbed per unit weight of adsorbent and the amount of solute non-adsorbed at equilibrium. Both have been used several times for heavy metal adsorption using various adsorbents and showed favorable results. At constant temperature and equilibrium solute concentration, adsorption isotherm models explain the interaction behavior of the adsorbent and heavy metal. These adsorption isotherm models help the researchers investigate the adsorption mechanism and optimize the use of the adsorbent by determining the amount of adsorbent required to uptake a desired concentration of heavy metals from the aqueous solution.

2.1. Langmuir adsorption isotherm

The Langmuir adsorption isotherm model is based on the chemical and physical interactions between the solute and the vacant sites on the surface of the adsorbent [101]. It reflects monolayer adsorption and adsorption at only specific homogeneous sites within the adsorbent. All of the Langmuir adsorption isotherm sites are regarded as similar and energetically comparable; once the adsorbate molecule occupies a site, no additional adsorption may occur in that site [84,100]. It is used to find out the maximum adsorption capacity (q_m) of the adsorbent, Langmuir isotherm constant (K_L), separation factor (R_L), and correlation coefficients (R^2) [98, 101–103]. It can be used to predict the shape of the isotherm by the R_L value. If $R_L > 1$ (adsorption is unfavorable), $R_L = 1$ (adsorption
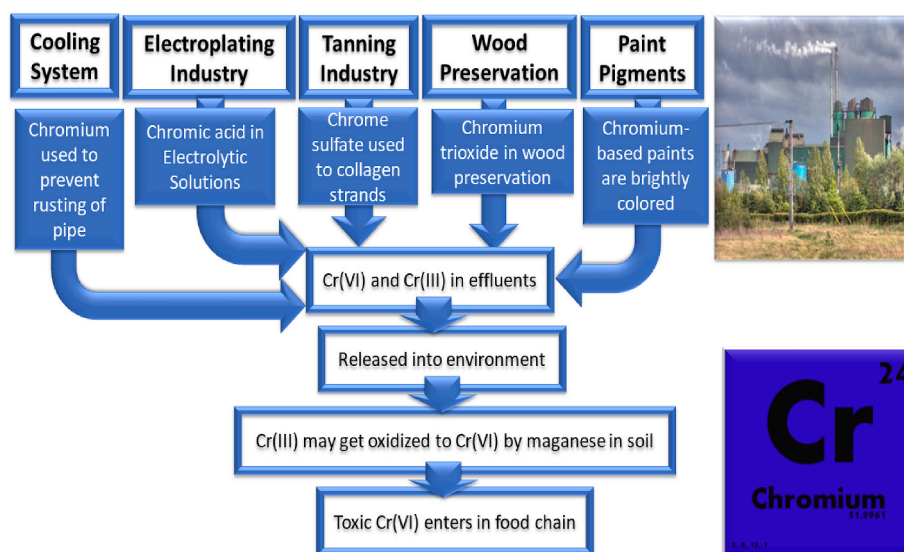

Fig. 2. Sources of Chromium industrial effluents.

Table 1
Conventional remediation methods of Cr(VI).

S#	Process	Process Type	Comments	Ref.
1	Liquid-liquid extraction	Physical	●Amine-based extractants (hard bases), preferably long-chain quaternary ammonium or tertiary amine-based compounds.	[62–67]
2	Chemical precipitation	Chemical	Advantages include: ●Simple ●Inexpensive ●It can be applied to a variety of metals Disadvantages include: ●Larger sludge formation ●Sludge disposal	[68–70]
3	Chemical coagulation	Chemical	Advantages include: ●Settling of sludge ●Dewatering Disadvantages include: ●Expensive ●Higher chemicals consumption	[68–70]
4	Ion-exchange	Chemical	Advantages include: ●Higher materials regeneration ●Metal selective ●Fast kinetics Disadvantages include: ●Expensive ●Lesser removal of metal ions ●Membrane fouling ●pH sensitivity ●Non-selectivity of the membrane	[68–71]
5	Electrochemical method	Chemical	Advantages include: ●Metal selective ●No chemicals consumption ●Attainment of pure metals Disadvantages include: ●Membrane Fouling ●Higher capital costs ●Higher running costs ●Higher energy consumption	[68–70]
6	Adsorption	Physical	Advantages include: ●Commonly used method for heavy metal removal ●The commonly used adsorbents include peroxide-modified titanium dioxide, zeolite, and chitosan and some inorganic cationic adsorbents, such as nitrogen-enriched activated carbons, zeolites modified with quaternary ammonium surfactants, and magnetic lignin composite adsorbent Disadvantages include: ●Performance efficiency depends on the type of adsorbent used.	[68–70, 72–77]
7	Membrane process and ultrafiltration	Physical	Advantages include: ●Lesser production of the solid waste ●Lesser chemical consumption ●Higher efficiency (even >95%) ●Require less space ●Require low pressure Disadvantages include: ●Higher initial cost ●Higher running cost ●Lower flow rates ●Heavy metal % removal declines in the presence of other metals ●Process complexity	[68–70]

Table 2

Langmuir and Freundlich adsorption isotherm constants obtained for Cr(VI) heavy metal adsorption by biosorbents.

Adsorbent type	Adsorbent	Source of Cr(VI)	Initial Cr(VI) Conc. (mg/l)	T/K	pH	Cont. t (min)	Dose (g/L)	Exp. q_m (mg/g)	Langmuir q_m (mg/g)	K_L (L/mg)	R^2	R_L	Freundlich K_F	n	R^2	Isotherm model	Ref
Fruit Waste	Pomegranate peel-Ppy	Cr(VI) aqueous solution of $K_2Cr_2O_7$	50	298	5.5	30	1	–	20.79002	0.11385	0.8053	–	2.154	1.37	0.92	F	[117]
	Grape waste	Cr(VI) aqueous solution of $K_2Cr_2O_7$	20-120	293	2	240	0.5	–	108.12	0.0380	0.9847	–	23.23	2.70	0.9743	L	[118]
	Olive waste		20-120	293	2	240	0.5	–	100.47	0.0816	0.9676	–	43.033	4.95	0.9386	L	[118]
	Mango kernel bio-composite	Cr(VI) aqueous solution of $K_2Cr_2O_7$	200	306	3	30	0.5	320.07	322.58	–	0.99	–	134.4	6.17	0.453	L	[112]
Fungus	Cladosporium cladosporioides	Cr(VI) aqueous solution of $K_2Cr_2O_7$	100-400	298	1	10080	3	–	222.22	5	0.8825	–	311.3756	1.582	0.9817	F	[106]
	Rhizopus sp.	Cr(VI) aqueous solution of $K_2Cr_2O_7$	12.5–300	283	2	240	5	–	9.9507	0.1557	0.9364	0.0316–0.304	1.9281	2.0796	0.8243	L	[119]
			12.5–300	298	2	240	5	–	8.0589	0.7730	0.8410	0.0064–0.1169	1.3518	1.9598	0.7888	L	[119]
			12.5–300	318	2	240	5	–	9.3811	1.2303	0.8930	0.0041–0.0819	0.9489	3.0158	0.8018	L	[119]
	Artist's Bracket	Cr(VI) aqueous solution of $K_2Cr_2O_7$	25, 50, 100, 200 and 300	298	2	180	5	–	200	0.002	0.9998	0.015	0.54	1.71	0.9992	L	[120]
	Aspergillus fumigatus	Mine drainage water	50	308	5.5	–	–	48.2	45.5	0.098	0.99	–	17.7	1.45	0.99	F	[113]
	Arthrinium malaysianum	Cr(VI) aqueous solution of $K_2Cr_2O_7$	50-1200	303	3	480	8	–	100.69	0.00138	0.9828	–	0.4837	1.412	0.9636	R–P	[121]
Leaf	Melaleuca diosmifolia leaf	Cr(VI) aqueous solution of $K_2Cr_2O_7$	100-500	297	7	120	5	–	62.50	0.13	0.98	0.07–0.01	–	–	–	L	[122]
	Magnolia leaf	Cr(VI) aqueous solution	40	313	2	45	0.5*	–	12.3	0.008	0.999	0.755	10.2	1.96	0.992	L	[123]

Table 2 (*continued*)

Adsorbent type	Adsorbent	Source of Cr(VI)	Initial Cr(VI) Conc. (mg/l)	T/K	pH	Cont. t (min)	Dose (g/L)	Exp. q_m (mg/g)	Langmuir				Freundlich			Isotherm model	Ref
									q_m (mg/g)	K_L (L/mg)	R^2	R_L	K_F	n	R^2		
		of K$_2$Cr$_2$O$_7$															
	Gliricidia sepiumLeaf (GSL) Powder	Cr(VI) aqueous solution of K$_2$Cr$_2$O$_7$	50	313	2	120	0.3*	35.71	33.57 ± 4.177	0.570 ± 0.366	0.846	0.33	16.046 ± 1.204	4.905 ± 0.600	0.974	F	[114]
	Mangrove leaf powder	Cr(VI) aqueous solution	400	283	2	30	4	–	54.3478	0.0141	0.9824	0.1505	2.1552	1.8807	0.9552	L	[124]
			400	298	2	30	4	–	60.2409	0.0243	0.9827	0.0932	3.6544	2.1767	0.9942	F	[124]
			400	313	2	30	4	–	52.6315	0.0221	0.9913	0.1015	3.1006	2.1477	0.9397	L	[124]
	Azadirachta Indica (Neem) Leaf Powder	Cr(VI) aqueous solution of K$_2$Cr$_2$O$_7$	7.1–24.8	300	5.5	180	1.6	–	14.38	0.407	0.95	0.122	0.876	0.58	0.99	F	[115]
			7.1–24.8	300	5.5	180	2	–	19.49	0.283	0.99	0.166	0.733	0.57	0.99	F	[115]
			7.1–24.8	300	5.5	180	6	–	38.00	0.078	0.98	0.419	0.162	0.41	0.97	L	[115]
			7.1–24.8	300	5.5	180	10	–	83.62	0.046	0.98	0.554	0.128	0.42	0.99	F	[115]
			7.1–24.8	300	5.5	180	14	–	145.77	0.032	0.97	0.637	0.101	0.40	0.99	F	[115]
Biochar	NCBC	Cr(VI) aqueous solution of K$_2$Cr$_2$O$_7$	25	298	1.5	720	2	–	3.53	0.5486	0.99	–	1.43	3.542	0.97	L	[125]
	NZCBC		25	298	1.5	720	2	–	3.97	0.3237	0.95	–	1.59	4.476	0.81	L	[125]
	ACBC		25	298	1.5	720	2	–	6.08	0.4067	0.97	–	1.96	2.799	0.98	L	[125]
	Oak wood char	Cr(VI) aqueous solution of K$_2$Cr$_2$O$_7$	1-100	298	2	2880	10	–	3.031	0.051	0.6460	–	0.436	2.475	0.6591	S	[116]
	Oak wood char		1-100	308	2	2880	10	–	4.076	0.082	0.5767	–	1.095	3.597	0.5854	S	[116]
	Oak wood char		1-100	318	2	2880	10	–	4.930	0.068	0.6658	–	1.038	3.012	0.6766	S	[116]
	Oak bark char		1-100	298	2	2880	10	–	4.619	0.073	0.9672	–	0.523	2.016	0.9149	S	[116]
	Oak bark char		1-100	308	2	2880	10	–	7.433	0.010	0.8183	–	0.942	1.957	0.7809	S	[116]
	Oak bark char		1-100	318	2	2880	10	–	7.515	0.149	0.7475		1.332	2.315	0.6534	S	[116]

NCBC=Natural biochar derived from oily seeds of P. terebinthus L; NZCBC = Zeolite based biochar derived from oily seeds of P. terebinthus L; ACBC = Alumina based biochar derived from oily seeds of P. terebinthus L; L = Langmuir adsorption isotherm; F=Freundlich adsorption isotherm; R–P=Redlich-Peterson adsorption isotherm; S=Sips adsorption isotherm.

is linear), $0 < R_L < 1$ (adsorption is favorable), $R_L = 0$ (adsorption is reversible) [101].

2.1.1. Linearized Langmuir adsorption isotherm equation

The linearized Langmuir adsorption isotherm equation (1) is represented below:

$$\frac{C_e}{q_e} = \frac{C_e}{q_m} + \frac{1}{q_m K_L} \tag{1}$$

where q_m represents the maximum monolayer adsorption capacity of the adsorbent (mg g^{-1}), and K_L represents the Langmuir adsorption constant (L mg^{-1}) [101–103].

2.1.2. Non-linear Langmuir isotherm equation

The non-linearized Langmuir adsorption isotherm equation (2) is represented below:

$$q_e = q_m K_L \frac{C_e}{1 + K_L C_e} \tag{2}$$

Separation Factor (R_L): The Langmuir isotherm can estimate the separation factor, i.e., the affinity between the adsorbate and adsorbent. It can be calculated by using equation (3):

$$R_L = \frac{1}{1 + K_L C_o} \tag{3}$$

C_o represents the highest initial adsorbate concentration in the solution (mg L^{-1}). The value of R_L shows whether the isotherm's shape is either unfavorable ($R_L > 1$), linear ($R_L = 1$), favorable ($0 < R_L < 1$), or reversible ($R_L = 0$) [101].

2.2. Freundlich adsorption isotherm

The Freundlich isotherm model only applies to adsorption processes on heterogeneous surfaces and reflects multilayer adsorption [104]. This model implies that (i) numerous layers of adsorbate can be linked to the adsorbent and that adsorbate will constantly bind to the adsorbent, and (ii) the energy required for adsorption is not constant but fluctuates and is exponentially distributed [98,105]. It is used to find out the capacity of the adsorbent (K_F) in mg g^{-1} and the adsorption constant for Freundlich (n) in L mg^{-1}, and correlation coefficients (R^2) [98]. If the 1/n number is less than one, the adsorption process is chemical; if the value is more than one, the adsorption process is favorable [100]. Freundlich adsorption isotherm can be represented by the linear (equation (4)) and non-linear (equation (5)) forms as:

2.2.1. Linearized Freundlich adsorption isotherm equation

$$\ln q_e = \ln K_F + \frac{1}{n} \ln C_e \tag{4}$$

2.2.2. Non-linear Freundlich adsorption isotherm equation

$$q_e = K_F C_e^{1/n} \tag{5}$$

where q_e is the adsorption capacity at equilibrium (mg g^{-1}), C_e is the Cr(VI) concentration at equilibrium (mg $^{-1}$), K_F is the Freundlich constant (l mg^{-1}) which indicates the adsorption capacity on heterogenous sites of an adsorbent, and n is the intensity of adsorbent. Adsorption is favorable when the value of 1/n lies between 0.1 and 1 [106]. In addition, the n values determine the degree of
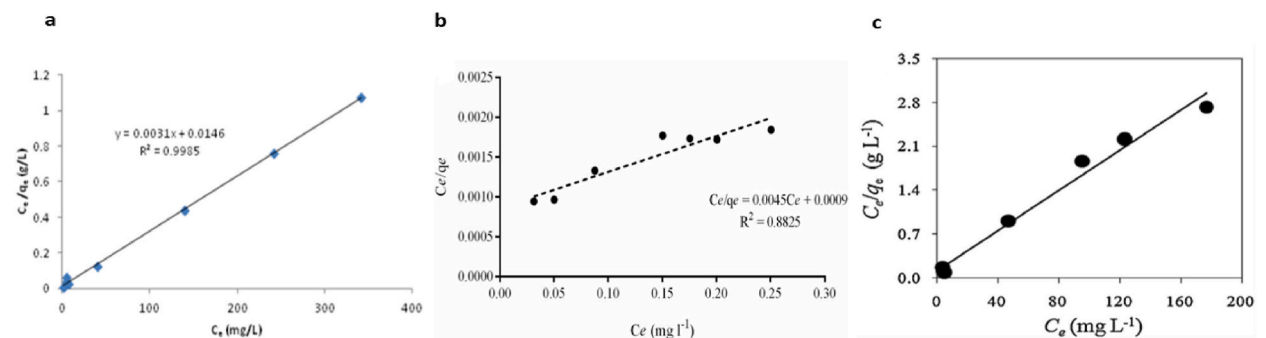
Fig. 3. Langmuir Isotherm of biosorbents for Cr(VI) adsorption **(a)** Mango kernel bio-composite [112],**(b)** Cladosporium cladosporioides [106], and **(c)** Melaleuca diosmifolia leaf [122].

nonlinearity between solution concentration and adsorption in the following manner: if n = 1, then adsorption is linear; if n > 1, then adsorption is a chemical process; and if n < 1, adsorption is considered as a physical process [107].

3. Adsorption & adsorption kinetics

The adsorption kinetic is important in determining the best conditions for a full-scale batch process. The adsorption kinetics of an adsorption system is influenced by several steps, such as the transfer of solute to the surface of the sorbent particle, transfer from the sorbent surface to the intra-particle active sites, and retention on these active sites via sorption, complexation, or intra-particle precipitation phenomena [108]. Experimental data is often analyzed using two different kinetics models, namely pseudo-first-order and pseudo-second-order. These models are used to make predictions about the mechanisms involved in the sorption and identify potential rate controlling, such as chemical reaction processes. In recent years, these models have been widely used to describe the adsorption of heavy metals from wastewater [109].

3.1. Pseudo-first order kinetic model

The pseudo-first-order kinetic model is one of the most widely used rate equations to describe the adsorption of adsorbate from a given liquid phase in non-linear (equation (6)) and linear (equation (7)) forms as:

$$\frac{dq}{dt} = k_1 (q_e - q_t) \tag{6}$$

$$\log(q_e - q_t) = \log q_e - \frac{k_1 t}{2.303} \tag{7}$$

3.2. Pseudo-first order kinetic model

The pseudo-second-order kinetic model assumes the adsorption process is chemisorption [110]. The mechanism may involve sharing valence forces or exchanging electrons between adsorbents and adsorbates [111]. The pseudo-second-order adsorption kinetic model can be expressed in non-linear (equation (8)) and linear (equation (9)) forms as shown below:

$$\frac{dq}{dt} = k_1 (q_e - q_t)^2 \tag{8}$$

$$\frac{t}{q_t} = \frac{1}{k_2 q_e^2} + \frac{t}{q_e} \tag{9}$$

where, k_2 (g^{-1} min^{-1}) represents the pseudo-second-order rate constant. The second-order sorption rate constant and q_e can be determined from the slope and intercept of the plot between t/q_t and time. The best-fit model can be selected based on the regression coefficient (R^2).

4. Classification of the novel adsorbents

Adsorbents can be classified into biosorbents, biomass-derived activated carbons, nanocomposites, and PANI composites. These
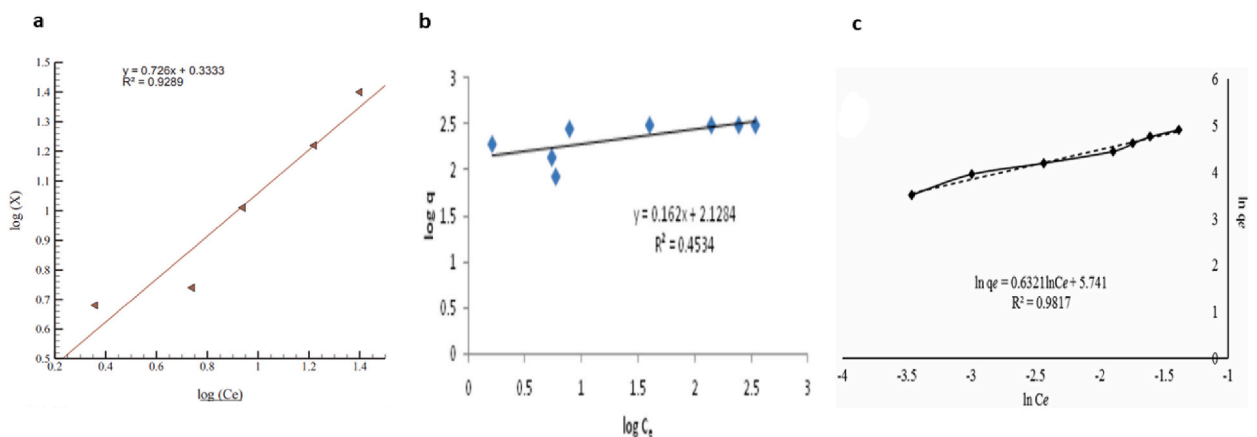

Fig. 4. Freundlich Isotherm of biosorbents for Cr(VI) adsorption **(a)** Pomegranate peel-Ppy [117], **(b)** Mango kernel bio-composite [112], and **(c)** Cladosporium cladosporioides [106].

Table 3
Pseudo-first-order and pseudo-second-order kinetic model constants obtained for Cr(VI) heavy metal adsorption by biosorbents.

Adsorbent type	Adsorbent	Initial Cr(VI) Conc. (mg/l)	T/K	pH	Dose (g/L)	$q_{e,exp}$ (mg/g)	Pseudo-first order kinetic model			Pseudo-second order kinetic model			Kinetic model	Ref
							$q^{I}_{e,cal}$ (mg/g)	k_1 (1/min)	R^2	$q^{II}_{e,cal}$ (mg/g)	k_2 (g/mg. min)	R^2		
Fruit Waste	Pomegranate peel-Ppy	50	298	5.5	1	–	–	–	–	–	–	–	–	[117]
	Grape waste	20	293	2	0.5	15.9	15.2	0.079	0.977	15.6	0.43	0.982	PSO	[118]
		40	293	2	0.5	29.9	29.1	0.052	0.989	27.7	0.37	0.963	PFO	
		60	293	2	0.5	66.5	61.5	0.031	0.951	62.9	0.24	0.976	PSO	
		80	293	2	0.5	83.6	76.7	0.027	0.892	81	0.19	0.971	PSO	
		100	293	2	0.5	98.3	98.1	0.024	0.993	98.2	0.12	0.999	PSO	
		120	293	2	0.5	104.3	103.3	0.022	0.977	104.5	0.11	0.997	PSO	
	Olive waste	20	293	2	0.5	14.7	14.5	0.075	0.968	14.6	0.44	0.983	PSO	[118]
		40	293	2	0.5	34.6	33.9	0.071	0.984	33.9	0.34	0.983	PFO	
		60	293	2	0.5	64.7	61.5	0.029	0.961	63.9	0.24	0.989	PSO	
		80	293	2	0.5	86.7	82.9	0.035	0.973	87.6	0.07	0.986	PSO	
		100	293	2	0.5	95.3	95.3	0.019	0.987	96.4	0.06	0.978	PFO	
		120	293	2	0.5	99.9	97.3	0.018	0.978	100.5	0.06	0.991	PSO	
	Mango kernel bio-composite	75	306	3	0.5	139.25	10.05	−0.027	0.483	141	0.0058	0.999	PSO	[112]
		100	306	3	0.5	196.78	12.74	−0.027	0.488	200	0.0045	0.999	PSO	
		150	306	3	0.5	284.55	12.02	−0.027	0.485	286	0.0051	0.999	PSO	
Fungus	Cladosporium cladosporioides	100	298	1	3	–	20.227	0.0279*	0.9985	28.902	0.0045**	0.9908	PFO	[106]
	Rhizopussp.	50	298	2	5	5.5080	1.7165	0.0056	0.8826	5.5679	0.0103	0.9975	PSO	[119]
	Rhizopussp.+NaCl	50	298	2	5	7.4580	2.7925	0.0080	0.8830	7.5852	0.0085	0.9982	PSO	[119]
	Artist's Bracket	50	298	2	3	15.63	1.61	0.044	0.932	16.13	0.074	0.999	PSO	[120]
	Aspergillus fumigatus	50	308	5.5	–	–	4.8	0.0316*	0.99	–	0.001**	0.93	PFO	[113]
	Arthrinium malaysianum	100	303	3	8	–	4.36	0.0499	0.983 7	5.45	0.0072	0.9907	PSO	[121]
Leaf	Melaleuca diosmifolia leaf	100-500	297	7	5	49.38	–	–	–	50	0.15	1	PSO	[122]
	Magnolia leaf	40	313	2	0.5[a]	3.97	3.59	0.235	0.885	4.01	0.798	0.987	PSO	[123]
	Gliricidia sepiumLeaf (GSL) Powder	50	313	2	0.3[a]	–	1.659	0.0023	0.795	9.259	0.0071	0.996	PSO	[114]
		100	313	2	0.3[a]		2.07	0.0046	0.924	18.86	0.0019	0.973	PSO	[114]
		150	313	2	0.3[a]		2.208	0.0046	0.771	27.03	0.0014	0.988	PSO	[114]
		200	313	2	0.3[a]		1.967	0.0046	0.731	33.33	0.0013	0.986	PSO	[114]
		250	313	2	0.3[a]		1.936	0.0046	0.723	40	0.0011	0.998	PSO	[114]
	Mangrove leaf powder	100	–	2	4	–	–	0.1119[b]	0.9600[b]	–	0.0299[b]	0.8308[b]	PFO	[124]
		100	–	2	4	–	–	0.0875[c]	0.9334[c]	–	0.0556[c]	0.9641[c]	PSO	[124]
		100	–	2	4	–	–	0.1545[d]	0.9017[d]	–	0.0623[d]	0.9499[d]	PSO	[124]
		100	–	2	4	–	–	0.1234[e]	0.9655[e]	–	0.0871[e]	0.9738[e]	PSO	[124]
		100	–	2	4	–	–	0.1372[f]	0.9321[f]	–	0.0691[f]	0.9471[f]	PSO	[124]
	Azadirachta Indica (Neem) Leaf Powder	14.1	300	5.5	1.6	0.1474	−1.733[g]	0.0141	0.89–0.99	0.1478	2.65–28.93	≈0.99	PSO	[115]
		14.1	300	5.5	2	0.1186	−1.774[g]	0.0141	0.89–0.99	0.1191	2.65–28.93	≈0.99	PSO	[115]
		14.1	300	5.5	6	0.0402	−2.097[g]	0.0141	0.89–0.99	0.0410	2.65–28.93	≈0.99	PSO	[115]
		14.1	300	5.5	10	0.0261	−1.969[g]	0.0141	0.89–0.99	0.0252	2.65–28.93	≈0.99	PSO	[115]
		14.1	300	5.5	14	0.0184	−2.535[g]	0.0141	0.89–0.99	0.0185	2.65–28.93	≈0.99	PSO	[115]

(*continued on next page*)

Table 3 (*continued*)

Adsorbent type	Adsorbent	Initial Cr(VI) Conc. (mg/l)	T/K	pH	Dose (g/L)	$q_{e,exp}$ (mg/g)	Pseudo-first order kinetic model			Pseudo-second order kinetic model			Kinetic model	Ref
							$q_{e,cal}^{I}$ (mg/g)	k_1 (1/min)	R^2	$q_{e,cal}^{II}$ (mg/g)	k_2 (g/mg. min)	R^2		
Biochar	NCBC	25	298	1.5	2	1.86	0.302	0.012	0.78	1.85	0.2141	0.99	PSO	[125]
	NZCBC	25	298	1.5	2	1.94	0.331	0.0129	0.58	1.93	0.2127	0.99	PSO	[125]
	ACBC	25	298	1.5	2	2.43	0.9	0.0131	0.78	2.43	0.059	0.99	PSO	[125]
	Oak wood char	40	298	2	10	1.97	1.77	1.77*	0.9029	2	2.00**	0.9151	PFO	[116]
		40	308	2	10	3.11	2.94	2.95*	0.8530	3.49	3.49**	0.8829	PSO	[116]
		40	318	2	10	3.54	3.21	3.21*	0.2930	3.49	3.49**	0.9125	PSO	[116]
	Oak bark char	40	298	2	10	1.93	1.49	1.49*	0.6072	1.63	1.63**	0.6542	PSO	[116]
		40	308	2	10	1.97	1.53	1.53*	0.6819	1.74	1.74**	0.8071	PSO	[116]
		40	318	2	10	2.34	2.08	2.08*	0.8048	2.26	2.26**	0.8986	PSO	[116]
	Oak wood char	20	298	2	10	1.82	1.71	1.71*	0.800	1.87	1.87**	0.8510	PSO	[116]
		40	298	2	10	2.6	2.62	2.64*	0.7481	2.91	2.91**	0.8111	PSO	[116]
		60	298	2	10	4.1	2.75	2.75*	0.6382	3	3.00**	0.7172	PSO	[116]
		80	298	2	10	5.5	4.73	4.73*	0.6663	6.12	6.12**	0.6808	PSO	[116]
	Oak bark char	20	298	2	10	1.8	2	2.00*	0.9520	2.34	2.34**	0.9505	PFO	[116]
		40	298	2	10	2.58	2.17	2.18*	0.7931	2.39	2.39**	0.8241	PSO	[116]
		60	298	2	10	3.4	3.18	3.18*	0.5030	3.37	3.37**	0.5934	PSO	[116]
		80	298	2	10	4.09	3.65	3.65*	0.6960	3.92	3.92**	0.7615	PSO	[116]

NCBC=Natural biochar derived from oily seeds of P. terebinthus L; NZCBC = Zeolite based biochar derived from oily seeds of P. terebinthus L; ACBC = Alumina based biochar derived from oily seeds of P. terebinthus L; a = adsorbent dosage in g; * = k_1 in h^{-1}; **k_2 in $g.mg^{-1}.h^{-1}$, b = at particle size 1.4 mm; c = at particle size 1.0 mm; d = at particle size 0.6 mm; e = at particle size 0.5 mm; f = at particle size 0.25 mm; g = log($q_{e,calc}$); PFO= Pseudo-first-order kinetic model; PSO= Pseudo-second-order kinetic model.
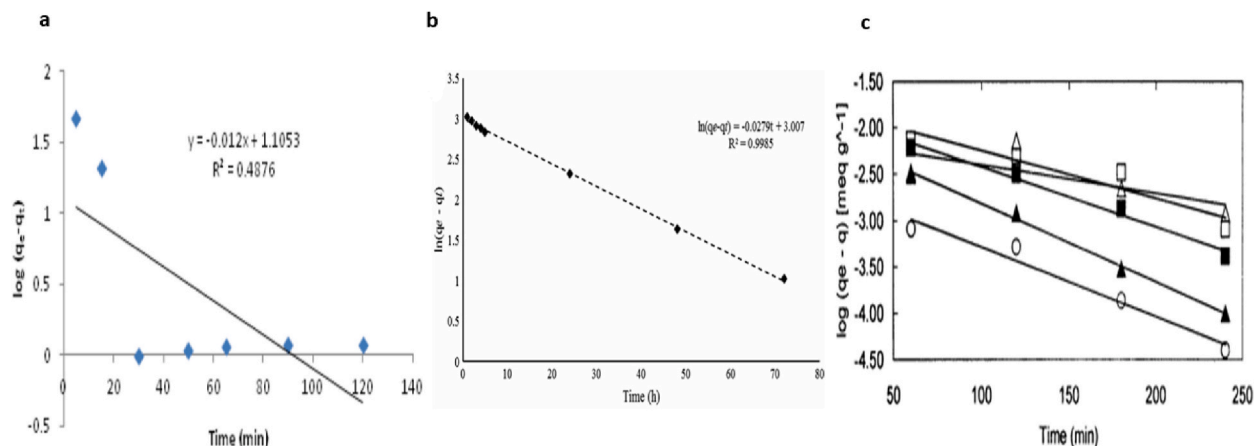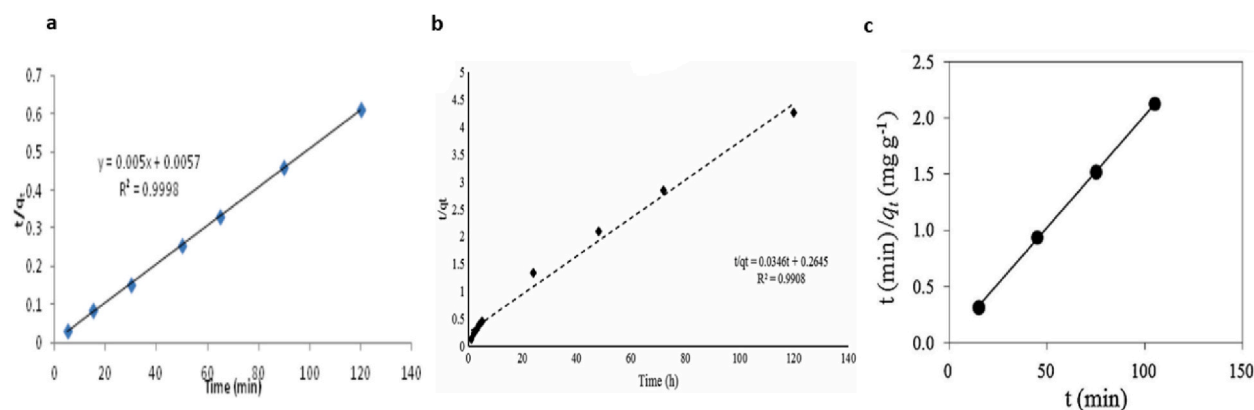
Fig. 5. Pseudo-first-order kinetic model of biosorbents for Cr(VI) adsorption **(a)** Mango kernel bio-composite [112], **(b)** Cladosporium clado-sporioides [106], and **(c)** Azadirachta Indica (Neem) Leaf Powder [115].

Fig. 6. Pseudo-second-order kinetic model of biosorbents for Cr(VI) adsorption **(a)** Mango kernel bio-composite [112], **(b)** Cladosporium clado-sporioides [106], and **(c)** Melaleuca diosmifolia leaf [122].

adsorbents are used for efficient heavy metal (Cr(VI)) removal from wastewater using Langmuir and Freundlich adsorption isotherms and Pseudo-first-order and Pseudo-second-order kinetic models, which are discussed in detail below:

4.1. Biosorbents

Biomass-based adsorbents, commonly known as biosorbents, are extensively used to remove heavy metals. Biosorbents from low-cost agricultural waste can remove and recover heavy metal contaminants such as chromium ions from wastewater streams [37–44]. Examples of biosorbents used for the removal of Cr(VI) from wastewater include Macadamia nutshells [45], pine cone biomass [46], Cannabinus kenaf [47], Masau stones [48], sawdust [49], almond green hull [50], grape peelings [51], lemon peel powder [52], coir pith [53] and fungal biomass [54]. Activated carbons are used extensively as adsorbent material for removing chromium due to their high surface area (500–$1500 \, m^2 \, g^{-1}$), well-developed microporous structure, and a wide spectrum of surface functional groups like the carboxylic group [55,81]. It is the most commonly used adsorbent for chromium adsorption [93]. It is used extensively for chromium adsorption during wastewater treatment [56,81,93].

4.1.1. Biosorbents and Langmuir adsorption isotherm

The maximum adsorption capacity is dependent on the type of biosorbent. Several biosorbents, such as fruit waste biosorbent, fungal biosorbent, leaf biosorbent, and biochar biosorbent for Cr(VI) adsorption, have been used. The Langmuir adsorption isotherms of the biosorbents are evaluated based on the maximum adsorption capacity, Langmuir constant (K_L), and R^2 value. The best maximum adsorption capacity of biosorbent is exhibited by the mango kernel bio-composite (fruit waste biosorbent) while representing the

Table 4
Langmuir and Freundlich adsorption isotherm constants obtained for Cr(VI) heavy metal adsorption using biomass-derived activated carbon.

Adsorbent type	Adsorbent	Source of Cr (VI)	Initial Cr (VI) Conc. (mg/l)	T/ K	pH	Cont. t (min)	Dose (g/L)	Exp. q_m (mg/g)	Langmuir				Freundlich			Isotherm model	Ref
									q_m (mg/g)	K_L (L/mg)	R^2	R_L	K_F	n	R^2		
Acid-treated activated carbon	Juniperus procera Leaves-H$_2$SO$_4$ acid AC	Cr(VI) aqueous solution of K$_2$Cr$_2$O$_7$	50-300	298	4	120	10	–	23	0.01	0.991	–	24.45	0.20	0.920	L	[107]
	Phosphoric acid-activated Leucaena leucocephala waste sawdust-based activated carbon	Cr(VI) aqueous solution of K$_2$Cr$_2$O$_7$	100	283	4	60	6	–	111	0.010	0.994	–	1.95	1.45	0.984	L	[132]
			100	293	4	60	6	–	125	0.009	0.997	–	1.89	1.40	0.989	L	[132]
			100	303	4	60	6	–	125	0.008	0.989	–	2.05	1.39	0.996	F	[132]
			100	313	4	60	6	–	143	0.007	0.979	–	2.02	1.39	0.997	F	[132]
			100	323	4	60	6	–	143	0.006	0.956	–	2.21	1.4	0.997	F	[132]
	H$_2$SO$_4$-activated F. nitida leaves derived activated carbon	Cr(VI) aqueous solution of K$_2$Cr$_2$O$_7$	50	298	1.5–4	25	8	–	21.0	0.185	0.9995	–	4.79	2.85	0.9343	L	[133]
	PEI-HNO$_3$ acid-rice husk derived biochar based activated carbon	Cr(VI) aqueous solution of K$_2$Cr$_2$O$_7$	10-1000	303	6.8 ± 0.1	1440	1	–	60.78	0.023	0.855	–	8.78	3.27	0.968	L	[130]
	HCl modified Cashew husk based tannery residual biomass-derived activated carbon	Cr(VI) aqueous solution of K$_2$Cr$_2$O$_7$	100-350	303	2	1440	1	–	177.31	0.0698	0.9918	–	66.8452	5.534	0.9881	L	[134]
			100-350	313	2	1440	1	–	200.40	0.1090	0.9994	–	65.5994	4.395	0.9935	L	[134]
			100-350	323	2	1440	1	–	217.39	0.1126	0.9977	–	74.2489	4.67	0.9907	L	[134]
	Sulphuric acid-treated sunflower head activated carbon	Cr(VI) aqueous solution of K$_2$Cr$_2$O$_7$	250	298	2	120	4	–	53.8	0.12	0.9989	–	14.5	3.3	0.9663	L	[135]
	Sulphuric acid-treated sunflower stem-activated carbon		250	298	2	120	4	–	56.5	0.21	0.9371	–	24.4	5.3	0.8813	L	[135]
	Phosphoric acid-treated bael fruit shell-activated carbon	Cr(VI) aqueous solution of K$_2$Cr$_2$O$_7$	50-125	RT	2	240	10	–	17.27	0.0848	0.9865	0.1908–0.0862	2.110	1.79	0.9996	F	[136]
	H$_2$SO$_4$ treated Tamarind seeds activated carbon	Cr(VI) aqueous solution of K$_2$Cr$_2$O$_7$	20-200	303	7	600	10	–	11.08	0.049	0.93	–	1.051	2.06	0.99	F	[137]
	Phosphoric acid-treated tamarind hull-activated carbon	Cr(VI) aqueous solution of K$_2$Cr$_2$O$_7$	50	303	2	1200	1	–	85.91	2.35	0.8927	–	53.47	6.71	0.9909	F	[131]
Base-treated activated carbon	KOH activated Chickpea-husk-derived activated carbon	Cr(VI) aqueous solution of K$_2$Cr$_2$O$_7$	100-400	293	8	360	3	–	126.5823	0.0265	0.9575	–	0.7781	1.3586	0.9837	F	[138]
	PEI-KOH alkali-rice husk derived biochar based activated carbon	Cr(VI) aqueous solution of K$_2$Cr$_2$O$_7$	10-1000	303	6.8 ± 0.1	1440	1	–	435.7	0.0046	0.972	–	14.04	2.06	0.939	L	[130]
Acid/base-treated activated carbon	NaOH/HCl activated P. terebinthus L oily seeds-based activated carbon	Cr(VI) aqueous solution of K$_2$Cr$_2$O$_7$	25	298	1.5	720	2	–	9.97	0.4283	0.87	–	3.23	2.835	0.96	F	[125]
	KOH/HCl activated CCAC	Cr(VI) aqueous solution of K$_2$Cr$_2$O$_7$	10-100	294	1.5	150	8	–	38.5	0.14	0.986	–	5.1	1.515	0.973	L	[139]

CCAC=Coconut coir activated carbon; RT = Room Temperature; L = Langmuir adsorption isotherm; F=Freundlich adsorption isotherm.

mono-layer adsorption as shown by the R^2 value approaching unity [112]. It is evident from the literature cited in Table 2 that most of the biosorbents followed the mono-layer adsorption except the Cladosporium cladosporioides (fungal biosorbent) [106], Aspergillus fumigatus (fungal biosorbent) [113], Gliricidia sepium leaf (GSL) powder (leaf biosorbent) [114], and Azadirachta Indica (Neem) leaf powder (leaf biosorbent) [115]. However, the oak wood biochar (biochar biosorbent) and oak bark char (biochar biosorbent) follow Sips isotherm, which indicates that these biochar biosorbents followed both mono-layer and multi-layer adsorption [116].

Hence, the biochar biosorbents track the mono-layer and multi-layer adsorption mechanisms [116]. Hence, it can be stated that the type of adsorption mechanism depends on the source of the biochar biosorbent. In addition, Cladosporium cladosporioides (fungal biosorbent) resulted in the highest Langmuir constant (K_L) value indicating a stronger interaction between Cr(VI) and Cladosporium cladosporioides (fungal biosorbent) [106] among other types of biosorbents. Various biosorbents were used to absorb Cr(VI). The Langmuir adsorption isotherms for Cr(VI) adsorption using biosorbents are presented in Fig. 3. The Langmuir adsorption isotherm constants obtained for Cr(VI) heavy metal adsorption by using biosorbents as adsorbents are listed in Table 2.

The maximum adsorption capacity, Langmuir constant (K_L) and R^2 depend on the type of biosorbents used. The mango kernel bio-composite (fruit waste biosorbent) resulted in the best Langmuir adsorption isotherms for Cr(VI) adsorption as represented by its highest maximum adsorption capacity and R^2 value approaching unity indicating the well-fitting of the Langmuir isotherm with the experimental adsorption capacity as shown in Fig. 3 (a) [112] among other fruit waste biosorbents cited in Table 2 such as pomegranate peel [117], grape waste [118], and olive waste [118]. Furthermore, it can be interpreted from the R^2 value approaching unity that the mango kernel bio-composite (fruit waste biosorbent) follows a mono-layer adsorption mechanism.

However, the Cladosporium cladosporioides (fungal biosorbent) resulted in good Langmuir maximum adsorption capacity. However, it does not exactly follow Langmuir adsorption isotherms for Cr(VI) adsorption as represented by its R^2 value is less than 0.9, indicating that the Langmuir isotherm fairly fits with the experimental adsorption capacity as shown in Fig. 3 (b). The K_L greater than unity indicates a stronger interaction between Cr(VI) and Cladosporium cladosporioides (fungal biosorbent) [106].

Moreover, the Azadirachta Indica (Neem) leaf powder (leaf biosorbent) resulted in the highest Langmuir adsorption capacity among other leaf biosorbents while showing weaker interactions between Cr(VI) and Azadirachta Indica (Neem) leaf powder (leaf biosorbent) [115]. The Melaleuca diosmifolia leaf (leaf biosorbent) resulted in good Langmuir adsorption isotherms for Cr(VI) adsorption as represented by its maximum adsorption capacity and R^2 value approaching unity, indicating that the Langmuir isotherm fits well with the experimental adsorption capacity value as shown in Fig. 3 (c). Furthermore, it can be interpreted from the R^2 value approaching unity that the Melaleuca diosmifolia leaf (leaf biosorbent) follows a mono-layer adsorption mechanism. The K_L, less than unity, indicates a weaker interaction between Cr(VI) and Melaleuca diosmifolia leaf (leaf biosorbent) [122].

The biochar biosorbents generally resulted in poor Langmuir adsorption isotherms for Cr(VI) adsorption as represented by its lowest maximum adsorption capacity and R^2 value ranging between 0.99 and 0.5767, indicating that the biochar biosorbents follow monolayer and multilayer adsorption [116,125]. The oak bark char (biochar biosorbent) resulted in better Langmuir adsorption isotherms for Cr(VI) adsorption as represented by its maximum adsorption capacity and R^2 value approaching unity [116], among other biochar biosorbents cited in Table 2, such as NCBC [125], NZCBC [125], ACBC [125], and oak wood char [116]. The oak bark char (biochar biosorbent) follows monolayer adsorption as the R^2 value approaches unity [116]. Hence, it can be stated that the type of adsorption mechanism depends on the source of the biochar biosorbent. Furthermore, all biochar biosorbents cited in Table 2 showed a Langmuir constant (K_L) value lesser than unity indicating weaker interaction between Cr(VI) and biochar biosorbents.

It can be concluded that the best Langmuir adsorption isotherm results for Cr(VI) adsorption are shown by mango kernel bio-composite (fruit waste biosorbent) as indicated by its highest maximum adsorption capacity and R^2 value (provided that the K_L value was missing in the literature) However, the best interaction between Cr(VI) and biosorbent is shown by Cladosporium cladosporioides (fungal biosorbent) as demonstrated by the highest Langmuir constant (K_L) value.
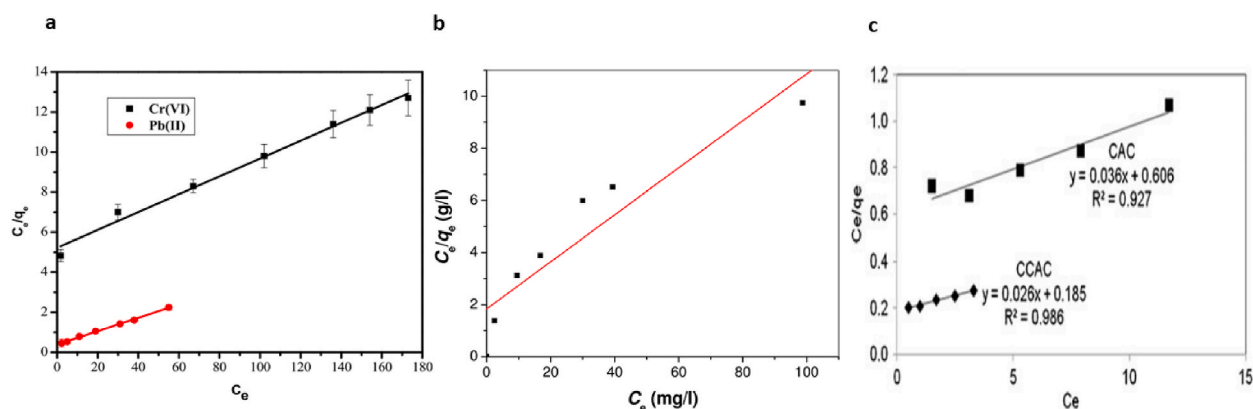

Fig. 7. Langmuir Isotherm of biomass-derived activated carbons adsorbents for Cr(VI) adsorption **(a)** Juniperus procera Leaves-H$_2$SO$_4$ acid activated carbon [107], **(b)** H$_2$SO$_4$ treated Tamarind seeds activated carbon [137], and **(c)** Coconut Coir Activated Carbon (CCAC) and Commercial Activated Carbon (CAC) [139].

4.1.2. Biosorbents and Freundlich adsorption isotherm

The adsorption capacity of an adsorbent on heterogeneous sites (K_F) depends on the type of biosorbent used. Freundlich adsorption isotherm of various biosorbents, such as fruit waste biosorbent, fungal biosorbent, leaf biosorbent, and biochar biosorbent, have been used for Cr(VI) adsorption. The Freundlich adsorption isotherms of the biosorbents were evaluated based on the Freundlich constant (K_F), the intensity of the adsorbent (n), and the R^2 value. Table 2 presents the Freundlich adsorption isotherm constants obtained for Cr (VI) heavy metal adsorption by using biosorbents as adsorbents. However, Fig. 4 presents the Freundlich adsorption isotherms for Cr (VI) adsorption using biosorbents as adsorbents.

The highest adsorption capacity of biosorbent was exhibited by the mango kernel bio-composite (fruit waste biosorbent) with the highest value of K_F and the highest intensity (n) of the Freundlich adsorption isotherm. However, it followed the mono-layer adsorption as shown by its lower R^2 value compared to Langmuir adsorption isotherm (Fig. 4 (a)) [112]. In contrast, the oak wood char (biochar) achieved the lowest Freundlich constant (K_F) while observing the Sips isotherm model, which is a combination of Langmuir and Freundlich isotherm models as R^2 values of Langmuir and Freundlich adsorption isotherms of oak wood char (biochar) are less than 0.9 indicating the Cr(VI) adsorption on the heterogenous surface of the oak wood char (biochar) following Freundlich adsorption isotherm at low initial Cr(VI) concentration and Langmuir adsorption isotherm at high initial Cr(VI) concentration [116].

All the biosorbents, including pomegranate peel-Ppy (fruit waste biosorbent) [117], grape waste (fruit waste biosorbent) [118], olive waste (fruit waste biosorbent) [118], mango kernel bio-composite (fruit waste biosorbent) [112], Cladosporium cladosporioides (fungus) [106], Melaleuca diosmifolia leaf (leaf) [122], NCBC (biochar) [125], NZCBC (biochar) [125], ACBC (biochar) [125], Oak wood char [116], and Oak bark char [116] showed the adsorption as a chemical process as indicated by adsorption intensity values of these biosorbents were greater than 1.

Moreover, only a few biosorbents followed the multi-layer adsorption, including Pomegranate peel-Ppy (Fig. 4 (b)) [117] and Cladosporium cladosporioides (Fig. 4 (c)) [106], indicating the heterogeneous surfaces of these biosorbents. The oak wood (biochar) showed the lowest Freundlich constant (K_F) [116], and Pomegranate peel-Ppy (fruit waste biosorbent) showed the lowest adsorption intensity (n) [117].

4.1.3. Biosorbents and pseudo-first order and pseudo-second order kinetic models

The experimental amount of adsorbate adsorbed at equilibrium ($q_{e,exp}$) depends on the type of biosorbent used, such as fruit waste biosorbent, fungal biosorbent, leaf biosorbent, and biochar biosorbent for Cr(VI) adsorption. The pseudo-first-order (PFO) and pseudo-second-order (PSO) kinetic models of biosorbents for Cr(VI) adsorption were evaluated using the experimental and calculated amounts of Cr(VI) adsorbed at equilibrium ($q_{e,exp}$, $q_{e,cal}^{I}$, $q_{e,cal}^{II}$ and $q_{e,cal}$), as well as the pseudo-first-order rate constant (k_1), pseudo-second-order rate constant (k_2) and R^2 value. Table 3 lists the experimental and calculated amounts of Cr(VI) adsorbed at equilibrium, pseudo-first-order and pseudo-second-order rate constants, and R^2 values obtained for various biosorbents for Cr(VI) adsorption.

The linear pseudo-first-order kinetic and pseudo-second-order kinetic models of biosorbents for Cr(VI) adsorption are shown in Figs. 5 and 6, respectively.

The mango kernel bio-composite (fruit waste biosorbent) exhibited the highest experimental and calculated amounts of Cr(VI) adsorbed at equilibrium ($q_{e,exp}$, and $q_{e,cal}^{II}$), with the highest R^2 value of the pseudo-second-order kinetic model as shown in Fig. 6 (a) indicating chemical sorption involving valence forces through sharing or exchange of electrons between the biosorbent and Cr(VI) as compared to pseudo-first-order kinetic model (Fig. 5 (a)) [112]. In contrast, the Azadirachta Indica (neem) leaf powder (leaf bio-sorbent) achieved the lowest experimental and calculated amounts of Cr(VI) adsorbed at equilibrium ($q_{e,exp}$, and $q_{e,cal}^{II}$), and while observing the pseudo-second-order kinetic model [115].
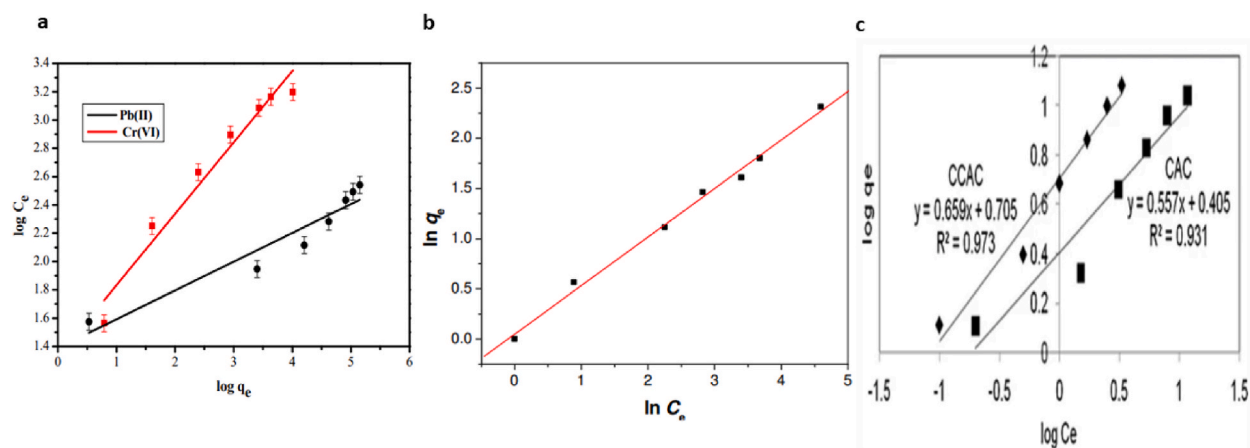

Fig. 8. Freundlich Isotherm of biomass-derived activated carbons adsorbents for Cr(VI) adsorption **(a)** Juniperus procera Leaves-H_2SO_4 acid activated carbon [107], **(b)** H_2SO_4 treated Tamarind seeds activated carbon [137], and **(c)** KOH/HCl activated Coconut Coir Activated Carbon (CCAC) and Commercial Activated Carbon (CAC) [139].

Table 5

Pseudo-first-order and pseudo-second-order kinetic model constants obtained for Cr(VI) heavy metal adsorption by biomass-derived activated carbon adsorbents.

Adsorbent type	Adsorbent	Initial Cr(VI) Conc. (mg/l)	T/ K	pH	Dose (g/L)	$q_{e,exp}$ (mg/g)	Pseudo-first order kinetic model			Pseudo-second order kinetic model			Kinetic model	Ref
							$q_{e,cal}^{I}$ (mg/g)	k_1 (1/ min)	R^2	$q_{e,cal}^{II}$ (mg/g)	k_2 (g/mg. min)	R^2		
Acid-treated activated carbon	Juniperus procera Leaves-H_2SO_4 acid AC	70	298	4	10	–	–	–	0.991	–	–	–	PFO	[107]
	Phosphoric acid-activated Leucaena leucocephala waste sawdust-based activated carbon	100	303	4	6	–	4.67	0.03	0.95	14.29	0.01	0.99	PSO	[132]
	HCl modified Cashew husk based tannery residual biomass-derived activated carbon	100	303	2	1	93.03	88.70	0.0193	0.9390	96.15	0.000516	0.9968	PSO	[134]
		150	303	2	1	119.89	94.93	0.0141	0.9552	126.58	0.000287	0.9981	PSO	[134]
		200	303	2	1	136.45	98.86	0.0136	0.9773	144.93	0.000253	0.9988	PSO	[134]
		250	303	2	1	145.40	80.91	0.0131	0.9846	151.52	0.00034	0.9995	PSO	[134]
		300	303	2	1	154.83	89.23	0.0145	0.9818	161.29	0.00038	0.9990	PSO	[134]
		350	303	2	1	174.25	122.80	0.0157	0.9577	185.19	0.00025	0.9993	PSO	[134]
	Sulphuric acid-treated sunflower head activated carbon	250	298	2	4	47.30	31.48	0.0267	0.9941	51.55	0.00127	0.9980	PSO	[135]
	Sulphuric acid-treated sunflower stem-activated carbon	250	298	2	4	53.56	49.14	0.0301	0.9764	59.52	0.00087	0.9958	PSO	[135]
	Phosphoric acid-treated bael fruit shell-activated carbon	50	RT	2	10	4.595	1.3187	0.0154	0.9410	4.661	0.0353	0.9999	PSO	[136]
		75	RT	2	10	6.719	2.2480	0.0154	0.9423	6.873	0.0183	0.9999	PSO	[136]
		100	RT	2	10	8.719	3.7282	0.0200	0.9457	9.009	0.0119	0.9999	PSO	[136]
		125	RT	2	10	10.682	4.3521	0.0154	0.9287	11.049	0.00082488	0.9997	PSO	[136]
	Phosphoric acid-treated tamarind hull-activated carbon	50	298	2	1	–	–	0.507*	–	–	–	–	PFO	[131]
		75	298	2	1	–	–	0.513*	–	–	–	–	PFO	[131]
		100	298	2	1	–	–	0.493*	–	–	–	–	PFO	[131]
Base-treated activated carbon	PEI-KOH alkali-rice husk derived biochar based activated carbon	100	303	6.8 ± 0.1	1	65.47	–	–	–	65.78	0.192**	0.999	PSO	[130]
		50	303	6.8 ± 0.1	1	36.05	–	–	–	36.63	0.160**	0.999	PSO	[130]
		100	303	6.8 ± 0.1	1	60.65	–	–	–	61.73	0.115**	0.999	PSO	[130]
		200	303	6.8 ± 0.1	1	114.05	–	–	–	116.28	0.040**	0.998	PSO	[130]
		500	303	6.8 ± 0.1	1	218.28	–	–	–	232.56	0.009**	0.995	PSO	[130]
	KOH activated Chickpea-husk-derived activated carbon	400	293	8	3	–	19.0633	0.0223	0.9431	46.5116	0.0040	0.9973	PSO	[138]
Acid/base-treated activated carbon	NaOH/HCl activated P. terebinthus L oily seeds-based activated carbon	25	298	1.5	2	2.52	1	0.009	0.96	2.48	0.0454	0.97	PSO	[125]
	KOH/HCl activated CCAC	20	294	1.5	8	–	–	3.567*	0.993	–	1.305**	0.999	PSO	[139]
		40	294	1.5	8	–	–	3.422*	0.982	–	0.251 **	0.998	PSO	[139]
		60	294	1.5	8	–	–	2.957*	0.961	–	0.185**	0.992	PSO	[139]

CCAC=Coconut coir activated carbon; RT = Room Temperature; **k_2 units in g/mg·h; PFO= Pseudo-first-order kinetic model; PSO= Pseudo-second-order kinetic model.
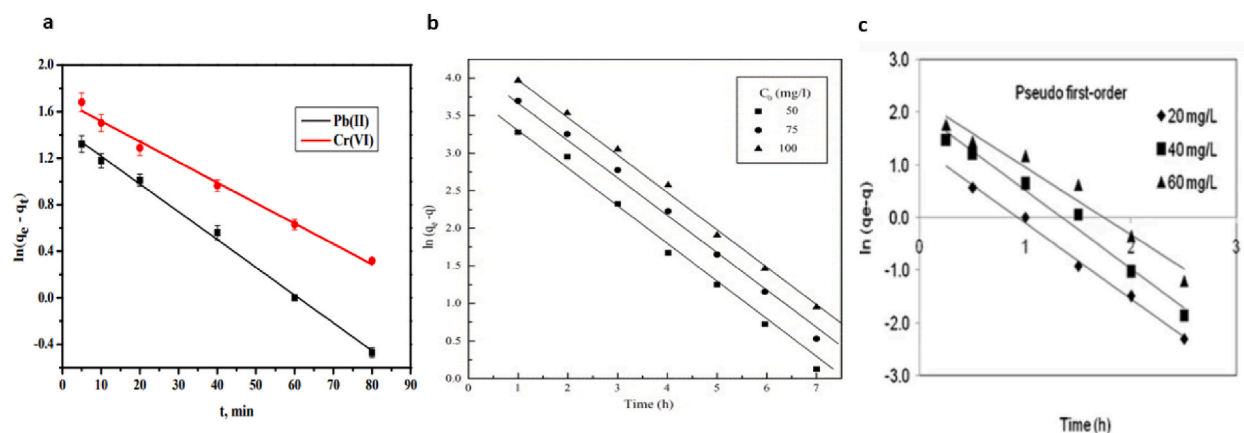
Fig. 9. Pseudo-first-order kinetic model of biomass-derived activated carbon adsorbents for Cr(VI) adsorption **(a)** Juniperus procera Leaves-H$_2$SO$_4$ acid AC [107], **(b)** Phosphoric acid-treated tamarind hull activated carbon [131], and **(c)** KOH/HCl activated CCAC [139].
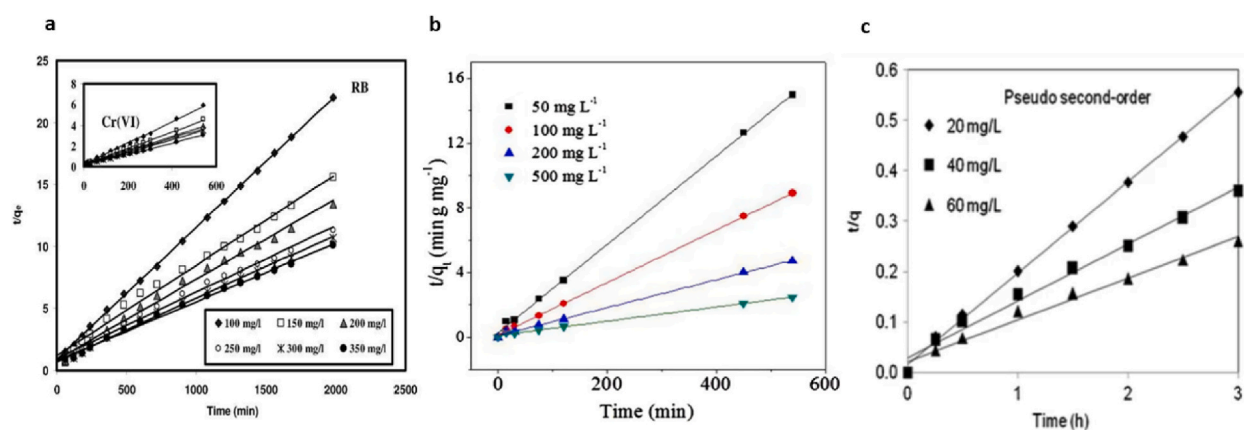

Fig. 10. Pseudo-second-order kinetic model of biomass-derived activated carbon adsorbents for Cr(VI) adsorption **(a)** HCl modified Cashew husk based tannery residual biomass-derived activated carbon [134], **(b)** PEI–alkali–biochar with various initial Cr(VI) concentration [130], and **(c)** KOH/HCl activated CCAC [139].

Furthermore, it was also observed that the increase in initial Cr(VI) concentration significantly enhances the amount of qe. Most biosorbents, including Mango kernel bio-composite (fruit waste biosorbent) [112], Rhizopus sp. (fungal biosorbent) [119], Rhizopus sp.+NaCl (fungal biosorbent) [119], Artist's Bracket (fungal biosorbent) [120], Arthrinium malaysianum (fungal biosorbent) [121], Melaleuca diosmifolia leaf (leaf biosorbent) (Fig. 6 (c)) [122], Magnolia leaf (leaf biosorbent) [123], Gliricidia sepium Leaf (GSL) Powder (leaf biosorbent) [114], Mangrove leaf powder (leaf biosorbent) [124], Azadirachta Indica (Neem) Leaf Powder (leaf biosorbent) [115], NCBC (biochar) [125], NZCBC (biochar) [125], and ACBC (biochar) [125], followed the chemical sorption as indicated by their higher R^2 values of the pseudo-second-order kinetic model. Moreover, pseudo-second-order kinetics modeling of biosorbents better described the experimental values than the pseudo-first-order kinetic model except for the *Cladosporium cladosporioides* (fungal biosorbent) [106], Aspergillus fumigatus (fungal biosorbent) [113], which followed the pseudo-first-order kinetic model as shown in Fig. 5 (b) and Fig. 5 (c) due to its higher R^2 value as compared to R^2 value of pseudo-second-order kinetics model as shown in Fig. 6 (b) [106].

Additionally, Cr(VI) adsorption by biosorbents such as grape waste (fruit waste biosorbent) [118], olive waste (fruit waste biosorbent) [118], oak wood char (biochar) [116], and oak bark char (biochar) [116] showed a complex process involving more than one mechanism as these biosorbents followed both the pseudo-first-order kinetic model and pseudo-second-order kinetic models.

4.2. Biomass-derived activated carbon adsorbents

Biomass-derived activated carbon (AC) is an adsorbent material for heavy metal removal. It is mainly used as an adsorbent material due to its larger microporous and mesoporous volumes and higher surface area. Researchers are working on activated carbon to remove heavy metals [126,127]. Commercial activated carbons and biomass-waste-derived activated carbons, such as nutshell-derived activated carbon, are examples of activated carbon-based adsorbents [57], wood apple shell-derived activated carbon

Table 6
Langmuir and Freundlich adsorption isotherm constants obtained for Cr(VI) heavy metal adsorption by using Nanocomposites as adsorbent.

Adsorbent type	Adsorbent	Source of Cr(VI)	Initial Cr(VI) Conc. (mg/l)	T/K	pH	Cont. t (min)	Dose (g/L)	Exp. q_m (mg/g)	Langmuir				Freundlich			Isotherm Model	Ref
									q_m (mg/g)	K_L (L/mg)	R^2	R_L	K_F	n	R^2		
Fe-based nanocomposite	Chi@Fe$_3$O$_4$ nanocomposite	Cr(VI) aqueous solution of K$_2$Cr$_2$O$_7$	40	295	2	180	0.5	–	142.381	0.24	0.969	0.041–0.303	53.151	4.012	0.984	F	[150]
	Peganum harmala seed based GnZVI/PAC	Cr(VI) aqueous solution of K$_2$Cr$_2$O$_7$	25-100	283-323	2	5-80	1-10	–	53.48	1.8	0.949	–	27.11	2.82	0.923	L	[151]
	IO@CaCO$_3$	Simulated wastewater (K$_2$CO$_3$, NaCl, MgSO$_4$, KH$_2$PO$_4$ and Ca(NO$_3$)$_2$ DI solution + As(V), Cr(VI) or Pb(II)	2.5–30	298	6.8 ± 0.2	9	2	–	303.4	0.011	0.9995	–	245.02	11.185	0.5786	L	[152]
	nZVI–Fe$_3$O$_4$ nanocomposites	Cr(VI) aqueous solution of K$_2$Cr$_2$O$_7$	40-120	303	3	120	1.3	–	100.00	6.10	0.993	–	14.43997	2.36	0.984	F	[153]
			20-80	303	8	120	1.3	–	29.43	6.21	0.997	–	14.15404	6.17	0.999	F	[153]
	PPY-γ-Fe$_2$O$_3$	Cr(VI) aqueous solution of K$_2$Cr$_2$O$_7$	50	RT	2	35	0.2	–	208.8	2.3	0.99	–	106.7	4.545	0.66	L	[154]
Mn-based nanocomposite	MnF-MO-NPs	Cr(VI) aqueous solution of K$_2$Cr$_2$O$_7$	100	303-338	2	60	0.125–1.5	–	91.24	1.58	0.99	(0.36–2.06) x10^2	49.40	5.85	0.82	L	[155]
	MnO$_2$/Fe$_3$O$_4$/o-MWCNTs	Cr(VI) aqueous solution of K$_2$Cr$_2$O$_7$	50-300	275	2	150	0.5	–	150.8	0.0191	0.998	0.149–0.511	12.342	2.114	0.921	L	[156]
			50-300	295	2	150	0.5	–	170.4	0.0175	0.974	0.160–0.533	11.727	2.132	0.895	L	[156]
			50-300	335	2	150	0.5	–	186.9	0.0164	0.970	0.168–0.549	13.479	2.347	0.866	L	[156]
Cu-based nanocomposite	CuO	Cr(VI) aqueous solution of K$_2$Cr$_2$O$_7$	20 [157]	298	3	180	1.6	–	15.625	0.0359	0.998	0.0182	7.667	6.451	0.946	L	[158]
			20 [157]	308	3	180	1.6	–	17.636	0.388	0.994	0.0168	8.944	6.493	0.926	L	[158]
			20 [157]	318	3	180	1.6	–	18.518	4.50	0.999	0.00147	11.279	7.751	0.940	L	[158]
Graphene-based nanocomposite	pssN-GO	Cr(VI) aqueous solution of K$_2$Cr$_2$O$_7$	5-100	298	–	1440	0.3	–	260.74	1.53	0.996	–	160.03	9.615	0.929	L	[159]
	psN-GO		5-100	298	–	1440	0.3	–	208.22	1.27	0.938	–	111.13	5.155	0.975	F	[159]
	pN-GO		5-100	298	–	1440	0.3	–	189.47	0.15	0.985	–	50.21	3.164	0.993	F	[159]
	mimGO sponge	Cr(VI) aqueous solution of K$_2$Cr$_2$O$_7$	10	296	2	360	1	–	208.3	0.03	0.99	–	5.8	5.263	0.9846	L	[160]
	GO sponge		10	296	2	360	1	–	123.5	1.8	0.9568	–	5.1	5.555	0.8964	L	[160]
	EDA-GO sponge		10	296	2	360	1	–	126.6	0.12	0.9515	–	4.8	4.545	0.9278	L	[160]
	MGO-Trp nanocomposite	Natural water samples (tap water, seawater, and industrial wastewater)	50-250	–	2	0.333	10	–	1000.0	2.163 × 10^{-5}	0.976	0.38–0.78	0.3478	1.208	0.999	F	[161]
	GO	Cr(VI) aqueous solution of K$_2$Cr$_2$O$_7$	5-80	–	4	1-60	0.005–0.01	–	1.222	1.305	0.981	–	3.625	12.195	0.899	L	[162]
	n-GO@HTCS biocomposite	Cr(VI) aqueous solution of K$_2$Cr$_2$O$_7$	100	303	3	0-100	2	–	46.23	0.777	0.999	0.374	35.28	1.654	0.890	L	[163]
			100	313	3	0-100	2	–	47.48	1.516	0.999	0.517	35.62	1.731	0.890	L	[163]
			100	323	3	0-100	2	–	47.83	1.665	0.999	0.622	36.33	1.888	0.908	L	[163]
	CS-GO	Cr(VI) aqueous solution of K$_2$Cr$_2$O$_7$	10-125	300	2	420	0.25	–	104.16	0.009	0.957	–	25.12	3.33	0.866	L	[164]
			10-125	300	2	420	0.5	–	59.17	0.108	0.983	–	13.81	3.17	0.942	L	[164]
			10-125	300	2	420	0.75	–	54.94	0.1	0.998	–	8.73	2.38	0.951	L	[164]
			10-125	300	2	420	1	–	47.16	0.081	0.955	–	6.60	2.33	0.963	F	[164]
			10-125	300	2	420	2	–	40.65	0.329	0.982	–	10.73	2.65	0.784	L	[164]
			10-125	300	2	420	3	–	27.54	0.357	0.965	–	7.54	2.67	0.763	L	[164]
	GFM	Cr(VI) aqueous solution of K$_2$Cr$_2$O$_7$	4.41	288-303	6.79	180	2.98	–	100	0.00006	0.97	0.013	1.69	3.09	0.933	L	[165]

Table 6 (*continued*)

Adsorbent type	Adsorbent	Source of Cr(VI)	Initial Cr (VI) Conc. (mg/l)	T/K	pH	Cont. t (min)	Dose (g/L)	Exp. q_m (mg/g)	Langmuir				Freundlich			Isotherm Model	Ref
									q_m (mg/g)	K_L (L/mg)	R^2	R_L	K_F	n	R^2		
	Chi@Fe$_3$O$_4$GO nanocomposite	Cr(VI) aqueous solution of K$_2$Cr$_2$O$_7$	40	295	2	180	0.5	–	100.514	0.36	0.968	0.027–0.217	40.373	4.495	0.985	L	[150]
	Fe$_3$O$_4$/G	Cr(VI) aqueous solution of K$_2$Cr$_2$O$_7$	50	298	–	–	2	–	78.5	0.000615	0.998	–	15.17	2.70	0.986	L	[166]
	Chitosan/CDTA/GO	Cr(VI) aqueous solution of K$_2$Cr$_2$O$_7$	25	298	3.5	60	1	–	166.98	–	0.987	–	–	–	0.956	L	[167]
	GO-1N	Cr(VI) aqueous solution of K$_2$Cr$_2$O$_7$	0.25	298	3.5	180	0.2	–	13.3 ± 0.61	1.46 ± 0.079	0.9969	–	8.0 ± 0.55	5.1 ± 0.28	0.9454	L	[168]
	GO-2N		0.25	298	3.5	180	0.2	–	15.1 ± 0.57	0.38 ± 0.035	0.9947	–	4.8 ± 0.42	2.4 ± 0.20	0.9770	L	[168]
	GO-3N		0.25	298	3.5	180	0.2	–	14.3 ± 0.69	0.57 ± 0.040	0.9820	–	5.9 ± 0.47	3.0 ± 0.27	0.9540	L	[168]
	RGO/NiO	Cr(VI) aqueous solution of K$_2$Cr$_2$O$_7$	100	298	4	–	0.333	–	198	–	0.9717	–	–	–	–	L	[169]

Chi@Fe$_3$O$_4$ nanocomposite = Magnetic chitosan nanocomposite; Peganum harmala seed based GnZVI/PAC= Peganum harmala seed based Green zero-valent iron nanoparticles/powdered activated carbon; IO@CaCO$_3$=Iron Oxide@Calcium Carbonate; PPY/γ-Fe$_2$O$_3$ = polypyrrole/maghemite nanocomposite; MnF-MO-NPs = Magnetic manganese ferrite and manganese oxide nanoparticles composite; CuO= Copper oxides nanocomposites; MnO2/Fe$_3$O$_4$/o-MWCNTs = Manganese dioxide/iron oxide/acid oxidized multi-walled carbon nanotube magnetic nanocomposite; nZVI–Fe$_3$O$_4$ nanocomposites = nanoscale zero-valent iron (nZVI)–Fe$_3$O$_4$ nanocomposites; pssN-GO = 3-[2-(2-aminoethylamino)ethylamino]propyl-trimethoxysilane GO (AEAEAPTMS-GO); psN-GO = [3-(2-aminoethylamino)propyl] trimethoxysilane Graphene Oxide (AEAPTMS-GO); pN-GO=(3-aminopropyl)trimethoxysilane Graphene Oxide (APTMS-GO); mimGO sponge = 1-aminopropyl-3- methylimidazolium bromide functionalized based graphene oxide sponge; GO sponge = Graphene oxide sponge; EDA-GO sponge = Ethylenediamine-Graphene Oxide sponge; MGO-Trp nanocomposite = Magnetic graphene oxide functionalized tryptophan; GO = graphene oxide nanocomposite; n-GO@HTCS biocomposite = nano-graphene oxide assisted hydrotalcite/chitosan biocomposite; CS-GO = chitosan grafted graphene oxide; GFM = magnetic graphene oxide functionalized with 2-mercaptobenzothiazole; Chi@Fe$_3$O$_4$GO nanocomposite = Graphene oxide modified magnetic chitosan nanocomposite; Fe$_3$O$_4$/G = Fe$_3$O$_4$ nanoparticles hybridized with graphene; Chitosan/CDTA/GO = Chitosan-1,2-Cyclohexylenedinitrilotetraacetic acid-graphene oxide; GO-1N = Graphene oxide modified with (C$_2$H$_5$O)$_3$Si(CH$_2$)$_3$NH$_2$; GO-2N = Graphene oxide modified with (CH$_3$O)$_3$Si(CH$_2$)$_3$NH(CH$_2$)$_2$NH$_2$; GO-3N = Graphene oxide modified with (CH$_3$O)$_3$Si(CH$_2$)$_3$NH(CH$_2$)$_2$NH(CH$_2$)$_2$NH$_2$; RGO/NiO=Reduced graphene oxide/NiO; L = Langmuir adsorption isotherm; F=Freundlich adsorption isotherm.
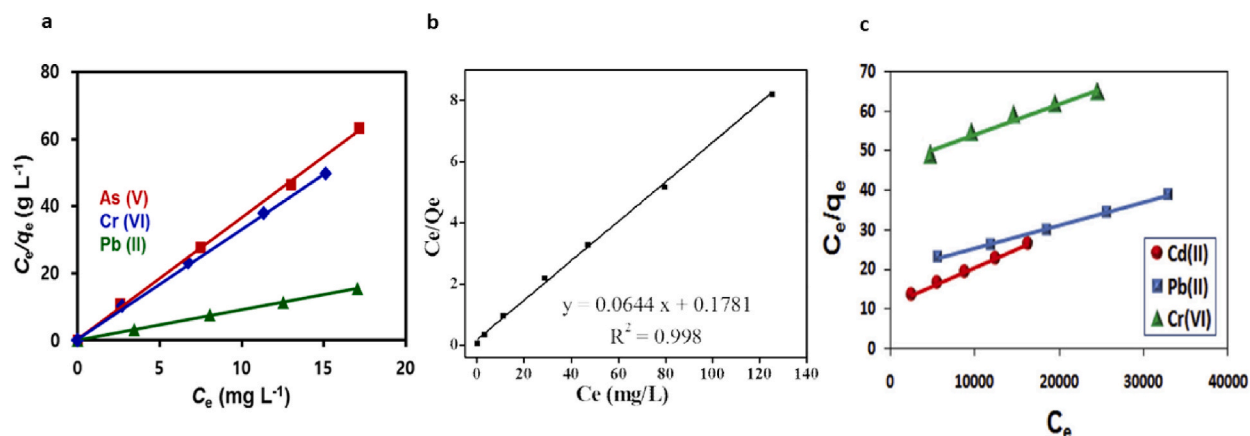
Fig. 11. Langmuir Isotherm of nanocomposite adsorbents for Cr(VI) adsorption **(a)** IO@CaCO$_3$ (Needle-like Iron Oxide@Calcium Carbonate) [172], **(b)** CuO nanoparticles [158], and (c) MGO-Trp nanocomposite [161].

[58], and mango kernel-derived activated carbon [59]. Termite feces-derived activated carbon [60]. As commercial activated carbons are expensive, researchers focus on generating activated carbon using low-cost biomass waste adsorbents [58,59,128]. Nanomaterials range from 1 to 100 nm, offering various unique features, including optical, mechanical, and magnetic properties [61]. They commonly use adsorbent materials due to the large surface area-to-volume ratio [129].

4.2.1. Biomass-derived activated carbon adsorbents and Langmuir adsorption isotherm

The maximum adsorption capacity depends on the type of chemical treatment of activated carbon adsorbents. Several activated carbon adsorbents have been used, including acid-treated activated carbon, base-treated activated carbon, and acid/base-treated activated carbon for Cr(VI) adsorption. The Langmuir adsorption isotherms of the activated carbon adsorbents are evaluated based on the maximum adsorption capacity, Langmuir constant (K_L), and R^2 value. The PEI-KOH alkali-rice husk exhibits the best maximum adsorption capacity of activated carbon adsorbents derived biochar (base-treated activated carbon) while representing the mono-layer adsorption shown by the R^2 value approaching unity [130]. It is evident from the literature cited in Table 4 that all activated carbon adsorbents followed the monolayer adsorption. However, the NaOH/HCl-activated P. terebinthus L oily seeds (acid/base activated carbon adsorbent) show the lowest maximum adsorption capacities following the mono-layer adsorption mechanisms [125]. Hence, it can be stated that the maximum adsorption capacity depends on the type of chemical treatment of the activated carbon adsorbents. However, phosphoric acid-treated tamarind hull (acid-treated activated carbon adsorbent) resulted in the highest Langmuir constant (K_L) value indicating a stronger interaction between Cr(VI) and phosphoric acid-treated tamarind hull (acid-treated activated carbon adsorbent) [131] among other types of activated carbons. Therefore, base-treated activated carbon adsorbents result in the best results of Langmuir adsorption isotherms for Cr(VI) adsorption but have a drawback of lower K_L value showing weaker interaction between Cr (VI) and base-treated activated carbon adsorbent.

The Langmuir adsorption isotherms for Cr(VI) adsorption by using biomass-derived activated carbons as an adsorbent are presented in Fig. 7. The Langmuir adsorption isotherm constants obtained for Cr(VI) heavy metal adsorption by using biomass-derived
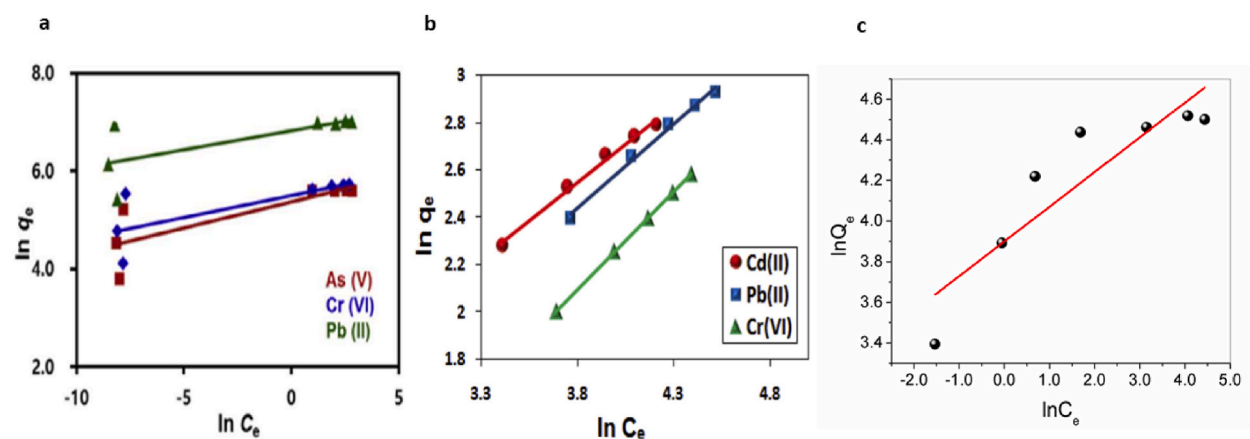

Fig. 12. Freundlich Isotherm of nanocomposite adsorbents for Cr(VI) adsorption **(a)** IO@CaCO$_3$ (Needle-like Iron Oxide@Calcium Carbonate) [172], **(b)** MGO-Trp nanocomposite [161], and **(c)** MnF-MO-NPs (Mn-based nanocomposite) [155].

Table 7

Pseudo-first-order and pseudo-second-order kinetic model constants obtained for Cr(VI) heavy metal adsorption by nanocomposite adsorbents.

Adsorbent type	Adsorbent	Initial Cr(VI) Conc. (mg/l)	T/K	pH	Dose (g/L)	$q_{e,exp}$ (mg/g)	Pseudo-first order kinetic model			Pseudo-second order kinetic model			Kinetic Model	Ref
							$q^{I}_{e,cal}$ (mg/g)	k_1 (1/min)	R^2	$q^{II}_{e,cal}$ (mg/g)	k_2 (g/mg.min)	R^2		
Fe-based nanocomposite	Chi@Fe$_3$O$_4$ nanocomposite	40	295	2	0.5	–	69.457	0.194	0.976	79.466	0.005	0.995	PSO	[150]
	Cr(VI) Peganum harmala seed-based GnZVI/PAC solution	25-100	283-323	2	1-10	–	13.39	0.064	0.74	27.32	0.0089	0.996	PSO	[151]
	IO@CaCO$_3$	10	298	6.8 ± 0.2	2	–	180.09	0.6073	0.8030	256.41	0.0029	0.9976	PSO	[152]
	nZVI–Fe$_3$O$_4$ nanocomposites	20	303	8	1.3	–	–	–	–	15.5	0.052	0.999	PSO	[153]
		40	303	8	1.3	–	–	–	–	21.28	0.023	0.999	PSO	[153]
		60	303	8	1.3	–	–	–	–	24.39	0.011	0.999	PSO	[153]
		80	303	8	1.3	–	–	–	–	26.32	0.013	0.999	PSO	[153]
		20	303	7	1.3	–	–	–	–	16.05	0.588	1	PSO	[153]
		20	303	9	1.3	–	–	–	–	4.61	0.049	0.997	PSO	[153]
		20	303	10	1.3	–	–	–	–	5.89	0.045	0.996	PSO	[153]
		20	303	11	1.3	–	–	–	–	3.58	0.05	0.99	PSO	[153]
	PPY/ γ-Fe$_2$O$_3$	50	RT	2	0.2	208.8	5.8	0.019	0.49	207.9	0.02	0.99	PSO	[154]
Mn-based nanocomposite	MnF-MO-NPs	30	303-338	2	0.75	39.38	29.35	1180	0.97	40.16	8520	0.99	PSO	[155]
		50	303-338	2	0.75	64.74	56.54	1280	0.93	65.79	4680	0.99	PSO	[155]
		70	303-338	2	0.75	81.20	60.89	1020	0.93	84.32	3490	0.99	PSO	[155]
		90	303-338	2	0.75	93.34	60.80	870	0.98	95.23	3180	0.99	PSO	[155]
		110	303-338	2	0.75	104.45	68.62	900	0.94	109.90	2740	0.99	PSO	[155]
	MnO$_2$/Fe$_3$O$_4$/o-MWCNTs	100	275	2	0.5	56.8	94.1	0.0221	0.854	74.1	0.652	0.972	PSO	[156]
		200	295	2	0.5	117.1	263.1	0.0349	0.831	147.9	0.959	0.976	PSO	[156]
		300	335	2	0.5	135.6	148.8	0.0202	0.947	157.7	1.412	0.992	PSO	[156]
Cu-based nanocomposite	CuO	20[157]	298	3	1.6	–	5.566	0.0287	0.982	11.111	0.00955	0.998	PSO	[158]
Graphene-based nanocomposite	pssN-GO	50	298	–	0.2	–	201.91	0.0295	0.963	221.82	0.0002	0.987	PSO	[159]
	mimGO sponge	10	296	2	0.25	16.0	7.8	0.007	0.7894	16.2	0.005	0.9942	PSO	[160]
		10	296	2	0.5	13.2	6.3	0.006	0.8069	13.2	0.006	0.9928	PSO	[160]
		10	296	2	1	9.8	4.5	0.0051	0.7272	9.8	0.008	0.9916	PSO	[160]
		10	296	2	1.5	6.7	2	0.0044	0.3204	6.8	0.02	1	PSO	[160]
	MGO-Trp nanocomposite	50-250	–	2	10	1000	1096.6	0.337	0.949	1010	0.000491	0.990	PSO	[161]
	GO	5-80	–	4	0.005–0.01	–	12.389	0.03376	0.863	0.692	0.26954	0.780	PFO	[162]
	CS-GO	20	300	2	2	11.78	9.82	0.00898	0.862	12.25	0.029	0.983	PSO	[164]
		50	300	2	2	23.15	18.86	0.00713	0.927	23.69	0.038	0.997	PSO	[164]
		75	300	2	2	27.35	18.97	0.0086	0.974	28.16	0.04	0.997	PSO	[164]
		100	300	2	2	33.45	14.54	0.00736	0.948	33.89	0.048	0.995	PSO	[164]

Table 7 (*continued*)

Adsorbent type	Adsorbent	Initial Cr(VI) Conc. (mg/l)	T/K	pH	Dose (g/L)	$q_{e,exp}$ (mg/g)	Pseudo-first order kinetic model			Pseudo-second order kinetic model			Kinetic Model	Ref
							$q_{e,cal}^{I}$ (mg/g)	k_1 (1/min)	R^2	$q_{e,cal}^{II}$ (mg/g)	k_2 (g/mg. min)	R^2		
	GFM	3	288-303	6.79	2.98	0.58	1.28	0.018	0.956	3.84	0.0039	0.955	PFO	[165]
		6	288-303	6.79	2.98	1.14	3.16	0.011	0.995	20	0.00011	0.908	PFO	[165]
		9	288-303	6.79	2.98	1.5	5.74	0.013	0.994	20	0.00011	0.972	PFO	[165]
	Chi@Fe$_3$O$_4$GO nanocomposite	40	295	2	0.5	–	76.098	0.265	0.965	73.164	0.006	0.985	PSO	[150]
	Chitosan/CDTA/GO	20	298	3.5	1	18.66	3.52	0.0041	0.86	18.18	0.014	0.999	PSO	[167]
		40	298	3.5	1	35.86	14.06	0.0066	0.944	36.76	0.002	0.999	PSO	[167]
		60	298	3.5	1	46.22	13.98	0.0049	0.985	47.16	0.0089	0.998	PSO	[167]
	GO-1N	0.25	298	3.5	0.25	–	–	–	–	1.206 ± 0.005	0.12 ± 0.02	1	PSO	[168]
		0.25	298	3.5	0.17	–	–	–	–	1.24 ± 0.01	0.07 ± 0.01	0.9997	PSO	[168]
		0.25	298	3.5	0.13	–	–	–	–	1.239 ± 0.007	0.050 ± 0.003	0.9999	PSO	[168]
		0.25	298	3.5	0.08	–	–	–	–	1.288 ± 0.008	0.030 ± 0.001	0.9999	PSO	[168]
		0.25	298	3.5	0.06	–	–	–	–	1.34 ± 0.02	0.017 ± 0.001	0.9995	PSO	[168]
		0.25	298	3.5	0.05	–	–	–	–	1.31 ± 0.04	0.014 ± 0.001	0.9976	PSO	[168]
	GO-2N	0.25	298	3.5	0.25	–	–	–	–	1.073 ± 0.004	0.13 ± 0.01	1	PSO	[168]
		0.25	298	3.5	0.17	–	–	–	–	1.114 ± 0.009	0.065 ± 0.007	0.9998	PSO	[168]
		0.25	298	3.5	0.13	–	–	–	–	1.108 ± 0.008	0.060 ± 0.005	0.9999	PSO	[168]
		0.25	298	3.5	0.08	–	–	–	–	1.14 ± 0.01	0.038 ± 0.003	0.9998	PSO	[168]
		0.25	298	3.5	0.06	–	–	–	–	1.17 ± 0.03	0.026 ± 0.003	0.9987	PSO	[168]
		0.25	298	3.5	0.05	–	–	–	–	1.18 ± 0.07	0.019 ± 0.005	0.9921	PSO	[168]
	GO-3N	0.25	298	3.5	0.25	–	–	–	–	1.091 ± 0.003	0.34 ± 0.06	1	PSO	[168]
		0.25	298	3.5	0.17	–	–	–	–	1.052 ± 0.006	0.52 ± 0.03	0.9999	PSO	[168]

Table 7 (*continued*)

Adsorbent type	Adsorbent	Initial Cr(VI) Conc. (mg/l)	T/K	pH	Dose (g/L)	$q_{e,exp}$ (mg/g)	Pseudo-first order kinetic model			Pseudo-second order kinetic model			Kinetic Model	Ref
							$q_{e,cal}^{I}$ (mg/g)	k_1 (1/min)	R^2	$q_{e,cal}^{II}$ (mg/g)	k_2 (g/mg. min)	R^2		
		0.25	298	3.5	0.13	–	–	–	–	1.056 ± 0.005	0.27 ± 0.06	0.9999	PSO	[168]
		0.25	298	3.5	0.08	–	–	–	–	1.09 ± 0.01	0.07 ± 0.01	0.9997	PSO	[168]
		0.25	298	3.5	0.06	–	–	–	–	1.10 ± 0.01	0.043 ± 0.005	0.9996	PSO	[168]
		0.25	298	3.5	0.05	–	–	–	–	1.08 ± 0.02	0.03 ± 0.04	0.9988	PSO	[168]
	RGO/NiO	100	298	4	0.333	–	–	–	–	–	–	–	PSO	[169]

Chi@Fe$_3$O$_4$ nanocomposite = Magnetic chitosan nanocomposite; Peganum harmala seed based GnZVI/PAC= Peganum harmala seed based Green zero-valent iron nanoparticles/powdered activated carbon; IO@CaCO$_3$=Iron Oxide@Calcium Carbonate; PPY/γ-Fe$_2$O$_3$ = polypyrrole/maghemite nanocomposite; MnF-MO-NPs = Magnetic manganese ferrite and manganese oxide nanoparticles composite; CuO= Copper oxides nanocomposites; MnO2/Fe$_3$O$_4$/o-MWCNTs = Manganese dioxide/iron oxide/acid oxidized multi-walled carbon nanotube magnetic nanocomposite; nZVI–Fe$_3$O$_4$ nanocomposites = nanoscale zero-valent iron (nZVI)–Fe$_3$O$_4$ nanocomposites; pssN-GO = 3-[2-(2-aminoethylamino)ethylamino]propyl-trimethoxysilane GO (AEAEAPTMS-GO); psN-GO = [3-(2-aminoethylamino)propyl] trimethoxysilane Graphene Oxide (AEAPTMS-GO); pN-GO=(3-aminopropyl)trimethoxysilane Graphene Oxide (APTMS-GO); mimGO sponge = 1-aminopropyl-3- methylimidazolium bromide functionalized based graphene oxide sponge; GO sponge = Graphene oxide sponge; EDA-GO sponge = Ethylenediamine-Graphene Oxide sponge; MGO-Trp nanocomposite = Magnetic graphene oxide functionalized tryptophan; GO = graphene oxide nanocomposite; n-GO@HTCS biocomposite = nano-graphene oxide assisted hydrotalcite/chitosan biocomposite; CS-GO = chitosan grafted graphene oxide; GFM = magnetic graphene oxide functionalized with 2-mercaptobenzothiazole; Chi@Fe$_3$O$_4$GO nanocomposite = Graphene oxide modified magnetic chitosan nanocomposite; Fe$_3$O$_4$/G = Fe$_3$O$_4$ nanoparticles hybridized with graphene; Chitosan/CDTA/GO = Chitosan-1,2-Cyclohexylenedinitrilotetraacetic acid-graphene oxide; GO-1N = Graphene oxide modified with (C$_2$H$_5$O)$_3$Si(CH$_2$)$_3$NH$_2$; GO-2N = Graphene oxide modified with (CH$_3$O)$_3$Si(CH$_2$)$_3$NH(CH$_2$)$_2$NH$_2$; GO-3N = Graphene oxide modified with (CH$_3$O)$_3$Si(CH$_2$)$_3$NH(CH$_2$)$_2$NH(CH$_2$)$_2$NH$_2$; RGO/NiO=Reduced graphene oxide/NiO; PFO= Pseudo-first-order kinetic model; PSO= Pseudo-second-order kinetic model.

activated carbon as an adsorbent are listed in Table 4.

The maximum adsorption capacity, Langmuir constant (K_L) and R^2 depend on the type of biomass-derived activated carbon used, such as (acid-treated, based-treated, and acid/base-treated). The HCl modified cashew husk based tannery residual biomass (acid-treated activated carbon) resulted in the best langmuir adsorption isotherms for Cr(VI) adsorption as represented by its highest maximum adsorption capacity and R^2 value approaching unity indicating the well-fitting of the Langmuir isotherm with the experimental adsorption capacity [134] among other acid-treated activated carbon adsorbents cited in Table 4 such as juniperus procera Leaves-H_2SO_4 acid AC [107] as shown in Fig. 7 (a), phosphoric acid activated leucaena leucocephala waste sawdust based activated carbon [132], H_2SO_4 activated F. nitida leaves derived activated carbon [133], PEI-HNO_3 acid-rice husk derived biochar based activated carbon [130], sulphuric acid treated sunflower head activated carbon [135], phosphoric acid treated bael fruit shell activated carbon [136], H_2SO_4 treated Tamarind seeds activated carbon [137] as shown in Fig. 7 (b), and phosphoric acid treated tamarind hull activated carbon [131]. Furthermore, it can be interpreted from the R^2 value approaching unity that the HCl-modified cashew husk-based tannery residual biomass (acid-treated activated carbon) follows a mono-layer adsorption mechanism. However, the lower value of Langmuir constant (K_L) of HCl-modified cashew husk-based tannery residual biomass (acid-treated activated carbon) [134] showed weaker interactions between Cr(VI) and HCl-modified cashew husk-based tannery residual biomass (acid-treated activated carbon adsorbent).

However, the PEI-KOH alkali-rice husk-derived biochar (base-treated activated carbon adsorbent) resulted in the best Langmuir adsorption isotherms for Cr(VI) adsorption as represented by its maximum adsorption capacity and R^2 value approaching unity indicated that the Langmuir adsorption isotherm fits well with the experimental adsorption capacity value [130] as compared to another base-treated activated carbon adsorbent such as KOH activated Chickpea-husk (base-treated activated carbon adsorbent) [101]. Furthermore, it can be interpreted from the R^2 value approaching unity that the PEI-KOH alkali-rice husk-derived biochar (base-treated activated carbon adsorbent) follows a mono-layer adsorption mechanism. The Langmuir constant (K_L), smaller than unity and closely approaching zero, indicates one of the weakest interactions between Cr(VI) and PEI-KOH alkali-rice husk-derived biochar (base-treated activated carbon adsorbent) [130]. It has been interpreted that the base-treated activated carbons follow the monolayer adsorption mechanism; however, observing weaker interactions between Cr(VI) and base-treated activated carbons.

The KOH/HCl activated CCAC (acid/base-treated activated carbon adsorbent) resulted in good Langmuir adsorption isotherms for Cr(VI) adsorption as represented by its maximum adsorption capacity and R^2 value approaching unity, indicating that the Langmuir adsorption isotherm fits well with the experimental adsorption capacity value [139] as shown in Fig. 7 (c) than another acid/base-treated activated carbon adsorbent such as NaOH/HCl activated P. terebinthus L oily seeds based activated carbon (acid/base-treated activated carbon adsorbent) [125]. Furthermore, it can be interpreted from the R^2 value approaching unity that the KOH/HCl activated CCAC (acid/base-treated activated carbon adsorbent) follows a mono-layer adsorption mechanism. The Langmuir constant (K_L), smaller than unity and closely approaching zero, indicates one of the weakest interactions between Cr(VI) and KOH/HCl activated CCAC (acid/base-treated activated carbon adsorbent) [139]. It has been interpreted that the acid/base-treated activated carbons follow the monolayer adsorption mechanism; however, observing weaker interactions between Cr(VI) and acid/base-treated activated carbons.

It can be concluded that the best Langmuir adsorption isotherm results for Cr(VI) adsorption are represented by PEI-KOH alkali-rice husk-derived biochar (base-treated activated carbon adsorbent) as indicated by its highest maximum adsorption capacity and R^2 value but with a lower K_L value representing weaker interactions between Cr(VI) and adsorbent. However, the best interaction between Cr(VI) and activated carbon is shown by phosphoric acid-treated tamarind hull (acid-treated activated carbon adsorbent), as demonstrated by the highest Langmuir constant (K_L) value.
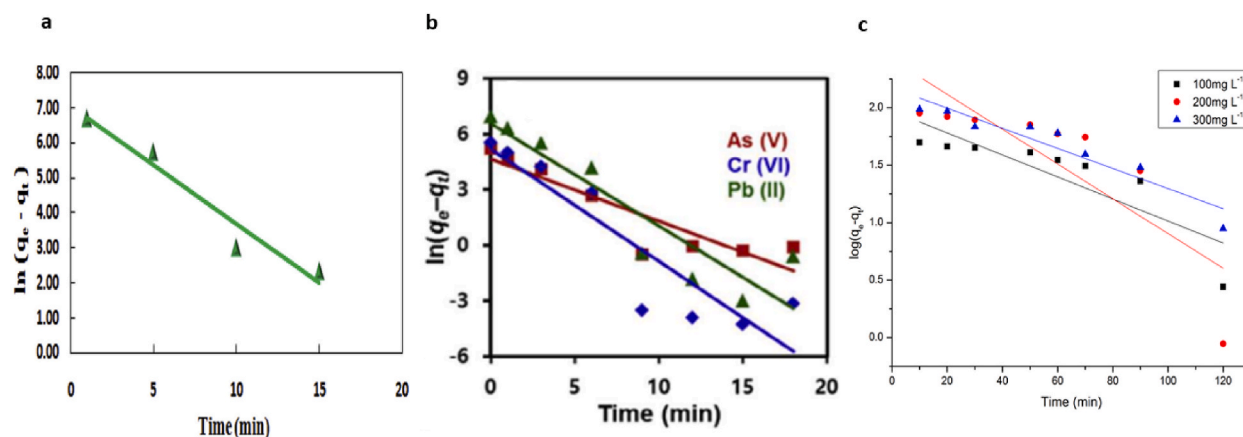

Fig. 13. Pseudo-first-order kinetic model of nanocomposite adsorbents for Cr(VI) adsorption **(a)** MGO-Trp nanocomposite [161], **(b)** IO@CaCO$_3$ [152], and **(c)** MnO$_2$/Fe$_3$O$_4$/o-MWCNTs [156].

4.2.2. Biomass-derived activated carbon adsorbents and Freundlich adsorption isotherm

The adsorption capacity on heterogenous sites of an adsorbent (K_F) depends on the type of biomass-derived activated carbon used, such as (acid-treated activated carbon, based-treated activated carbon, and acid/base-treated activated carbon). The Freundlich adsorption isotherms for Cr(VI) adsorption using biomass-derived activated carbon adsorbents are presented in Fig. 8. However, the Freundlich adsorption isotherm constants obtained for Cr(VI) heavy metal adsorption by using biomass-derived activated carbon as adsorbents are listed in Table 4.

It can be observed from Table 4 that the HCl-modified cashew husk-based tannery residual biomass (acid-treated activated carbon) resulted in the highest value of K_F for Cr(VI) adsorption. However, the value of R^2 for Cr(VI) adsorption using this type of activated carbon through Freundlich adsorption isotherm is lower than Langmuir adsorption isotherm [134]. However, the lowest value of K_F is shown by KOH-activated Chickpea-husk-derived activated carbon (base-treated activated carbon) [138] among other activated carbon adsorbents.

Furthermore, it can be interpreted from the adsorption intensity (n) of the biomass-derived activated carbon that the adsorption of Cr(VI) adsorption is majorly a chemical process except for Juniperus procera Leaves-H_2SO_4 acid AC which indicates the Cr(VI) adsorption as a physical process as shown in Fig. 8 (a) [107].

Moreover, phosphoric acid-activated Leucaena leucocephala waste sawdust-based activated carbon (acid-treated activated carbon) [132], phosphoric acid-treated bael fruit shell activated carbon (acid-treated activated carbon) [136], phosphoric acid-treated tamarind hull activated carbon (acid-treated activated carbon) [131], H_2SO_4 treated Tamarind seeds activated carbon (acid-treated activated carbon) (Fig. 8 (b)) [137], and KOH activated Chickpea-husk-derived activated carbon (base-treated activated carbon) [138] followed the multi-layer adsorption of Cr(VI) on the heterogenous surface of these activated carbon adsorbents due to their higher R^2 values of Freundlich adsorption isotherms than Langmuir adsorption isotherms. In contrast, Freundlich adsorption isotherm modelling of Juniperus procera Leaves-H_2SO_4 acid AC (acid-treated activated carbon) [107], phosphoric acid-activated Leucaena leucocephala waste sawdust based activated carbon (acid-treated activated carbon) [132], H_2SO_4 activated F. nitida leaves derived activated carbon (acid-treated activated carbon) [133], PEI-HNO_3 acid-rice husk derived biochar based activated carbon (acid-treated activated carbon) [130], HCl modified Cashew husk based tannery residual biomass-derived activated carbon (acid-treated activated carbon) [134], Sulphuric acid treated sunflower head activated carbon (acid-treated activated carbon) [135], Sulphuric acid-treated sunflower stem activated carbon (acid-treated activated carbon) [135], PEI-KOH alkali-rice husk derived biochar based activated carbon (base-treated activated carbon) [130], and KOH/HCl activated CCAC (acid-base treated activated carbon) [139] (Fig. 8 (c)) followed the mono-layer adsorption as their adsorption data fitted well with a Langmuir adsorption isotherm model rather than Freundlich adsorption isotherm model.

4.2.3. Biomass-derived activated carbon adsorbents and pseudo-first order and pseudo-second order kinetic models

The experimental amount of adsorbate adsorbed at equilibrium ($q_{e,exp}$) depends on the type of biomass-derived activated carbon adsorbent used, such as acid-treated activated carbon, base-treated activated carbon, and acid/base-treated activated carbon for Cr(VI) adsorption. The pseudo-first-order (PFO) and pseudo-second-order (PSO) kinetic models of biomass-derived activated carbon adsorbents for Cr(VI) adsorption were evaluated using the experimental and calculated amounts of Cr(VI) adsorbed at equilibrium ($q_{e,exp}$, $q_{e,cal}^I$, and $q_{e,cal}^{II}$), as well as the pseudo-first-order rate constant (k_1), pseudo-second-order rate constant (k_2) and R^2 value. Table 5 lists the experimental and calculated amounts of Cr(VI) adsorbed at equilibrium, pseudo-first-order and pseudo-second-order rate constants, and R^2 values obtained for various biomass-derived activated carbon adsorbents for Cr(VI) adsorption.

The linear pseudo-first-order kinetic and linear pseudo-second-order kinetic models of biomass-derived activated carbon adsorbents for Cr(VI) adsorption are shown in Figs. 9 and 10, respectively.

The PEI-KOH alkali-rice husk derived biochar based activated carbons (base-treated activated carbon) exhibited the highest experimental and calculated amounts of Cr(VI) adsorbed at equilibrium by the pseudo-second-order kinetic model ($q_{e,exp}$, and $q_{e,cal}^{II}$)
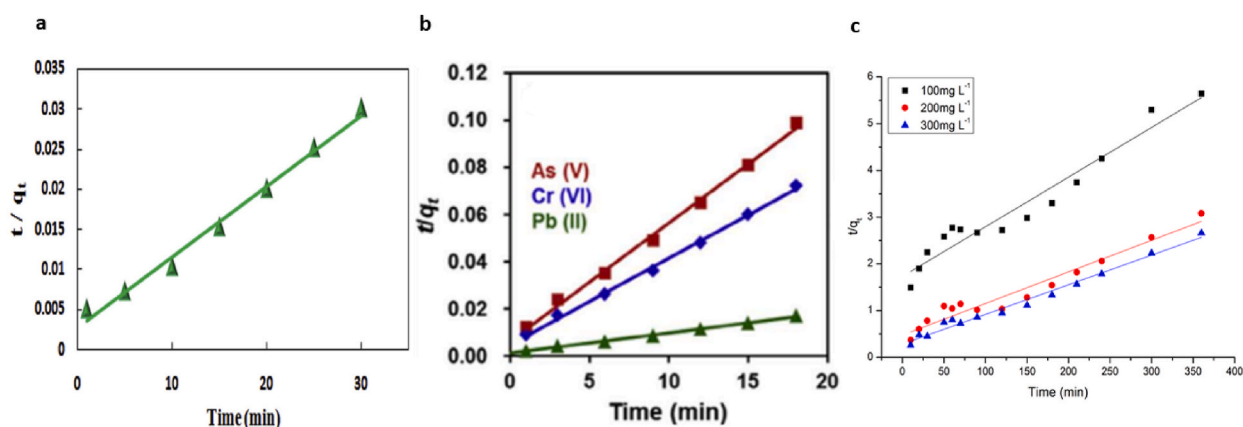

Fig. 14. Pseudo-second-order kinetic model of nanocomposite adsorbents for Cr(VI) adsorption (a) MGO-Trp nanocomposite [161], (b) IO@CaCO3 [152], and (c) MnO2/Fe3O4/o-MWCNTs [156].

Table 8
Langmuir and Freundlich adsorption isotherm constants obtained for Cr(VI) heavy metal adsorption by using PANI polymer composites as adsorbent.

Adsorbent	Source of Cr (VI)	Initial Cr (VI) Conc. (mg/l)	T/ K	pH	Cont. t (min)	Dose (g/L)	Exp. q_m (mg/ g)	Langmuir				Freundlich			Isotherm model	Ref
								q_m (mg/g)	K_L (L/mg)	R^2	R_L	K_F	n	R^2		
PANi/SD/PEG	Cr(VI) aqueous solution of $K_2Cr_2O_7$	50	RT	2	30	5-80	–	3.2	0.691578	0.9994	–	–	4	0.9328	L	[172]
(PANI/PI)	Cr(VI)	20	298	1	300	0.4	–	70.08	2.70	0.999	–	43.17	5.46	0.946	L	[185]
microfiber	aqueous	20	313	1	300	0.4	–	81.43	2.96	0.999	–	50.96	5.24	0.971	L	[185]
membranes	solution of $K_2Cr_2O_7$	20	328	1	300	0.4	–	96.53	3.91	0.998	–	63.93	5.15	0.982	L	[185]
PPy-PANI/Fe_3O_4	Cr(VI)	100	288	2	270	1	–	243.90	0.191	0.9995	0.0195	101.30	6.05	0.8420	L	[186]
	aqueous	100	298	2	270	1	–	303.03	0.340	0.9994	0.0111	143.39	6.78	0.8872	L	[186]
	solution of	100	308	2	270	1	–	384.62	0.186	0.9990	0.02	132.26	4.63	0.7350	L	[186]
	$K_2Cr_2O_7$	100	318	2	270	1	–	434.78	0.25	0.9984	0.0150	157.69	4.61	0.5792	L	[186]
PANI nanosheets	Cr(VI)	10-60	298	2	–	0.2	–	263.2	2.262	0.9999	0.007314–0.01452[a]	192.9	8.078	0.9303	L	[187]
PANI nanotubes	aqueous	10-60	298	2	–	0.2	–	259.7	1.930	0.9973	0.008562–0.01698[a]	181.2	7.215	0.9973	L	[187]
PANI nanofibers	solution of $K_2Cr_2O_7$	10-60	298	2	–	0.2	–	248.8	1.853	0.9994	0.008914–0.01767[a]	182.2	8.787	0.9883	L	[187]
(PANI/EVOH) nanofiber	Cr(VI) aqueous	25–200	293	2	100	–	–	291.55	9.026×10^{-3}	0.95207	–	3.2846	1.1665	0.99859	F	[188]
composite	solution of	25–200	303	2	100	–	–	271.00	10.762×10^{-3}	0.91866	–	3.7386	1.1944	0.99969	F	[188]
membranes	$K_2Cr_2O_7$	25–200	313	2	100	–	–	278.55	11.098×10^{-3}	0.85419	–	3.973	1.1978	0.99924	F	[188]
		25–200	323	2	100	–	–	248.76	13.867×10^{-3}	0.87084	–	4.489	1.2281	0.99947	F	[188]
PANI	Cr(VI)	–	293	3	20	0.1	–	357.1	0.27	0.99	–	160.66	0.19	0.96	L	[189]
PANI@MoS_2	aqueous solution of $K_2Cr_2O_7$	–	293	3	20	0.1	–	526.3	0.98	0.99	–	134.59	0.07	0.93	L	[189]
PANI/LDHs	Cr(VI)	40	288	3	–	0.2	–	393.7	0.24	0.999	–	103.06	0.32	0.907	L	[190]
(LDHs/aniline	aqueous	40	303	3	–	0.2	–	434.78	0.45	0.999	–	154.21	0.26	0.868	L	[190]
mass ratio of 1:8)	solution of $K_2Cr_2O_7$	40	318	3	–	0.2	–	510.2	0.69	0.995	–	226.52	0.21	0.828	L	[190]
PANI/H-TNB (H-TNBs/aniline mol ratio of 1: 20)	Cr(VI) aqueous solution of $K_2Cr_2O_7$	20	298	5	–	0.3	–	156.9	0.156	0.971	–	50.56	4.00	0.923	L	[191]
PANI/PVA	Cr(VI)	200-250	303	4	60	2	–	111.23	0.725	0.999	0.005	81.801	12.987	0.995	L	[192]
composite	aqueous	200-250	313	4	60	2	–	–	–	–	–	82.695	0.083	0.946	F	[192]
		200-250	323	4	60	2	–	–	–	–	–	83.416	0.088	0.980	F	[192]

(*continued on next page*)

Table 8 (*continued*)

Adsorbent	Source of Cr (VI)	Initial Cr (VI) Conc. (mg/l)	T/ K	pH	Cont. t (min)	Dose (g/L)	Exp. q_m (mg/ g)	Langmuir				Freundlich			Isotherm model	Ref
								q_m (mg/g)	K_L (L/mg)	R^2	R_L	K_F	n	R^2		
SA-PANI	solution of $K_2Cr_2O_7$ Cr(VI) aqueous solution of $K_2Cr_2O_7$	100	303	4.2	60	2	–	73.34	0.049	0.993	0.091	15.47	3.285	0.992	F	[193]
		100	313	4.2	60	2	–	74.46	0.064	0.996	0.071	18.43	3.555	0.997	F	[193]
		100	323	4.2	60	2	–	75.82	0.100	0.995	0.047	24.50	4.226	0.994	L	[193]
PANI/ γ-Fe$_2$O$_3$	Cr(VI) aqueous solution of $K_2Cr_2O_7$	50	RT	2	35	0.2	–	195.7	3.0	0.99	–	100.8	4.545	0.65	L	[154]
PANI-MWCNT	Cr(VI) aqueous solution of $K_2Cr_2O_7$	20-100	288	4.5	600	0.5	–	28.25	0.56	0.967	–	14.45	4.70	0.984	F	[194]
		20-100	298	4.5	600	0.5	–	31.75	0.48	0.983	–	15.49	6.50	0.984	F	[194]
		20-100	308	4.5	600	0.5	–	36.76	0.41	0.929	–	23.3	9.56	0.984	F	[194]
PANI/PA composite	Cr(VI) aqueous solution of $K_2Cr_2O_7$	2.5–30	288	5.5	400	0.5	–	11.52	8.35	0.999	–	8.79	9.78	0.922	L	[195]
		2.5–30	298	5.5	400	0.5	–	14.79	1.77	0.996	–	10.14	8.22	0.945	L	[195]
		2.5–30	308	5.5	400	0.5	–	16.45	1.54	0.999	–	10.17	6.33	0.95	L	[195]

PANi/SD/PEG=Poly, aniline/polyethylene glycol, coated on sawdust; RT = Room Temperature; (PANI/PI) microfiber membranes = Dodecylbenzene sulfonic acid (DBSA) doped-polyaniline; (PANI) coated conductive polyimide (PI) microfiber membrane; PPy-PANI/Fe$_3$O$_4$ = Polypyrrole- Polyaniline/magnetic nanocomposite; PANI nanosheets = Polyaniline nanosheets; [a] The RL values with the initial Cr(VI) concentration (C0) of 30–60nullmg/l; PANI nanotubes = Polyaniline nanotubes; PANI nanofibers = Polyaniline nanofibers; (PANI/EVOH) nanofiber composite membranes= (polyaniline/ethylene vinyl alcohol) nanofiber composite membranes; PANI=Polyaniline; PANI@MoS$_2$=Polyaniline-Molybdenum disulfide; PANI/LDHs = Polyaniline/Layered Double Hydroxides; PANI/H-TNB = polyaniline/hydrogen-titanate nanobelt nanocomposite; PANI/PVA composite = polyaniline/Poly(vinyl acetate) composite; SA-PANI= Sodium alginate-polyaniline nanofibers; PANI/ γ -Fe$_2$O$_3$ = polyaniline/ maghemite nanocomposite; PANI-MWCNT = polyaniline-multiwalled carbon nanotubes; PANI/PA composite = polyaniline/palygorskite composites; L = Langmuir adsorption isotherm; F=Freundlich adsorption isotherm.
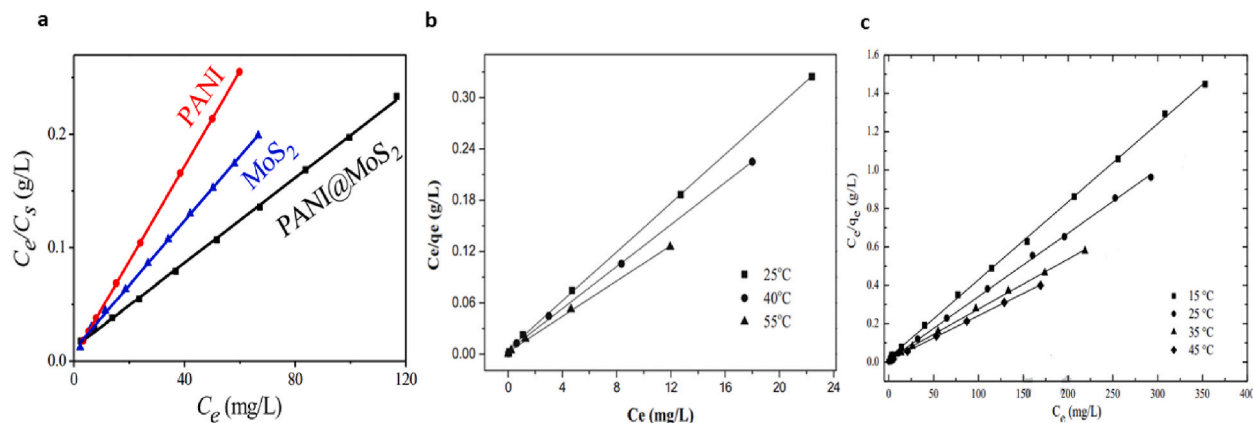
Fig. 15. Langmuir Isotherm of PANI polymer adsorbents for Cr(VI) adsorption **(a)** PANI, MoS_2 and PANI@MoS_2 [189], **(b)** PANI/PI microfiber membranes [185], and **(c)** PPy-PANI/Fe_3O_4 [186].

among acid-treated, base-treated and acid/base-treated activated carbons while following pseudo-second-order kinetic model indicating chemisorption of Cr(VI) on base-treated activated carbon [130].

The HCl modified Cashew husk based tannery residual biomass-derived activated carbon (acid-treated activated carbon) exhibited the highest experimental and calculated amounts of Cr(VI) adsorbed at equilibrium ($q_{e,exp}$, and $q_{e,cal}^{I}$) among acid-treated activated carbons, with the highest R^2 value of the pseudo-second-order kinetic model as shown in Fig. 10 (a) indicating chemical sorption involving valence forces through sharing or exchange of electrons between the acid-treated activated carbon and Cr(VI) as compared to pseudo-first-order kinetic model [134]. In contrast, the NaOH/HCl activated P. terebinthus L oily seeds-based activated carbon (acid/base-treated activated carbon) achieved the lowest experimental and calculated amounts of Cr(VI) adsorbed at equilibrium ($q_{e,exp}$, and $q_{e,cal}$) while observing the pseudo-second-order kinetic model [125].

Furthermore, it was also observed that the increase in initial Cr(VI) concentration significantly enhances the amount of qe. Most biomass-derived activated carbon adsorbents, including Phosphoric acid-activated Leucaena leucocephala waste sawdust based activated carbon (acid-treated activated carbon) [132], HCl modified Cashew husk based tannery residual biomass-derived activated carbon (acid-treated activated carbon) [134], Sulphuric acid treated sunflower head activated carbon (acid-treated activated carbon) [135], Sulphuric acid-treated sunflower stem activated carbon (acid-treated activated carbon) [135], Phosphoric acid-treated bael fruit shell activated carbon (acid-treated activated carbon) [136], PEI-KOH alkali-rice husk derived biochar based activated carbon (base-treated activated carbon) (Fig. 10 (b)) [130], KOH activated Chickpea-husk-derived activated carbon (base-treated activated carbon) [138], NaOH/HCl activated P. terebinthus L oily seeds based activated carbon (acid/base-treated activated carbon) [125], and KOH/HCl activated CCAC (acid/base-treated activated carbon) (Fig. 10 (c)) [139] followed the chemical sorption as indicated by their higher R^2 values of pseudo-second order kinetic model except for Juniperus procera Leaves-H_2SO_4 acid AC (acid-treated activated carbon) (Fig. 9 (a)) [107] and Phosphoric acid-treated tamarind hull activated carbon (acid-treated activated carbon) (Fig. 9 (b)) [131]. Thus, it can be concluded that pseudo-second-order kinetics modeling of biomass-derived activated carbon adsorbents better described the experimental values than the pseudo-first-order kinetic model except for the Juniperus procera Leaves-H_2SO_4 acid AC
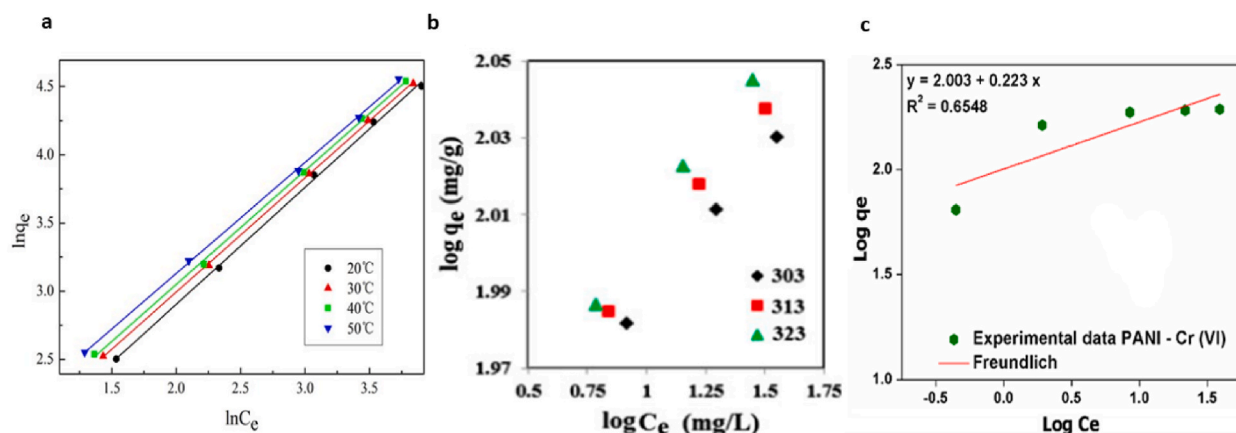

Fig. 16. Freundlich Isotherm of PANI polymer adsorbents for Cr(VI) adsorption **(a)** (PANI/EVOH) nanofiber composite membranes [188], **(b)** PANI/PVA [192], and **(c)** PANI/ γ-Fe_2O_3 [154].

Table 9

Pseudo-first-order and pseudo-second-order kinetic model constants obtained for Cr(VI) heavy metal adsorption by PANI polymer composites as adsorbents.

Adsorbent type	Adsorbent	Initial Cr(VI) Conc. (mg/l)	T/ K	pH	Dose (g/ L)	$q_{e,exp}$ (mg/ g)	Pseudo-first order kinetic model			Pseudo-second order kinetic model			Kinetic model	Ref
							$q^I_{e,cal}$ (mg/ g)	k_1 (1/min)	R^2	$q^{II}_{e,cal}$ (mg/ g)	k_2 (g/mg. min)	R^2		
PANI polymer composite	(PANI/PI) microfiber membranes	20	298	1	0.4	48.9	41.89	0.018447	0.96894	52.74	0.0007	0.99826	PSO	[185]
	PPy-PANI/Fe$_3$O$_4$	50	298	2	1	–	7	0.0147	0.8551	49.75124	0.01	1	PSO	[186]
		75	298	2	1	–	22.99	0.0175	0.9573	75.18797	0.003109	0.9999	PSO	[186]
		100	298	2	1	–	46.04	0.0168	0.9667	100	0.001395	0.9997	PSO	[186]
		100	288	2	1	–	–	–	–	97.66	0.000594	0.9974	PSO	[186]
		100	298	2	1	–	–	–	–	100.30	0.001386	0.9997	PSO	[186]
		100	308	2	1	–	–	–	–	100.60	0.002023	0.9999	PSO	[186]
		100	318	2	1	–	–	–	–	100.30	0.004168	0.9999	PSO	[186]
	PANI nanosheets	20	298	2	0.5	100	24.08	0.00898	0.9903	102.1	0.000795	0.9997	PSO	[187]
	PANI nanotubes	20	298	2	0.5	100	17.38	0.0414	0.9822	101.4	0.00546	0.9998	PSO	[187]
	PANI nanofibers	20	298	2	0.5	100	10.86	0.0966	0.9986	101	0.0187	0.9999	PSO	[187]
	(PANI/EVOH) nanofiber composite membranes	25	303	2	–	12.35	10.15	0.0578	0.98526	12.66	0.01543	0.99926	PSO	[188]
		50	303	2	–	24.49	7.02	0.0203	0.84955	24.98	0.0077169	0.99991	PSO	[188]
		100	303	2	–	47.97	10.61	0.64	0.81523	48.78	0.003963	0.99988	PSO	[188]
		150	303	2	–	70.94	30.29	0.0243	0.97882	73.10	0.001816	0.99984	PSO	[188]
		200	303	2	–	93.09	41.31	0.0288	0.98084	95.97	0.001485	0.99969	PSO	[188]
	PANI/LDHs (LDHs/aniline mass ratio of 1:8)	40	288	3	0.2	–	110.39	0.66	0.938	182.48	0.024	0.999	PSO	[190]
	PANI/H-TNB (H-TNBs/aniline mol ratio of 1: 20)	20	298	5	0.3	56.13	60.26	0.262	0.915	58.65	0.0017	0.999	PSO	[191]
	PANI/PVA composite	200	303	4	2	–	–	0.086	0.870	109.17	0.0009	0.998	PSO	[192]
		225	303	4	2	–	–	0.076	0.892	116.95	0.0008	0.998	PSO	[192]
		250	303	4	2	–	–	0.065	0.994	120.33	0.001	0.999	PSO	[192]
		200	313	4	2	–	–	0.143	0.803	109.76	0.0009	0.999	PSO	[192]
		225	313	4	2	–	–	0.142	0.799	118.34	0.0008	0.999	PSO	[192]
		250	313	4	2	–	–	0.064	0.964	121.80	0.0009	0.999	PSO	[192]
		200	323	4	2	–	–	0.096	0.949	110.37	0.001	0.999	PSO	[192]
		225	323	4	2	–	–	0.082	0.962	119.61	0.001	0.999	PSO	[192]
		250	323	4	2	–	–	0.053	0.984	122.85	0.001	0.998	PSO	[192]
	SA-PANI	100	303	4.2	2	–	–	0.0649	0.979	48.169	0.001104	0.999	PSO	[193]
		150	303	4.2	2	–	–	0.0554	0.982	54.854	0.001855	0.999	PSO	[193]
		200	303	4.2	2	–	–	0.0624	0.955	66.269	0.001529	0.999	PSO	[193]
	PANI/γ-Fe$_2$O$_3$	50	RT	2	0.2	195.7	183.2	0.095	0.56	215.5	0.0007.5	0.99	PSO	[154]
	PANI-MWCNT	20	288	4.5	0.5	24.24	08.80	0.00415	0.874	19.19	0.00260	0.996	PSO	[194]
		40	298	4.5	0.5	27.25	10.61	0.00392	0.938	23.20	0.00167	0.995	PSO	[194]
		80	308	4.5	0.5	33.39	10.49	0.00345	0.941	27.25	0.00189	0.994	PSO	[194]
	PANI/PA composite	2.5	298	5.5	0.5	4.94	0.74	0.00495	0.852	4.94	0.31	0.999	PSO	[195]
		5	298	5.5	0.5	9.76	5.06	0.00829	0.974	9.83	0.00573	0.999	PSO	[195]
		10	298	5.5	0.5	12.34	5.65	0.00553	0.975	12.61	0.00527	0.998	PSO	[195]
		30	298	5.5	0.5	14.37	15.60	0.00714	0.979	14.62	0.00388	0.998	PSO	[195]

PANi/SD/PEG=Poly, aniline/polyethylene glycol, coated on sawdust; RT = Room Temperature; (PANI/PI) microfiber membranes = Dodecylbenzene sulfonic acid (DBSA) doped-polyaniline; (PANI) coated conductive polyimide (PI) microfiber membrane; PPy-PANI/Fe$_3$O$_4$ = Polypyrrole- Polyaniline/magnetic nanocomposite; PANI nanosheets = Polyaniline nanosheets; [a] The RL values with the initial Cr(VI) concentration (C0) of 30–60nullmg/l; PANI nanotubes = Polyaniline nanotubes; PANI nanofibers = Polyaniline nanofibers; (PANI/EVOH) nanofiber composite membranes= (polyaniline/ethylene vinyl alcohol) nanofiber composite membranes; PANI=Polyaniline; PANI@MoS$_2$=Polyaniline-Molybdenum disulfide; PANI/LDHs = Polyaniline/Layered Double Hydroxides; PANI/H-TNB = polyaniline/hydrogen-titanate nanobelt nanocomposite; PANI/PVA composite = polyaniline/Poly(vinyl acetate) composite; SA-PANI= Sodium alginate-polyaniline nanofibers; PANI/ γ -Fe$_2$O$_3$ = polyaniline/ maghemite nanocomposite; PANI-MWCNT = polyaniline-multiwalled carbon nanotubes; PANI/PA composite = polyaniline/palygorskite composites; PFO= Pseudo-first-order kinetic model; PSO= Pseudo-second-order kinetic model.

(acid-treated activated carbon) and Phosphoric acid-treated tamarind hull activated carbon (acid-treated activated carbon) which followed the pseudo-first-order kinetic model due to its higher R^2 value as compared to R^2 value of pseudo-second-order kinetics model [107].

4.3. Nanocomposite adsorbents

Nanocomposite-based adsorbents are gaining the attention of researchers as they offer better adsorption by coupling particles with other adsorbents [129,140]. Examples of nanocomposite-based adsorbents include Chitosan-g-poly(butylacrylate)/silica gel (Cs-g-PBA/SG) nanocomposite [141], Chitosan-magnetite (Chitosan-Fe$_3$O$_4$) nanocomposite strip [142], Magnetite/bacterial cellulose (Fe$_3$O$_4$/BC) nanocomposites [143], and Zero-valent copper-chitosan (Ch-(Cu^0)) nanocomposites [144]. Polyaniline-modified adsorbents are commonly used for heavy metal removal due to their excellent biodegradability, biocompatibility [145–148], non-toxicity [145–149], electrical conductivity, electrical/optical capabilities, ion exchange properties, environmental stability, simple and low-cost production, a strong affinity for metal ions, and effectiveness in reducing harmful contaminants are all advantages [149].

The Langmuir adsorption isotherm constants obtained for Cr(VI) heavy metal adsorption by using nanocomposites as adsorbents are listed in Table 6.

4.3.1. Nanocomposite adsorbents and Langmuir adsorption isotherm

The maximum adsorption capacity is dependent on the element-modified nanocomposite adsorbents. Several nanocomposite adsorbents have been used: Fe-based, Mn-based, Cu-based, and graphene-based. The Langmuir adsorption isotherms of the nanocomposite adsorbents are evaluated based on the maximum adsorption capacity, Langmuir constant (K_L), and R^2 value. The best maximum adsorption capacity of nanocomposite adsorbents is exhibited by the MGO-Trp nanocomposite (graphene-based nanocomposite) while representing the mono-layer adsorption shown by the R^2 value approaching unity [170]. It is evident from the literature cited in Table 6 that all nanocomposite adsorbents followed the monolayer adsorption. Hence, it can be stated that the maximum adsorption capacity depends on the modification of the graphene nanocomposite adsorbents.

However, nZVI–Fe$_3$O$_4$ (Fe-based nanocomposite adsorbent) resulted in the highest Langmuir constant (K_L) value indicating the strongest interaction between Cr(VI) and nZVI–Fe$_3$O$_4$ (Fe-based nanocomposite adsorbent) [171] among other nanocomposite adsorbents. Therefore, graphene-based nanocomposite adsorbents result in the best results of Langmuir adsorption isotherms for Cr(VI) adsorption with the highest maximum adsorption capacity and K_L value greater than unity the strongest interaction between Cr(VI) and graphene-based nanocomposite adsorbents while following monolayer adsorption. Various nanocomposite adsorbents were used to absorb Cr(VI). The Langmuir adsorption isotherms for Cr(VI) adsorption by using nanocomposite as adsorbents are presented in Fig. 11.

The maximum adsorption capacity, Langmuir constant (K_L) and R^2 depend on the elements-modified nanocomposite adsorbent used, such as (Fe-based nanocomposite, Mn Cu-based nanocomposite, and graphene-based nanocomposite). The IO@CaCO$_3$ (Fe-based nanocomposite) resulted in the best Langmuir adsorption isotherms for Cr(VI) adsorption as represented by its highest maximum adsorption capacity and R^2 value approaching unity indicating the well-fitting of the Langmuir adsorption isotherm with the experimental adsorption capacity as shown in Fig. 11 (a) [173] among other Fe-based nanocomposite adsorbents cited in Table 6 such as Chi@Fe$_3$O$_4$ nanocomposite [174], Peganum harmala seed-based GnZVI/PAC [175], nZVI–Fe$_3$O$_4$ nanocomposites [171], and PPY/γ-Fe$_2$O$_3$ nanocomposite [176]. Furthermore, it can be interpreted from the R^2 value approaching unity that the IO@CaCO$_3$ (Fe-based nanocomposite) follows a mono-layer adsorption mechanism. However, the lower value of Langmuir constant (K_L) of IO@CaCO$_3$ (Fe-based nanocomposite) showed weaker interactions between Cr(VI) and IO@CaCO$_3$ (Fe-based nanocomposite) [173]. The higher Langmuir constant (K_L) values of nZVI–Fe$_3$O$_4$ (Fe-based nanocomposite) [171], peganum harmala seed-based GnZVI/PAC (Fe-based nanocomposite) [175], and PPY/ γ-Fe$_2$O$_3$ nanocomposite [176] showed stronger interactions between Cr(VI) and Fe-based nanocomposite adsorbents. Hence, zero-valent iron nanoparticles (nZVI) significantly enhance the Langmuir constant (K_L) values due to the strong interactions between Cr(VI) and the nZVI-based nanocomposite adsorbents.

However, the MnO$_2$/Fe$_3$O$_4$/o-MWCNTs (Mn-based nanocomposite) resulted in the best Langmuir adsorption isotherms for Cr(VI) adsorption as represented by its maximum adsorption capacity, R_L value between 0 and 1 indicating favorable Langmuir adsorption isotherm, and R^2 value approaching unity indicated that the Langmuir adsorption isotherm fits well with the experimental adsorption capacity value but with a lower K_L value [177] as compared to another Mn-based nanocomposite adsorbent such as MnF-MO-NPs (Mn-based nanocomposite adsorbent) [155]. Furthermore, it can be interpreted from the R^2 value approaching unity that the MnO$_2$/Fe$_3$O$_4$/o-MWCNTs (Mn-based nanocomposite adsorbent) follow the mono-layer adsorption mechanism. The Langmuir constant (K_L), smaller than unity and closely approaching zero, indicates one of the weakest interactions between Cr(VI) and MnO$_2$/-Fe$_3$O$_4$/o-MWCNTs (Mn-based nanocomposite adsorbent) [177]. It can be interpreted that the Mn-based nanocomposite adsorbents follow the monolayer adsorption mechanism; however, observing weaker interactions between Cr(VI) and MnO$_2$/Fe$_3$O$_4$/o-MWCNTs (Mn-based nanocomposite adsorbent) due too-MWCNTs. Moreover, MnF-MO-NPs (Mn-based nanocomposite adsorbent) showed a stronger interaction between Cr(VI) and MnF-MO-NPs (Mn-based nanocomposite adsorbent) due to K_L value greater than one [155]. The Mn-based nanocomposite adsorbents follow a favorable Langmuir adsorption isotherm as the R_L value is between 0 and 1, as shown in Table 6.

The CuO (Cu-based nanocomposite adsorbent) resulted in good Langmuir adsorption isotherms for Cr(VI) adsorption as represented by its maximum adsorption capacity, R_L value between 0 and 1, indicating favorable Langmuir adsorption isotherm, and R^2 value approaching unity indicates the well-fitting of Langmuir adsorption isotherm with the experimental adsorption capacity value as shown in Fig. 11 (b) [158]. Furthermore, it can be interpreted from the R^2 value approaching unity that the CuO (Cu-based

nanocomposite adsorbent) follows a mono-layer adsorption mechanism. The Langmuir constant (K_L), more significant than unity, indicates a stronger interaction between Cr(VI) and CuO (Cu-based nanocomposite adsorbent) at a higher temperature [158]. It has been interpreted that the Cu-based nanocomposite adsorbents result in a lower maximum adsorption capacity while following the monolayer adsorption mechanism, observing stronger interactions between Cr(VI) and Cu-based nanocomposite adsorbents at elevated temperature and favorable Langmuir adsorption isotherm.

The MGO-Trp nanocomposite (graphene-based nanocomposite adsorbent) resulted in the best Langmuir adsorption isotherms for Cr(VI) adsorption as represented by its highest maximum adsorption capacity, R_L value between 0 and 1, indicating favorable Langmuir adsorption isotherm, and R^2 value approaching unity indicates the well-fitting of Langmuir adsorption isotherm with the experimental adsorption capacity value [161] but with a lower Langmuir constant (K_L) value showing the weakest interaction between Cr(VI) and MGO-Trp nanocomposite (graphene-based nanocomposite adsorbent) as shown in Fig. 11 (c) than other graphene-based nanocomposite adsorbents such as pssN-GO, psN-GO, pN-GO [159], mimGO sponge, GO sponge, EDA-GO sponge [178], rGO/PEI-KOH nanocomposite [179], GO [162], n-GO@HTCS biocomposite [163], CS-GO [164], GFM [165], Chi@Fe_3O_4GO nanocomposite [174], Fe_3O_4/G [166], Chitosan/CDTA/GO [167], GO-1N, GO-2N, GO-3N [168], and RGO/NiO [169]. Furthermore, it can be interpreted from the R^2 value approaching unity that MGO-Trp nanocomposite (graphene-based nanocomposite adsorbent) follows a mono-layer adsorption mechanism. Again, the worst maximum adsorption capacity is shown by the GO-1N following mono-layer adsorption as the R^2 value approaches unity, but a stronger interaction between Cr(VI) and GO-1N (graphene-based nanocomposite adsorbent) [168].

However, GO sponge (graphene-based nanocomposite adsorbent) resulted in the highest Langmuir constant (K_L) value indicating the strongest interaction between Cr(VI) and GO sponge (graphene-based nanocomposite adsorbent) [178] among other graphene-based nanocomposite adsorbents. It has been interpreted that the graphene-based nanocomposite adsorbents result in the highest maximum adsorption capacity while following the monolayer adsorption mechanism and favorable Langmuir adsorption isotherm. However, interactions between Cr(VI) and graphene-based nanocomposite adsorbent depend on the compound/component attached to the graphene-based nanocomposite.

It can be concluded that the best Langmuir adsorption isotherm results for Cr(VI) adsorption are represented by MGO-Trp nanocomposite (graphene-based nanocomposite adsorbent) as indicated by its highest maximum adsorption capacity and R^2 value but with a lower K_L value representing weaker interactions between Cr(VI) and adsorbent. However, the best interaction between Cr(VI) and graphene-based nanocomposite adsorbent is shown by nZVI–Fe_3O_4 nanocomposites (Fe-based nanocomposite adsorbent) as represented by the highest Langmuir constant (K_L) > 1.

4.3.2. Nanocomposite adsorbents and Freundlich adsorption isotherm

The adsorption capacity on heterogenous sites of an adsorbent (K_F) depends on the type of nanocomposite adsorbents used, such as (Fe-based nanocomposite, Mn-based nanocomposite, Cu-based nanocomposite, and graphene-based nanocomposite). The Freundlich adsorption isotherms for Cr(VI) adsorption using nanocomposite adsorbents are presented in Fig. 12. However, the Freundlich adsorption isotherm constants obtained for Cr(VI) heavy metal adsorption by using these nanocomposite adsorbents are listed in Table 6.

It can be observed from Table 6 that the IO@$CaCO_3$ (Fe-based nanocomposite) resulted in the highest value of K_F for Cr(VI) adsorption. However, the value of R^2 for Cr(VI) adsorption using this type of activated carbon through Freundlich adsorption isotherm (Fig. 12 (a)) is lower as compared to Langmuir adsorption isotherm [152]. However, the lowest value of K_F is shown by the MGO-Trp nanocomposite (Graphene-based nanocomposite) while following multi-layer adsorption on the heterogenous surface of MGO-Trp nanocomposite (Graphene-based nanocomposite) (Fig. 12 (b)) [161] among other nanocomposite adsorbents.
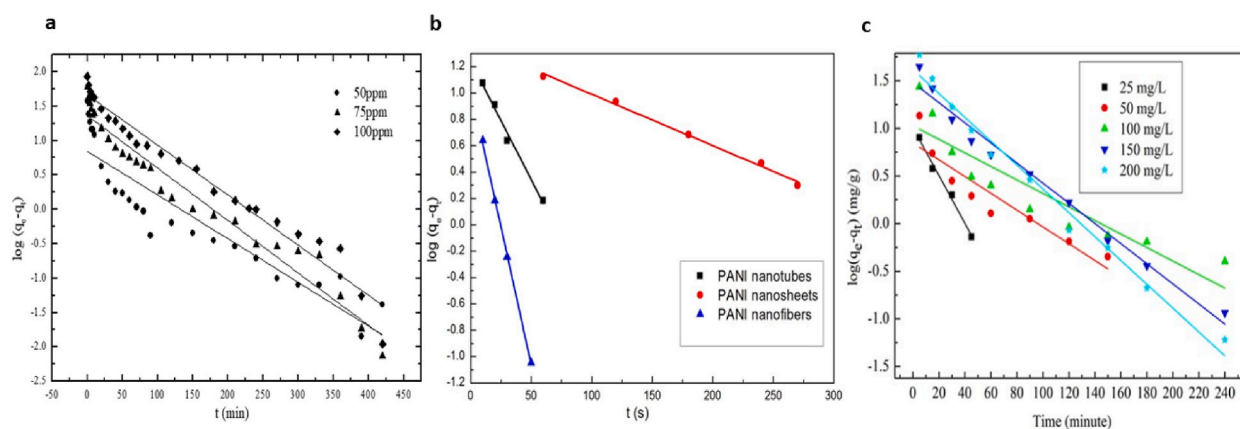

Fig. 17. Pseudo-first-order kinetic model of PANI polymer adsorbents for Cr(VI) adsorption **(a)** PPy-PANI/Fe_3O_4 at different Cr(VI) concentrations [186], **(b)** PANI nanosheets, PANI nanotubes, and PANI nanofibers [187], and **(c)** (PANI/EVOH) nanofiber composite membranes [188].
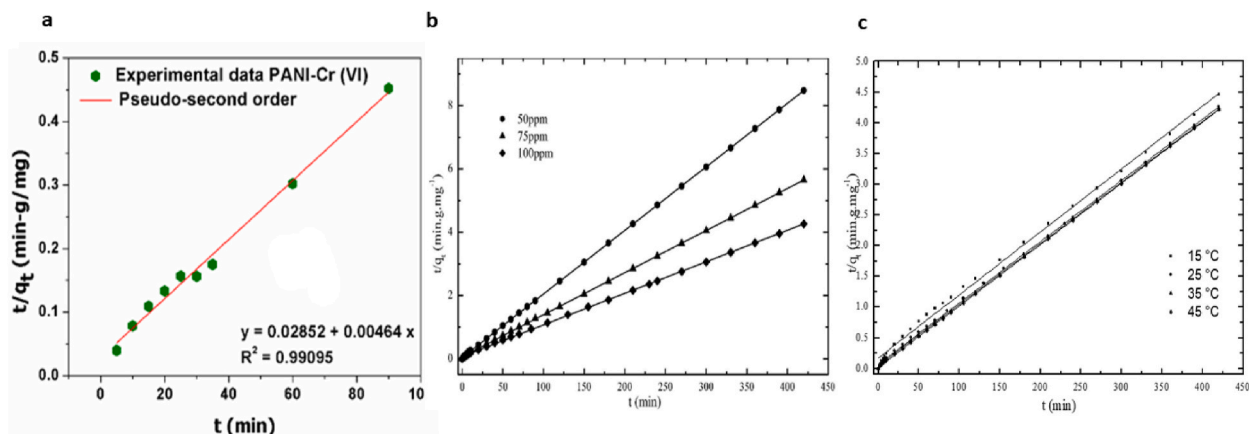
Fig. 18. Pseudo-second-order kinetic model of PANI polymer adsorbents for Cr(VI) adsorption **(a)** PANI/γ-Fe$_2$O$_3$ [154], **(b)** PPy-PANI/Fe$_3$O$_4$ at different concentrations [186], and **(c)** PPy-PANI/Fe$_3$O$_4$ at different Cr(VI) temperatures [186].
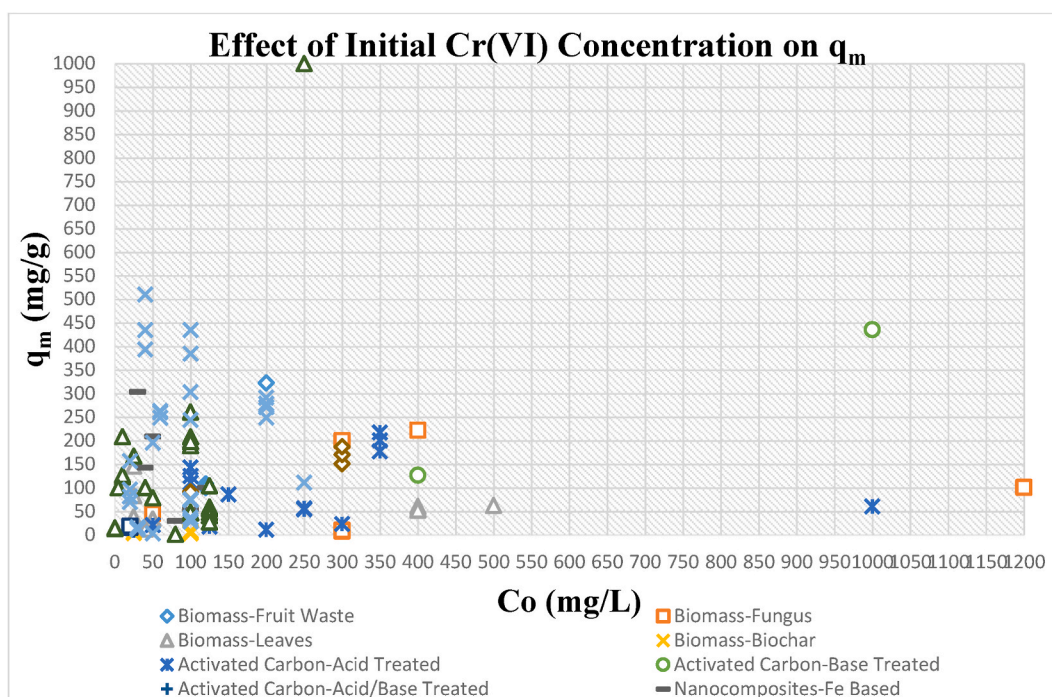

Fig. 19. Effect of initial Cr(VI) concentration (C$_o$) on the Langmuir's maximum adsorption capacity (q$_m$).

The highest adsorption intensity is observed by IO@CaCO$_3$ (Fe-based nanocomposite) and GO (Graphene-based nanocomposite) following mono-layer adsorption [162]. Furthermore, it can be interpreted from the adsorption intensity (n) of the nanocomposite adsorbents that the adsorption of Cr(VI) is mainly a chemical process.

Furthermore, the removal of 2-aminoethyl from the pssN-GO (Graphene-based nanocomposite) leads to the dominance of multi-layer adsorption with a decline in Freundlich constant (K$_F$) and adsorption intensity (n), which is quite evident in psN-GO (Graphene-based nanocomposite) and pN-GO (Graphene-based nanocomposite) [159]. MnF-MO-NPs (Mn-based nanocomposite) resulted in good values of Freundlich constant and adsorption intensity while following mono-layer adsorption, as shown in Fig. 12 (c) [155].

Moreover, Fe-based nanocomposites (Chi@Fe$_3$O$_4$ nanocomposite [150], and nZVI–Fe$_3$O$_4$ nanocomposites [153]), and Graphene-based nanocomposite (psN-GO [159], pN-GO [159], and MGO-Trp nanocomposite [161]), followed the multi-layer adsorption of Cr(VI) on the heterogenous surface of these activated carbon adsorbents due to their higher R^2 values of Freundlich adsorption isotherms than Langmuir adsorption isotherms. In contrast, Freundlich adsorption isotherm modelling of Fe-based nanocomposites (Peganum harmala seed-based GnZVI/PAC [151], IO@CaCO$_3$ [152], PPY/ γ-Fe$_2$O$_3$ [154]), Mn-based nano-composites (MnF-MO-NPs [155], MnO$_2$/Fe$_3$O$_4$/o-MWCNTs [156]**)**, Cu-based nanocomposite (CuO [158]), and Graphene-based
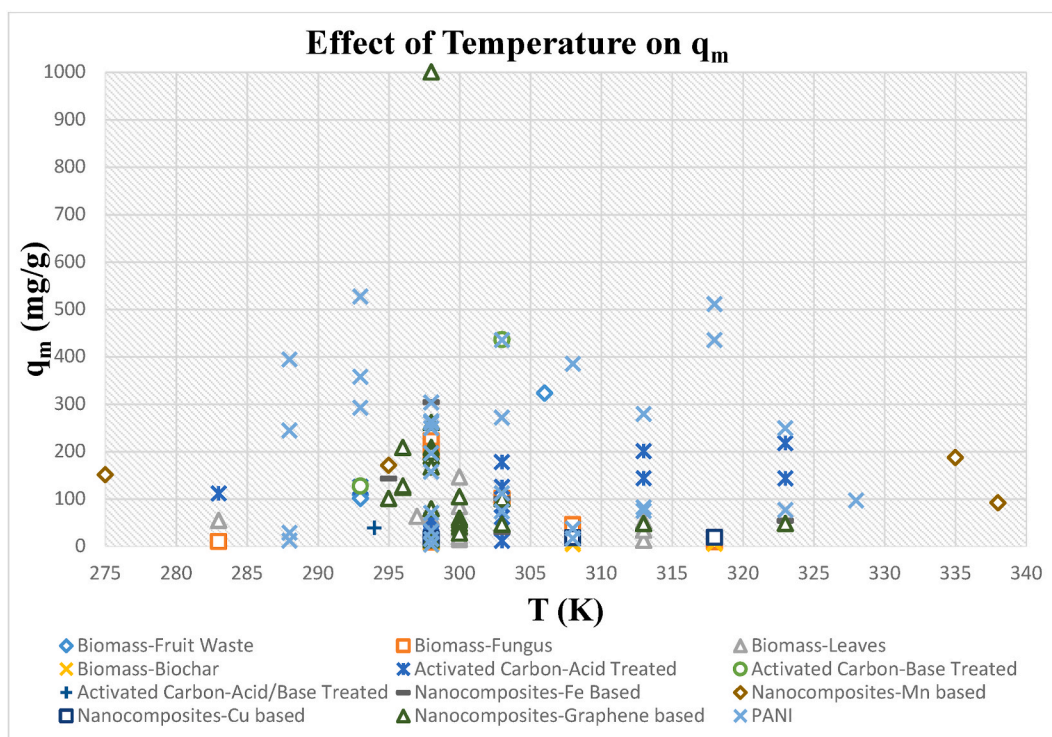
Fig. 20. Effect of temperature (T) on the Langmuir's maximum adsorption capacity (q_m).

nanocomposite (pssN-GO [159], mimGO sponge [160], GO sponge [160], EDA-GO sponge [160], GO [162], n-GO@HTCS bio-composite [163], GFM [165], Chi@Fe$_3$O$_4$GO nanocomposite [150], Fe$_3$O$_4$/G [166], Chitosan/CDTA/GO [167], GO-1N, GO-2N, GO-3N [168], and RGO/NiO) [169] followed the mono-layer adsorption as their adsorption data fitted well with a Langmuir adsorption isotherm model rather than Freundlich adsorption isotherm model.

However, CS-GO (Graphene-based nanocomposite) followed the Langmuir adsorption isotherm at adsorbent dosages of 0.25, 0.5, 0.75, 2, and 3 g L^{-1}, while Freundlich adsorption isotherm at an adsorbent dosage of 1 g L^{-1} [164].

4.3.3. Nanocomposite adsorbents and pseudo-first order and pseudo-second order kinetic models

The experimental amount of adsorbate adsorbed at equilibrium ($q_{e,exp}$) depends on the type of nanocomposite adsorbent used, such as Fe-based nanocomposite, Mn-based nanocomposite, Cu-based nanocomposite, and graphene-based nanocomposite for Cr(VI) adsorption. The pseudo-first-order (PFO) and pseudo-second-order (PSO) kinetic models of nanocomposite adsorbents for Cr(VI) adsorption were evaluated using the experimental and calculated amounts of Cr(VI) adsorbed at equilibrium ($q_{e,exp}$, $q_{e,cal}^{I}$, $q_{e,cal}^{II}$), as well as the pseudo-first-order rate constant (k_1), pseudo-second-order rate constant (k_2) and R^2 value. Table 7 lists the experimental and calculated amounts of Cr(VI) adsorbed at equilibrium, pseudo-first-order and pseudo-second-order rate constants, and R^2 values obtained for various nanocomposite adsorbents for Cr(VI) adsorption.

The linear pseudo-first-order kinetic and pseudo-second-order kinetic models of nanocomposite adsorbents for Cr(VI) adsorption are shown in Figs. 13 and 14, respectively.

The MGO-Trp nanocomposite (Graphene-based nanocomposite) exhibited the highest experimental and calculated amounts of Cr(VI) adsorbed at equilibrium ($q_{e,exp}$, $q_{e,cal}^{I}$, and $q_{e,cal}^{II}$) among all types of nanocomposite adsorbents, with the highest R^2 value of the pseudo-second-order kinetic model as shown in Fig. 13 (a) indicating chemical sorption involving valence forces through sharing or exchange of electrons between the graphene-based nanocomposite and Cr(VI) as compared to pseudo-first-order kinetic model as shown in Fig. 13 (a) [161]. In contrast, the GO (Graphene-based nanocomposite) achieved the lowest calculated amount of Cr(VI) adsorbed at equilibrium ($q_{e,cal}^{II}$) by pseudo-second-order kinetic model among all types of nanocomposite adsorbents and indicated that the adsorption of Cr(VI) using GO is not a chemisorption process and hence validated the pseudo-first-order kinetic model [162].

The IO@CaCO$_3$ (Fe-based nanocomposite) showed the highest calculated amounts of Cr(VI) adsorbed at equilibrium ($q_{e,cal}^{I}$, and $q_{e,cal}^{II}$) among other Fe-based nanocomposite adsorbents, with the highest R^2 value of the pseudo-second-order kinetic model (Fig. 14 (b)) than pseudo-first-order kinetic model (Fig. 13 (b)) [152].

The MnO$_2$/Fe$_3$O$_4$/o-MWCNTs (Mn-based nanocomposite) showed the highest experimental and calculated amounts of Cr(VI) adsorbed at equilibrium by the pseudo-second-order kinetic model ($q_{e,exp}$, and $q_{e,cal}^{II}$) among other Mn-based nanocomposite adsorbents, with the highest R^2 value of the pseudo-second-order kinetic model (Fig. 14 (c)) than pseudo-first-order kinetic model (Fig. 13 (c)) [156].
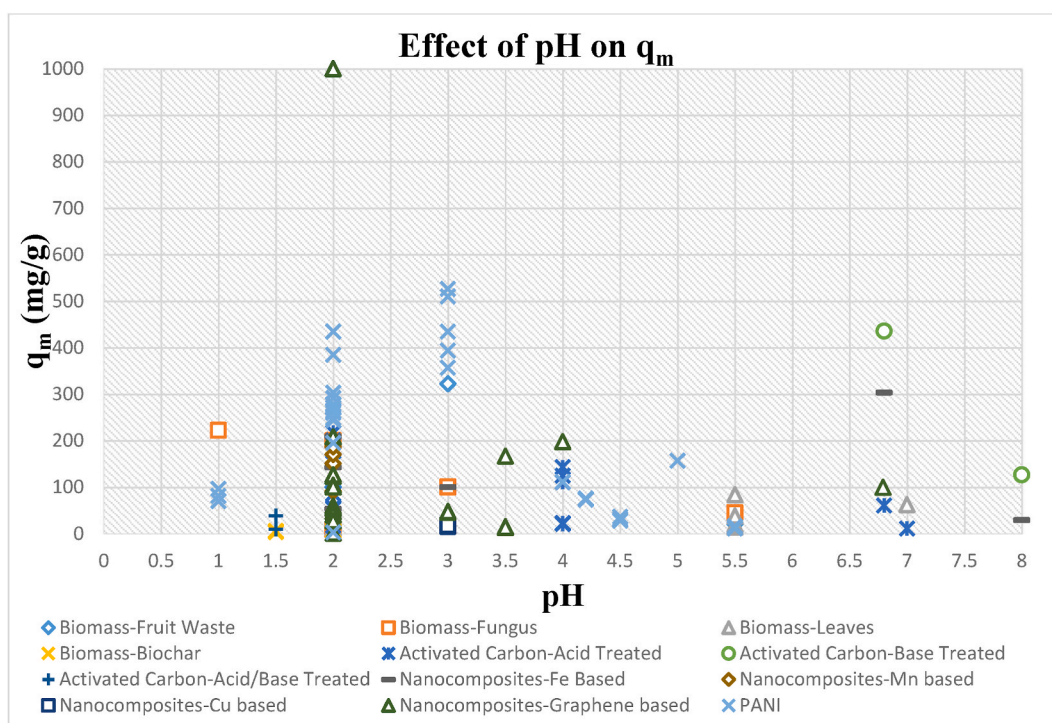
Fig. 21. Effect of pH on the Langmuir's Maximum Adsorption Capacity (q_m).

The GFM (Graphene-based nanocomposite) showed the lowest experimental amount of Cr(VI) adsorbed at equilibrium ($q_{e,exp}$), which best fits with the calculated amount of Cr(VI) adsorbed at equilibrium ($q_{e,cal}^I$) by pseudo-first-order kinetic model and indicated that the adsorption of Cr(VI) follows pseudo-first-order kinetic model [165].

Furthermore, it was also observed that the increase in initial Cr(VI) concentration significantly enhances the amount of qe. Most nanocomposite adsorbents, including Fe-based nanocomposites (Peganum harmala seed-based GnZVI/PAC [151], Chi@Fe$_3$O$_4$ nanocomposite [150], IO@CaCO$_3$ [152], nZVI–Fe$_3$O$_4$ nanocomposites [153], and PPY/ γ-Fe$_2$O$_3$ [154]), Mn-based nanocomposites (MnF-MO-NPs [155], MnO$_2$/Fe$_3$O$_4$/o-MWCNTs [156]), Cu-based nanocomposite (CuO [158]), and Graphene-based nanocomposite (pssN-GO [159], psN-GO [159], pN-GO [159], mimGO sponge [160], GO sponge [160], EDA-GO sponge [160], MGO-Trp nano-composite [161], n-GO@HTCS biocomposite [163], CS-GO [164], Fe$_3$O$_4$/G [166], Chitosan/CDTA/GO [167], GO-1N, GO-2N, GO-3N [168], and RGO/NiO [169]) followed the chemical sorption as indicated by their higher R^2 values of the pseudo-second-order kinetic model except for the few Graphene-based nanocomposites (GO [162], and GFM [165]). Thus, it can be concluded that the pseudo-second-order kinetics modeling of nanocomposite adsorbents better described the experimental values than pseudo-first-order kinetic model except for the for few Graphene-based nanocomposites (GO [162], and GFM [165]) which followed the pseudo-first order kinetic model due to its higher R^2 value as compared to R^2 value of pseudo-second-order kinetics model.

4.4. PANI polymer composite adsorbents

Several studies have recommended PANI-based biosorbents due to their broad spectrum of efficacy. Adsorbents based on Fe$_3$O$_4$/G/ PANI can be utilized to remove heavy metal ions effectively. PANI is employed in many applications, such as catalysts, energy storage, corrosion inhibitors, chemical and biological sensors, and selective ion-transport switchable membranes [149,180–184].

The Langmuir adsorption isotherm constants obtained for Cr(VI) heavy metal adsorption by using PANI polymer composites as adsorbents are listed in Table 8.

4.4.1. PANI polymer composite adsorbents and Langmuir adsorption isotherm

The maximum adsorption capacity is dependent on the type of compound/element attached to the PANI-based adsorbents. Several PANI-based adsorbents have been used for Cr(VI) adsorption. The Langmuir adsorption isotherms of the PANI-based adsorbents are evaluated based on the maximum adsorption capacity, Langmuir constant (K_L), and R^2 value. The best maximum adsorption capacity of PANI-based adsorbents is exhibited by the PANI@MoS$_2$ (PANI-based adsorbent) while representing the mono-layer adsorption as shown by the R^2 value approaching unity [189] but with a K_L value approximately equals to 1 indicating a stable interaction between Cr(VI) and PANI@MoS$_2$ (PANI-based adsorbent). It is evident from the literature cited in Table 8 that almost all PANI-based adsorbents followed mono-layer adsorption. However, the PANi/SD/PEG shows the worst maximum adsorption capacities following the

mono-layer adsorption mechanisms [172]. Hence, it can be stated that the maximum adsorption capacity depends on the compound attached to the PANI-based adsorbents. However, PANI/PA composite (PANI-based adsorbent) resulted in the highest Langmuir constant (K_L), indicating a stronger interaction between Cr(VI) and PANI/PA composite (PANI-based adsorbent) value at a lower temperature [195] among other PANI-based adsorbents. Therefore, PANI@MoS$_2$ (PANI-based adsorbent) results in the best results of Langmuir adsorption isotherms for Cr(VI) adsorption but has a drawback of showing stable interactions between Cr(VI) and PAN-I@MoS$_2$ (PANI-based adsorbent) [189]. Various PANI-based adsorbents were used to adsorb Cr(VI). The Langmuir adsorption isotherms for Cr(VI) adsorption by using PANI as adsorbents are presented in Fig. 15.

The maximum adsorption capacity, Langmuir constant (K_L) and R^2 depend on the type of compound/element attached to the PANI-based adsorbents. The PANI@MoS$_2$ (PANI-based adsorbent) resulted in the best Langmuir adsorption isotherms for Cr(VI) adsorption as represented by its highest maximum adsorption capacity and R^2 value approaching unity indicating the well-fitting of the Langmuir adsorption isotherm with the experimental adsorption capacity as shown in Fig. 15 (a) [189] among other PANI-based adsorbents cited in Table 8 such as PANi/SD/PEG [172], (PANI/PI) microfiber membranes [185], PPy-PANI/Fe$_3$O$_4$ [186], PANI nanosheets, PANI nanotubes, PANI nanofibers [187], (PANI/EVOH) nanofiber composite membranes [188], PANI [189], PANI/LDHs (LDHs/aniline mass ratio of 1:8) [190], PANI/H-TNB (H-TNBs/aniline mol ratio of 1: 20) [191], PANI/PVA composite [192], SA-PANI [193], PANI/γ-Fe$_2$O$_3$, PANI-MWCNT [194], and PANI/PA composite [195] for Cr(VI) adsorption. Furthermore, it can be interpreted from the R^2 value approaching unity that the PANI@MoS$_2$ (PANI-based adsorbent) follows a mono-layer adsorption mechanism. However, the value of the Langmuir constant (K_L) of PANI@MoS$_2$ (PANI-based adsorbent) showed stable interactions between Cr(VI) and PAN-I@MoS$_2$ (PANI-based adsorbent) [189]. The higher Langmuir constant (K_L) values of PANI/PA (polyaniline/palygorskite) composite [195] showed stronger interactions between Cr(VI) and PANI/PA composite (PANI-based adsorbent). Hence, palygorskite at a lower temperature significantly enhances the Langmuir constant (K_L) values due to the strong interactions between Cr(VI) and the PANI/PA composite adsorbent. In addition, the PANi/SD/PEG shows the worst maximum adsorption capacities following the mono-layer adsorption mechanisms and weaker interactions between Cr(VI) and PANi/SD/PEG adsorbent as shown by the lower K_L value [172]. Hence, it can be stated that the maximum adsorption capacity depends on the compound attached to the PANI-based adsorbents.

It can be concluded that the best Langmuir adsorption isotherm results for Cr(VI) adsorption are represented by PANI@MoS$_2$ (PANI-based adsorbent) as indicated by its highest maximum adsorption capacity and R^2 value but with a K_L value of approximately approaching unity representing stable interactions between Cr(VI) and adsorbent. Therefore, molybdenum disulfide-modified PANI adsorbent significantly helps achieve a high adsorption capacity. However, the best interaction between Cr(VI) and PANI-based is shown by PANI/PA composite (PANI-based adsorbent) as represented by the highest Langmuir constant (K_L) > 1.

4.4.2. PANI polymer composite adsorbents and Freundlich adsorption isotherm

The adsorption capacity on an adsorbent (KF) 's heterogenous sites depends on the type of compound/element attached to the
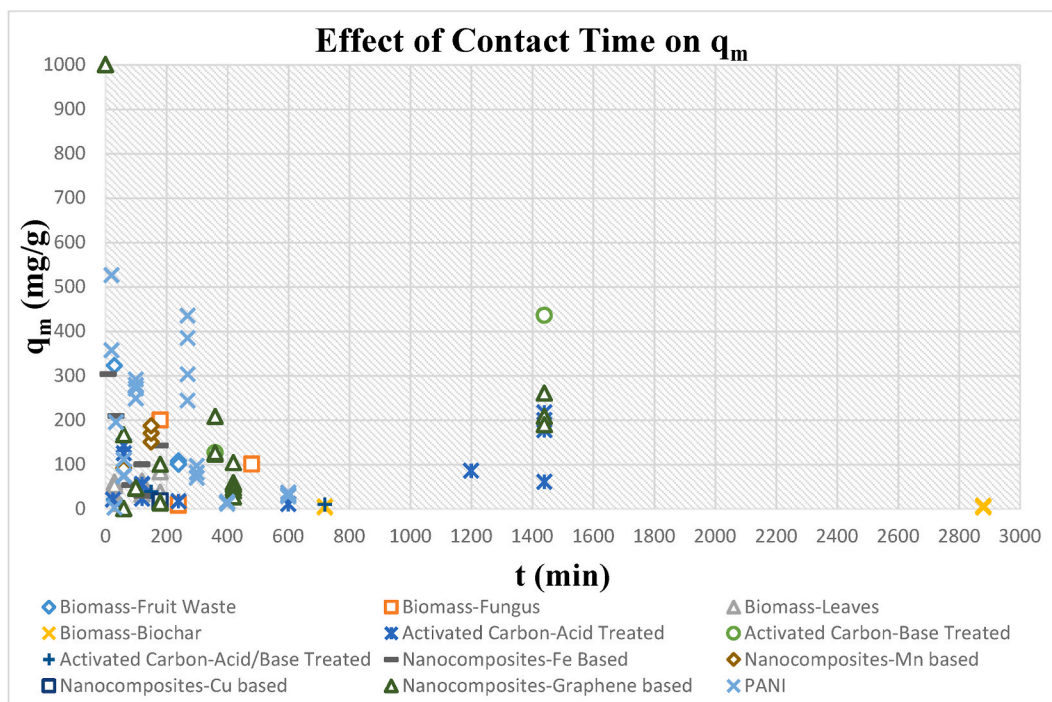

Fig. 22. Effect of contact time (t) on the Langmuir's maximum adsorption capacity (q_m).

PANI-based adsorbents. The Freundlich adsorption isotherms for Cr(VI) adsorption using PANI-based adsorbents are presented in Fig. 16. However, the Freundlich adsorption isotherm constants obtained for Cr(VI) heavy metal adsorption by using the PANI-based adsorbents are listed in Table 8.

It can be observed from Table 8 that the PANI/LDHs (LDHs/aniline mass ratio of 1:8) resulted in the highest value of K_F for Cr(VI) adsorption with the adsorption intensity less than 1 indicating the absorption of Cr(VI) using PANI/LDHs (LDHs/aniline mass ratio of 1:8) is a physical process. However, the value of R^2 for Cr(VI) adsorption using PANI/LDHs through Freundlich adsorption isotherm is lower as compared to Langmuir adsorption isotherm [190]. However, the lowest value of K_F is shown by the PANI/EVOH nanofiber composite membranes while following the chemical adsorption process and multi-layer adsorption on the heterogenous surface of PANI/EVOH nanofiber composite membranes (Fig. 16 (a)) [188] among other PANI-based adsorbents.

The highest adsorption intensity is observed by PANI/PVA composite while following mono-layer adsorption (Fig. 16 (b)) [192]. Furthermore, it can be interpreted from the adsorption intensity (n) of the PANI-based adsorbents that the adsorption of Cr(VI) adsorption is mainly a chemical process except for PANI [189], PANI@MoS$_2$ [189], PANI/LDHs (LDHs/aniline mass ratio of 1:8) [190], PANI/PVA composite [192] while following mono-layer adsorption.

Moreover, (PANI/EVOH) nanofiber composite membranes [188], SA-PANI [193], and PANI-MWCNT [194] followed the multi-layer adsorption of Cr(VI) on the heterogenous surface of these activated carbon adsorbents due to their higher R^2 values of Freundlich adsorption isotherms than Langmuir adsorption isotherms. In contrast, Freundlich adsorption isotherm modelling of PANi/SD/PEG [172], (PANI/PI) microfiber membranes [185], PPy-PANI/Fe$_3$O$_4$ [186], PANI nanosheets [187], PANI nanotubes [187], PANI nanofibers [187], (PANI/EVOH) nanofiber composite membranes [188], PANI [189], PANI@MoS$_2$ [189], PANI/LDHs (LDHs/aniline mass ratio of 1:8) [190], PANI/H-TNB (H-TNBs/aniline mol ratio of 1: 20) [191], PANI/PVA composite [192], PANI/ γ-Fe$_2$O$_3$ (Fig. 16 (c)) [154], and PANI/PA composite [195] followed the mono-layer adsorption as their adsorption data fitted well with a Langmuir adsorption isotherm model rather than Freundlich adsorption isotherm model.

It can be concluded that the best Freundlich isotherm results for Cr(VI) adsorption are represented by PANI/LDHs (PANI-based adsorbent) as indicated by its highest adsorption capacity on heterogenous sites and R^2 value greater than 0.9 but with a weak adsorption intensity value indicating adsorption of Cr(VI) a physical process. Therefore, Polyaniline/Layered Double Hydroxides significantly helps achieve a high adsorption capacity. However, the best interaction adsorption intensity is shown by PANI/PVA (polyaniline/Poly(vinyl acetate) composite) as represented by the highest adsorption intensity>1 indicating adsorption of Cr(VI) by using PANI-based adsorbent, a chemical process. However, the best-fit result of Freundlich adsorption isotherm is observed in (PANI/ EVOH) nanofiber composite membranes (polyaniline/ethylene vinyl alcohol) nanofiber composite membranes).

4.4.3. PANI polymer composite adsorbents and pseudo-first order and pseudo-second order kinetic models

The experimental amount of adsorbate adsorbed at equilibrium ($q_{e,exp}$) depends on the type of compound/element attached to the PANI-based adsorbents used for Cr(VI) adsorption. The pseudo-first-order (PFO) and pseudo-second-order (PSO) kinetic models of
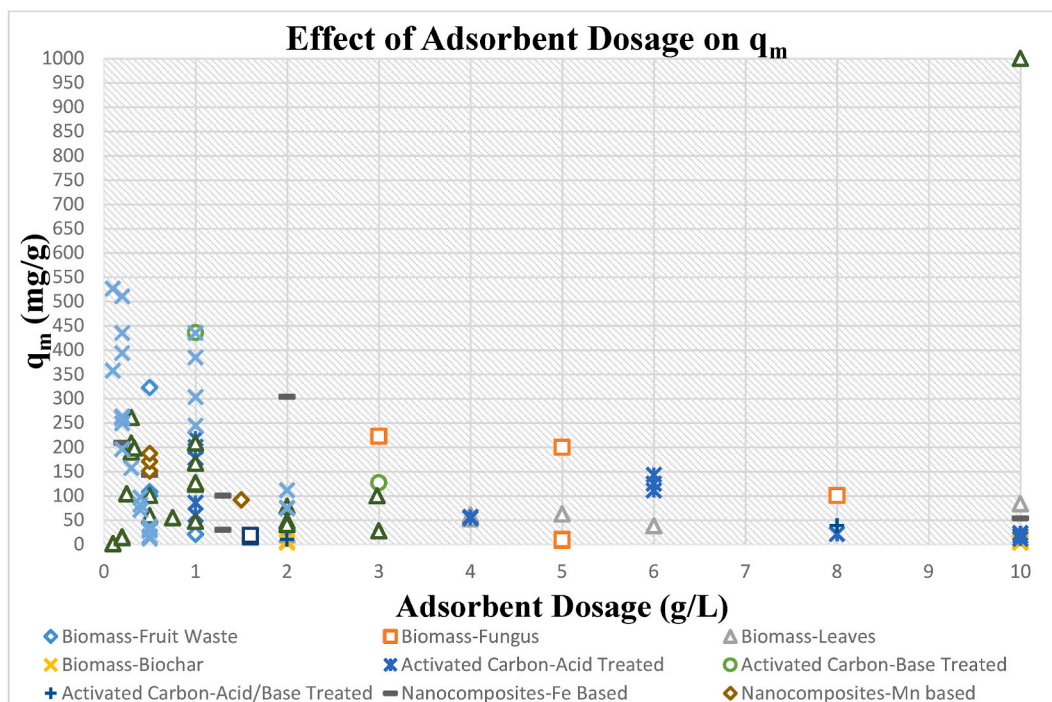

Fig. 23. Effect of adsorbent dosage on the Langmuir's maximum adsorption capacity (q_m).

Table 10
Langmuir and Freundlich adsorption isotherm constants obtained for Cr(VI) heavy metal adsorption by using adsorbents in industrial wastewater.

Source of wastewater	Adsorbent type	Adsorbent	Initial Cr(VI) Conc. (mg/l)	T/K	pH	Cont t (min)	Dose (g/L)	Exp. q_m (mg/g)	Langmuir				Freundlich			Isotherm model	Ref
									q_m (mg/g)	K_L (L/mg)	R^2	R_L	K_F	n	R^2		
Tannery wastewater	Biosorbent	Tea waste	455	303	3.9	240	6	–	90.90	0.265	0.9994	–	23.06	2.21	0.9669	L	[197]
		Syzygium cumini bark	2920.2 ± 0.7	293	3.9 ± 0.1	15	3[a']	–	500	−0.18182	0.847	–	0.05602	0.1224	0.995	F	[198]
		Corn cob	100	298	2	1440	0.1[a']	–	111.11	0.0052	0.969	–	1.640	1.5337	0.996	F	[199]
		Avocado kernel seeds (AKS)	4085	298	1	160	0.5[a'], 16.66	–	10.08	3.367	0.963	0.0059[b']	1.0162	1.724	0.998	F	[200]
		Juniperus procera sawdust (JPS)	4085	298	1	160	0.5[a'], 16.66	–	16.03	3.0303	0.968	0.0066[b']	1.2823	2.049	0.996	F	[200]
		Papaya peels (PP)	4085	298	1	160	0.5[a'], 16.66	–	7.16	3.861	0.966	0.0052[b']	0.8109	1.508	0.997	F	[200]
		Banana peel	0.1–100	293	2	60	10	–	131.5, 2.53 ± 0.15[c']	2.05 ± 0.14[d']	0.98	0.34–0.99	–	–	–	L	[201]
			0.1–100	298	2	60	10	–	1.85 ± 0.06[c']	2.87 ± 0.12[d']	0.99	0.27–0.99	–	–	–	L	[201]
			0.1–100	303	2	60	10	–	1.62 ± 0.07[c']	3.07 ± 0.02[d']	0.99	0.25–0.98	–	–	–	L	[201]
			0.1–100	308	2	60	10	–	1.52 ± 0.05[c']	3.06 ± 0.12[d']	0.99	0.25–0.99	–	–	–	L	[201]
			0.1–100	313	2	60	10	–	1.16 ± 0.04[c']	3.99 ± 0.16[d']	0.98	0.21–0.98	–	–	–	L	[201]
		Orange (Citrus cinensis) peel adsorbent	46.71	RT	2	90	2.5	–	5.0800	0.3469	0.730	–	3.6520	6.0800	0.08	L	[202]
		Coconut Coir pith	60	AT	7.33	60	40	1.2045*	–	–	–	–	158.8	1.8375	0.9988	F	[203]
		Banana waste (BW)	50	303	3	60	5	24.38	31.51	0.0301	0.8614	0.33	1.38	0.54	0.9755	F	[204]
			1000	303	3	180	25	39.02	105.84	0.0016	0.9998	0.43	0.77	0.73	0.9988	L	[204]
		Sugarcane bagasse (SCB)	50	303	3	60	5	8.88	13.49	0.0102	0.7747	0.56	0.78	0.52	0.9200	F	[204]
			400-1000	303	3	–	–	37.34	73.83	0.0015	0.9493	0.48	0.88	0.60	0.9642	F	[204]
		Sawdust (SD)	50	303	3	60	5	11.13	13.02	0.0327	0.9531	0.31	1.34	0.34	0.9405	L	[204]
			1000	303	2	180	10	26.58	29.86	0.0122	1	0.1	2.72	0.15	0.9891	L	[204]
		Phragmites Australis (PA)	50	303	3	60	5	11.07	19.72	0.0076	0.7611	0.62	0.70	0.63	0.9693	F	[204]
			400-1000	303	3	–	–	18.59	19.30	0.0415	1	0.03	3.12	0.05	0.9950	L	[204]
		Teak Sawdust	60	AT	5.97	60	40	0.8931*	–	–	–	–	1481.7	26.7379	0.9375	F	[203]
		Rice husks	60	AT	6.68	60	40	0.6335*	–	–	–	–	56.6	1.5656	0.9389	F	[203]
		Cactus	6	298	2	60	0.125[a']	–	4.587	7.5	0.999	0.062–0.013	5.57	1.98	0.956	L	[205]
Tannery wastewater	Biomass-derived activated carbon	H₃PO₄-treated rice husk (RH-AC)	3.249	298	6.28	180	0.3[a']	–	3.55	0.00062	0.997	0.08	0.00046	3.096	0.973	L	[206]

Table 10 (*continued*)

Source of wastewater	Adsorbent type	Adsorbent	Initial Cr (VI) Conc. (mg/l)	T/ K	pH	Cont. t (min)	Dose (g/L)	Exp. q_m (mg/g)	Langmuir q_m (mg/ g)	K_L (L/mg)	R^2	R_L	Freundlich K_F	n	R^2	Isotherm model	Ref
		H_3PO_4 treated potato peel (PP-AC)	3.249	298	6.28	180	0.3[a']	–	0.94	0.00083	0.920	0.247	0.00036	1.888	0.989	F	[206]
		Charcoal-activated carbon (AC)	50	303	3	60	5	21.46	26.20	0.0424	0.986	0.26	1.46	0.49	0.9905	F	[204]
		Granular activated carbon	150	293	0.5	240	0.1[a']-2 [a']	–	8.02[e]	0.14[e]	0.97	0.98	1.441217[a]	−1.69[a]	0.90	L	[207]
			150	293	1	240	0.1[a']-2 [a']	–	1.03[f]	0.02[f]	0.90	0.99	1.441217[a]	−1.69[a]	0.95	F	[207]
			150	293	1.5	240	0.1[a']-2 [a']	–	8.02[e]	0.14[e]	0.97	0.98	1.441217[a]	−1.69[a]	0.90	L	[207]
			150	293	2	240	0.1[a']-2 [a']	–	1.03[f]	0.02[f]	0.90	0.99	1.120689[b]	−7.03[b]	0.95	F	[207]
			150	293	3	240	0.1[a']-2 [a']	–	8.02[e]	0.14[e]	0.97	0.98	1.120689[b]	−7.03[b]	0.90	L	[207]
			150	293	4	240	0.1[a']-2 [a']	–	1.03[f]	0.02[f]	0.90	0.99	1.120689[b]	−7.03[b]	0.95	F	[207]
			150	293	4.8	240	0.1[a']-2 [a']	–	8.02[e]	0.14[e]	0.97	0.98	1.120689[b]	−7.03[b]	0.90	L	[207]
			150	293	5.6	240	0.1[a']-2 [a']	–	1.03[f]	0.02[f]	0.90	0.99	1.120689[b]	−7.03[b]	0.95	L	[207]
			150	293	5.8	240	0.1[a']-2 [a']	–	8.02[e]	0.14[e]	0.97	0.98	1.120689[b]	−7.03[b]	0.90	L	[207]
			150	293	6.7	240	0.1[a']-2 [a']	–	1.03[f]	0.02[f]	0.90	0.99	1.120689[b]	−7.03[b]	0.95	L	[207]
			150	293	7.6	240	0.1[a']-2 [a']	–	8.02[e]	0.14[e]	0.97	0.98	1.441217[a]	−1.69[a]	0.90	L	[207]
			150	293	8	240	0.1[a']-2 [a']	–	1.03[f]	0.02[f]	0.90	0.99	1.120689[b]	−7.03[b]	0.95	L	[207]
			25	293	5.5	240	0.1[a']-2 [a']	–	11.13	0.18	0.99	0.99	0.35	2.17	0.97	L	[207]
			50	293	5.5	240	0.1[a']-2 [a']	–	11.13	0.18	0.99	0.99	0.35	2.17	0.97	L	[207]
			75	293	5.5	240	0.1[a']-2 [a']	–	11.13	0.18	0.99	0.98	0.35	2.17	0.97	L	[207]
			100	293	5.5	240	0.1[a']-2 [a']	–	11.13	0.18	0.99	0.98	0.35	2.17	0.97	L	[207]
			120	293	5.5	240	0.1[a']-2 [a']	–	11.13	0.18	0.99	0.97	0.35	2.17	0.97	L & F	[207]
			120	293	5.5	240	0.1[a']-2 [a']	–	9.72	0.93	0.99	0.90	1.14	−9.98	0.98	F	[207]
			120	313	5.5	240	0.1[a']-2 [a']	–	9.72	0.93	0.99	0.90	1.14	−9.98	0.98	F	[207]
			120	333	5.5	240	0.1[a']-2 [a']	–	9.72	0.93	0.99	0.90	1.14	−9.98	0.98	F	[207]
			120	343	5.5	240	0.1[a']-2 [a']	–	9.72	0.93	0.99	0.90	1.14	−9.98	0.98	F	[207]
Tannery wastewater	Nanocomposite	MNPs/rGO/PMMA nanocomposite	1640	–	2	30	15	–	240.96	4.021	0.991	–	6.85	2.85	0.972	L	[208]
		GO-Fe_3O_4	82.38 ± 3.21	–	4.3	120	10	–	16.88	68.83	0.999	0.0062	15.45	−3.225	0.994	L	[209]
Tannery wastewater	PANI polymer composite	Fe_3O_4@PANI/IA magnetic nanocomposite	100	298	8-10	60	20	–	218	0.72	0.968	0.05	86.21	0.925	0.995	F	[210]
Electroplating wastewater	Biosorbent	Coconut coir pith	1647	288	2	1080	0.01–0.18[a']	–	138.04	0.011	0.996	0.058	–	–	–	L	[211]
			1647	303	2	1080	0.01–0.18[a']	–	197.23	0.018	0.997	0.036	–	–	–	L	[211]
			1647	318	2	1080	0.01–0.18[a']	–	262.89	0.022	0.995	0.030	–	–	–	L	[211]
			1647	333	2	1080	0.01–0.18[a']	–	317.65	0.033	0.984	0.020	–	–	–	L	[211]
		Leechi (Litchi chinensis) fruit peel	50	303	2	1440	10	–	−34.48	−0.020	0.894	−10.00	0.686	0.599	0.947	F	[212]
			50	313	2	1440	10	–	101.10	0.012	0.977	0.625	1.330	1.125	0.967	L	[212]
			50	323	2	1440	10	–	75.98	0.024	0.956	0.454	2.450	1.580	0.837	L	[212]
		Walnut Shell Powder	40	303	2	60	0.5	–	138.89	0.039	0.999	–	14.09	2.16	0.969	L	[213]

Table 10 (*continued*)

Source of wastewater	Adsorbent type	Adsorbent	Initial Cr (VI) Conc. (mg/l)	T/ K	pH	Cont. t (min)	Dose (g/L)	Exp. q_m (mg/g)	Langmuir				Freundlich			Isotherm model	Ref
									q_m (mg/g)	K_L (L/mg)	R^2	R_L	K_F	n	R^2		
		Powdered pistachio hull (PHP)	85.5	–	3.2	720	5	119	117.6	0.16	0.986	–	41.1	4.0	0.945	L	[214]
		Aspergillus niger fungal biosorbent	30	298	2	60	12	–	17.61	0.0026	0.98	–	17.92	1.18	0.99	F	[215]
		Aspergillus sydoni fungal biosorbent	30	298	2	60	16	–	9.07	0.0022	0.97	–	8.06	1.01	0.95	L	[215]
		Penicillium janthinellum fungal biosorbent	30	298	2	60	16	–	9.35	0.0042	0.95	–	9.05	1.1	0.91	L	[215]
		Aspergillus niger fungal biosorbent	20	303	2	60	4.59	–	17.51	0.0025	0.98	–	17.92	1.18	0.99	F	[216]
		Aspergillus niger fungal biosorbent	117	301	4.1	–	1	–	16.3934	0.3041	0.9893	0.0318	–	–	–	L	[217]
		P. orientalis bark	86.39	298	5	300	2	–	13.423	0.670	0.995	–	1.316	1.282	0.996	F	[218]
		Corn straw biochar	112	298	3	960	1	175.44	176.37	0.16	0.9955	–	93.66	8.5251	0.9899	L	[219]
			112	313	3	960	1	218.38	215.98	0.14	0.9803	–	106.25	8.0515	0.8865	L	[219]
			112	328	3	960	1	236.72	234.74	0.19	0.9862	–	112.51	7.2411	0.9272	L	[219]
Electroplating wastewater	Biomass-derived activated carbon	HNO$_3$-treated *P. orientalis* bark-activated carbon	86.39	298	5	300	2	–	19.920	0.524	0.998	–	1.695	1.175	0.998	F	[218]
		H$_2$SO$_4$ treated Aspergillus niger fungal biosorbent	117	301	4.1	–	1	–	20.1613	0.10894	0.9987	0.0841	–	–	–	L	[217]
		NaOH-treated Aspergillus niger fungal biosorbent	117	301	4.1	–	1	–	26.666	0.3495	0.9910	0.0278	–	–	–	L	[217]
		NaOH treated corncob based activated (CAC)	1080	298	4.5	1440	15	–	12.6817	0.103554	0.91384	–	3.34	3.741495	0.9962	F	[220]
		KOH-treated peanut shell-based activated carbon (PAC)	670.31	298	3	1440	1	–	208.33	0.9057	0.9986	–	99.46	4.4914	0.6759	L	[221]
		Magnetic KOH-treated peanut shell-based activated carbon (MPAC)	670.31	298	3	1440	2	–	192.31	0.4094	0.9984	–	78.63	4.5562	0.8384	L	[221]
		Commercial Activated Carbon (CAC)	670.31	298	3	1440	1	–	138.89	0.3789	0.9988	–	56.66	5.1501	0.8231	L	[221]
		Commercial activated carbon based on coconut coir pith	1647	288	2	1080	0.01–0.18[a']	–	137.61	0.007	0.999	0.089	–	–	–	L	[211]
			1647	303	2	1080	0.01–0.18[a']	–	185.01	0.013	0.999	0.049	–	–	–	L	[211]
			1647	318	2	1080	0.01–0.18[a']	–	246.16	0.016	0.997	0.038	–	–	–	L	[211]
			1647	333	2	1080	0.01–0.18[a']	–	302.80	0.023	0.991	0.028	–	–	–	L	[211]
		Powdered Activated Carbon (PAC)	85.5	–	3.2	720	5	125	47.6	0.09	0.980	–	8	2.1	0.354	L	[214]
Electroplating wastewater	Nanocomposite	Thioacetamide (TAA) sulfur precursor-based Bi$_2$S$_3$ nanostructures	109.56	303	2.12	–	0.02[a']	–	125.97	0.0688	0.9421	–	19.22	0.4398	0.9767	F	[222]
			9.48	303	2.14	–	0.02[a']	–	140.97	0.1576	0.9821	–	26.38	0.5285	0.9778	L	[222]

(*continued on next page*)

Table 10 (*continued*)

Source of wastewater	Adsorbent type	Adsorbent	Initial Cr (VI) Conc. (mg/l)	T/ K	pH	Cont. t (min)	Dose (g/L)	Exp. q_m (mg/g)	Langmuir				Freundlich			Isotherm model	Ref
									q_m (mg/g)	K_L (L/mg)	R^2	R_L	K_F	n	R^2		
		L-cysteine (L-Cys) sulfur precursor-based Bi$_2$S$_3$ nanostructures	109.56	303	2.12	–	0.02[a']	–	223.33	0.9271	0.9417	–	110.17	0.2596	0.9613	F	[222]
			9.48	303	2.14	–	0.02[a']	–	240.25	0.4983	0.9939	–	87.32	0.4223	0.9739	L	[222]
		Amino-functionalized vermiculite-supported nanoscale zero-valent iron (AVT-nZVI)	20	303	5	60	0.625	–	59.17	3.8409	0.9887	–	40.0809	6.1	0.6968	L	[223]
Petroleum refinery wastewater	Nanocomposite	γ-Fe$_2$O$_3$ nanoparticles	50	298	2.5	–	5	–	17.43	0.327	0.995	0.058	–	–	–	L	[224]
		G nanosheets	1.45 ± 0.89	298	–	180	12	–	80	0.014	0.8714	0.0094	7.9	2.9	0.9883	F	[225]
		GO nanosheets	1.45 ± 0.89	298	–	180	12	–	65.71	0.02	0.8938	0.18	18.33	2.5	0.982	F	[225]
		CdO NPs	1.45 ± 0.89	298	–	180	12	–	400	0.46	0.9304	0.29	110	4.5	0.9929	F	[225]
		G-CdO nanocomposite	1.45 ± 0.89	298	–	180	12	–	430	0.89	0.9543	0.0179	149	6	0.9969	F	[225]
		CdO-GO nanocomposites	1.45 ± 0.89	298	–	180	12	–	699.46	0.8	0.9834	0.0134	11.61	13	0.9993	F	[225]

Fe$_3$O$_4$@PANI/IA magnetic nanocomposite = polyaniline-itaconic acid magnetic nanocomposite; γ-Fe$_2$O$_3$ nanoparticles = Maghemite nanoparticles; G nanosheets = Graphene nanosheets; GO nanosheets = Graphene Oxide nanosheets; CdO NPs = CdO nanoparticles; G-CdO nanocomposite = Graphene modified CdO nanocomposite; CdO-GO nanocomposites = CdO modified Graphene Oxide nanocomposite; MNPs/rGO/PMMA composite = magnetic nanoparticle (MNP)-reduced graphene oxide (rGO) and polymethylmethacrylate (PMMA) composite; a' = Adsorbent dose in g; b' = R_L at 50nullmg/l initial Cr(VI) concentration; c' = q_m units in mmol/g; d' = K_L units in L/g; AT = Ambient Temperature; * = Calculated based on the total volume of influent passed through the column and total weight of the adsorbents in the column; a = 50nullmg/L ≤ Ce ≤ 140nullmg/L; b = 10nullmg/L ≤ Ce ≤ 50nullmg/L; c = 1.6nullmg/L ≤ Ce ≤ 2.5nullmg/L; d = 1.0nullmg/L ≤ Ce ≤ 1.6nullmg/L; e = 9.0nullmg/L ≤ Ce ≤ 70nullmg/L; f = 70nullmg/L ≤ Ce ≤ 135nullmg/L; L = Langmuir adsorption isotherm; F = Freundlich adsorption isotherm.
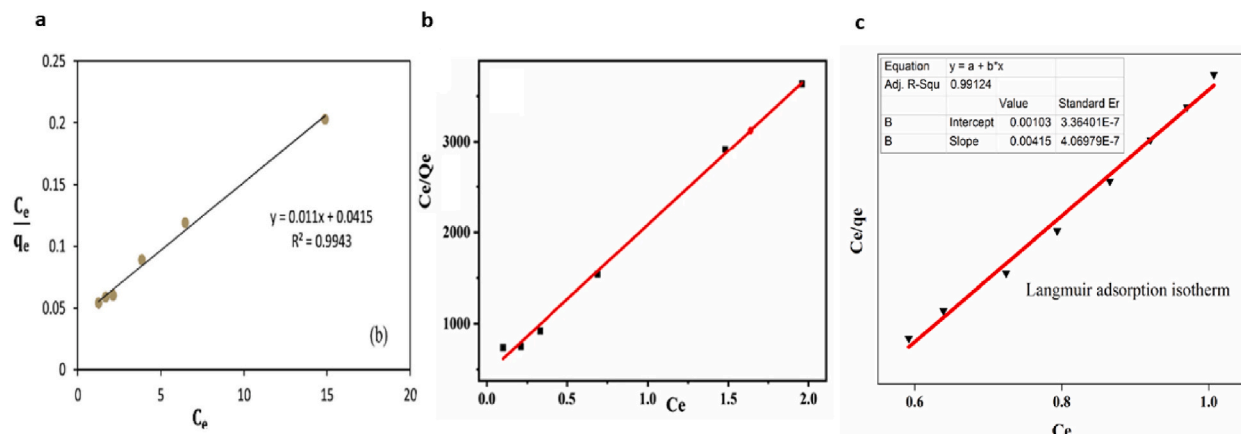
Fig. 24. Langmuir isotherm model of Cr(VI) removal for Tannery industrial wastewater using **(a)** Tea waste [197], **(b)** H_3PO_4 treated rice husk (RH-AC) [206], and **(c)** MNPs/rGO/PMMA nanocomposite [208].
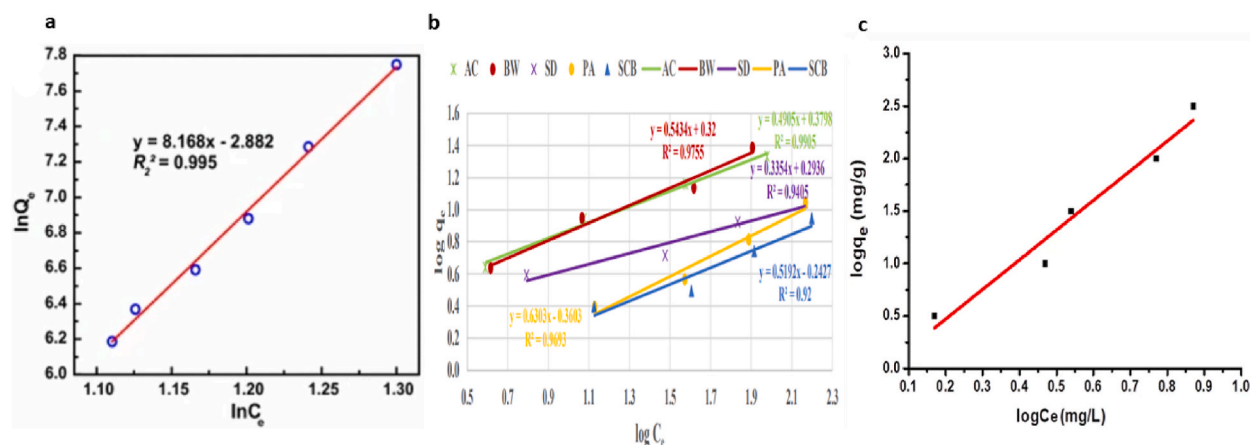
Fig. 25. Freundlich isotherm model of Cr(VI) removal for Tannery industrial wastewater using **(a)** Syzygium cumini bark [198], **(b)** Banana waste (BW), Sawdust (SD), Phragmites Australis (PA), Sugarcane Bagasse (SCB), and Charcoal activated carbon (AC) at low concentration [204], and **(c)** Fe_3O_4@PANI/IA magnetic nanocomposite [210].
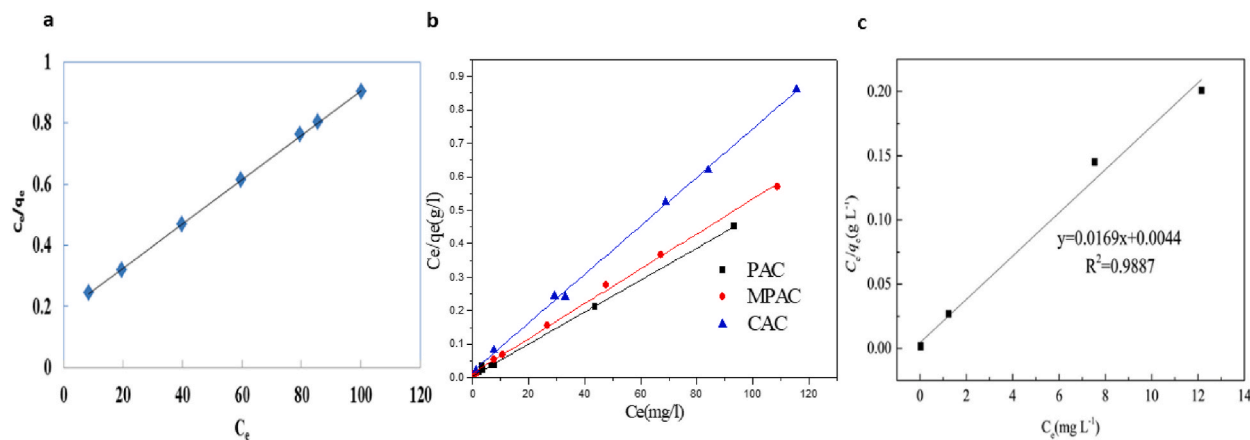
Fig. 26. Langmuir isotherm model of Cr(VI) removal for Electroplating industrial wastewater using **(a)** Walnut Shell Powder [212], **(b)** KOH-treated peanut shell-based activated carbon (PAC), Magnetic KOH-treated peanut shell-based activated carbon (MPAC), and Commercial activated carbon (CAC) [221], and **(c)** Amino-functionalized vermiculite-supported nanoscale zero-valent iron (AVT-nZVI) [223].
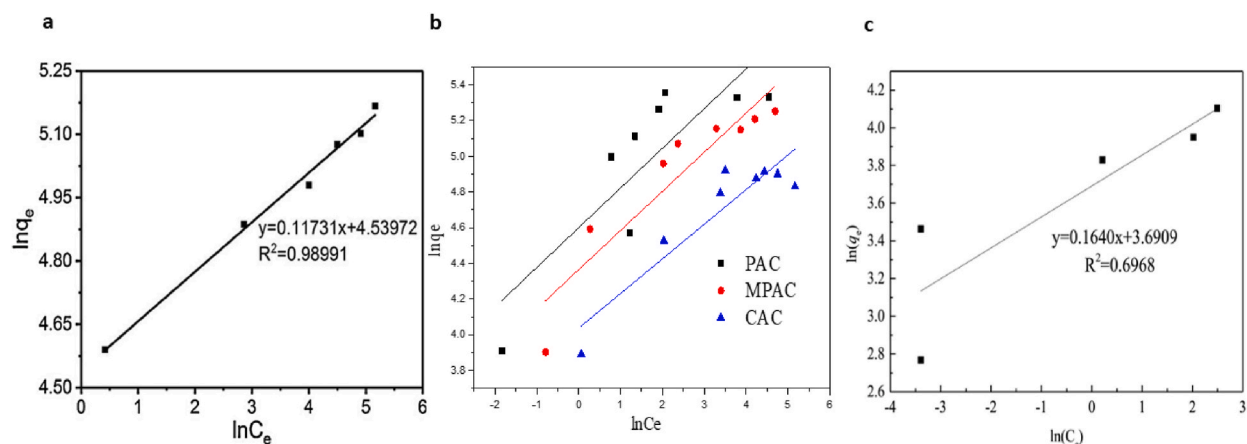
Fig. 27. Freundlich isotherm model of Cr(VI) removal for Electroplating industrial wastewater using **(a)** Corn straw biochar [219], **(b)** KOH-treated peanut shell-based activated carbon (PAC), Magnetic KOH-treated peanut shell-based activated carbon (MPAC), and Commercial activated carbon (CAC) [221], and **(c)** Amino-functionalized vermiculite-supported nanoscale zero-valent iron (AVT-nZVI) [223].

PANI-based adsorbents for Cr(VI) adsorption were evaluated using the experimental and calculated amounts of Cr(VI) adsorbed at equilibrium ($q_{e,exp}$, $q_{e,cal}^{I}$, $_{and\ qe,cal}^{II}$), as well as the pseudo-first-order rate constant (k_1), pseudo-second-order rate constant (k_2) and R^2 value. Table 9 lists the experimental and calculated amounts of Cr(VI) adsorbed at equilibrium, pseudo-first-order and pseudo-second-order rate constants, and R^2 values obtained for PANI-based adsorbents for Cr(VI) adsorption.

The linear pseudo-first-order kinetic and pseudo-second-order kinetic models of PANI-based adsorbents for Cr(VI) adsorption are shown in Figs. 17 and 18, respectively.

The PANI/γ-Fe$_2$O$_3$ exhibited the highest experimental and calculated amounts of Cr(VI) adsorbed at equilibrium ($q_{e,exp}$, $q_{e,cal}^{I}$, $_{and\ qe,cal}^{II}$) among other PANI-based adsorbents, with the highest R^2 value of the pseudo-second-order kinetic model as shown in Fig. 18 (a) indicating chemical sorption involving valence forces through sharing or exchange of electrons between the PANI-based adsorbent and Cr(VI) as compared to pseudo-first-order kinetic model [154]. However, the lowest pseudo-second-order kinetic constant is observed in the PANI/γ-Fe$_2$O$_3$ [154]. In contrast, PANI/PA composite achieved the lowest experimental and calculated amounts of Cr(VI) adsorbed at equilibrium ($q_{e,exp}$, $q_{e,cal}^{I}$, $_{and\ qe,cal}^{II}$) by pseudo-first-order and pseudo-second-order kinetic models among others PANI-based adsorbents while following pseudo-second-order kinetic model [195].

However, PPy-PANI/Fe$_3$O$_4$ (PANI-based adsorbent) best fits with the calculated amount of Cr(VI) adsorbed at equilibrium ($q_{e,cal}^{I}$) by the pseudo-second-order kinetic model as indicated by its correlation of coefficient for a pseudo-second-order kinetic model is unity (Fig. 18 (b)) [186]. However, pseudo-second-order kinetic modelling of PPy-PANI/Fe$_3$O$_4$ (PANI-based adsorbent) at different temperatures also shows good best-fit results (Fig. 18 (c)) [186].

Furthermore, it was also observed that the increase in initial Cr(VI) concentration and temperature significantly enhanced the amount of qe. All of the PANI-based adsorbents, including (PANI/PI) microfiber membranes [185], PPy-PANI/Fe$_3$O$_4$ [186], PANI nanosheets [187], PANI nanotubes [187], PANI nanofibers [187], (PANI/EVOH) nanofiber composite membranes [188], PANI/LDHs (LDHs/aniline mass ratio of 1:8) [190], PANI/H-TNB (H-TNBs/aniline mol ratio of 1: 20) [191], PANI/PVA composite [192], SA-PANI [193], PANI/γ-Fe$_2$O$_3$ [154], and PANI-MWCNT [194], PANI/PA composite [195] followed the chemical sorption as indicated by their higher R^2 values of the pseudo-second-order kinetic model. However, the worst fit pseudo-first-order kinetic model was observed as their R^2 values were less than 0.9 in the order PANI/ γ-Fe$_2$O$_3$ [154]< PANI/PVA composite [192]< (PANI/EVOH) nanofiber composite membranes (Fig. 17 (c)) [188]< PANI/PA composite [195]< PANI-MWCNT [194]. Thus, it can be concluded that pseudo-second-order kinetics modeling of PANI-based adsorbents better described the experimental values than a pseudo-first-order kinetic model of (PANI/PI) microfiber membranes [185], PPy-PANI/Fe$_3$O$_4$ (Fig. 17 (a)) [186], PANI nanosheets [187], PANI nanotubes [187], PANI nanofibers (Fig. 17 (b)) [187], (PANI/EVOH) nanofiber composite membranes [188], PANI/LDHs (LDHs/aniline mass ratio of 1:8) [190], PANI/H-TNB (H-TNBs/aniline mol ratio of 1: 20) [191], PANI/PVA composite [192], SA-PANI [193], PANI/γ-Fe$_2$O$_3$ [154], and PANI-MWCNT [194], PANI/PA composite [195].

5. Effect of operational parameters on the Langmuir's maximum adsorption capacity (q$_m$)

The operational parameters have significant effects on the q$_m$. The operational parameters used for the adsorption of Cr(VI) using various adsorbents are enlisted below: Initial Cr(VI) concentration; temperature; pH; contact time; adsorbent dosage.

5.1. Effect of Initial Cr(VI) concentration

The effect of initial concentration on the maximum adsorption capacity of various types of adsorbents such as biosorbents (fruit waste, fungus, leaf, and biochar), activated carbon (acid-treated, base-treated, and acid/base-treated), nanocomposite (Fe-based, Mn-

Table 11

Pseudo-first-order and pseudo-second-order kinetic model constants obtained for Cr(VI) heavy metal adsorption by using adsorbents in industrial wastewater.

Source of wastewater	Adsorbent type	Adsorbent	Initial Cr (VI) Conc. (mg/l)	T/K	pH	Dose (g/L)	$q_{e,exp}$ (mg/g)	Pseudo-first order kinetic model			Pseudo-second order kinetic model			Kinetic model	Ref
								$q^I_{e,cal}$ (mg/g)	k_1 (1/min)	R^2	$q^{II}_{e,cal}$ (mg/g)	k_2 (g/mg·min)	R^2		
Tannery wastewater	Biosorbent	Tea waste	455	303	3.9	6	73.35	78.91	0.0173	0.9666	88.49	0.000212	0.9901	PSO	[197]
		Syzygium cumini bark	2920.2 ± 0.7	293	3.9 ± 0.1	3[a]	–	−0.00223	0.101	0.997	−2.29885	−0.0654	0.92	PFO	[198]
		Corn cob	100	298	2	0.1[a]	–	82.22	0.002441	0.488	29.41	944	0.999	PSO	[199]
		Avocado kernel seeds (AKS)	5	298	1	0.5[a], 16.66	–	0.0646	0.0253	0.820	0.2803	2.6413	0.999	PSO	[200]
		Juniperus procera sawdust (JPS)	5	298	1	0.5[a], 16.66	–	0.0592	0.0253	0.807	0.2986	1.1916	0.998	PSO	[200]
		Papaya peels (PP)	5	298	1	0.5[a], 16.66	–	0.0678	0.0253	0.827	0.2691	3.1837	1.000	PSO	[200]
		Banana peel	0.1–100	293	2	10	–	3.643×10^{-5} *	0.183 ± 0.005	0.993	–	–	–	PFO	[201]
		Oil-free Moringa oleifera cake (OFMOC)	0.75	301.85	7	1.5[a]	–	0.7819	0.049	0.841	0.66697	0.000 82	0.115	PFO	[201]
		Sweet potatoes peels (SPP)	0.75	301.85	7	2.5[a]	–	0.3712	0.032	0.84	1.8698×10^{-10}	0.117 7	0.772 2	PFO	[201]
		Orange (Citrus cinensis) peel adsorbent	46.71	RT	2	2.5	–	5.3585	0.009	0.9641	6.5617	0.0036	0.99	PSO	[202]
		Banana waste (BW)	–	303	3	5	9.02	0.51	0.481	0.9975	8.798	6.12	0.9987	PFO	[204]
		Sugarcane Bagasse (SCB)	–	303	3	5	6.52	3.83	0.405	0.6318	7.972	0.091	0.9352	PSO	[204]
		Sawdust (SD)	–	303	3	5	8.41	6.76	0.787	0.7866	10.05	0.104	0.9924	PSO	[204]
		Phragmites Australis (PA)	–	303	3	5	5.04	2.24	0.404	0.9911	5.21	0.435	0.9837	PFO	[204]
Tannery wastewater	Biomass-derived activated carbon	H_3PO_4-treated rice husk (RH-AC)	3.249	298	6.28	0.3[a]	–	–	–	–	–	–	>0.9	PSO	[206]
		H_3PO_4 treated potato peel (PP-AC)	3.249	298	6.28	0.3[a]	–	–	–	–	–	–	>0.9	PSO	[206]
		Charcoal Activated Carbon (AC)	–	303	3	5	9.05	8.26	2.76	0.9712	8.473	1.24	0.9977	PSO	[204]
		Granular activated carbon	120	293.15	5.5	0.1[a]-2[a]	–	–	1.96×10^2	0.96	–	1.77×10^2	0.85	PFO	[207]
			120	313.15	5.5	0.1[a]-2[a]	–	–	2.25×10^2	0.95	–	3.62×10^2	0.93	PFO	[207]
			120	333.15	5.5	0.1[a]-2[a]	–	–	2.93×10^2	0.96	–	3×10^2	0.98	PSO	[207]
			120	343.15	5.5	0.1[a]-2[a]	–	–	3.29×10^2	0.98	–	3.68×10^2	0.99	PSO	[207]
Tannery wastewater	Nanocomposite	MNPs/rGO/PMMA nanocomposite	1640	–	2	15	109.33	23.93	0.151	0.86	166.66	0.362	0.98	PSO	[208]
Electroplating wastewater	Biosorbent	Leechi (Litchi chinensis) fruit peel	10	303	2	10	0.23	0.17	0.060	0.9868	0.26	0.660	0.9852	PFO	[212]
			20	303	2	10	1.04	0.19	0.060	0.9227	1.06	0.750	0.9996	PSO	[212]
			50	303	2	10	2.50	1.28	0.070	0.9293	2.67	0.100	0.9983	PSO	[212]

Table 11 (*continued*)

Source of wastewater	Adsorbent type	Adsorbent	Initial Cr(VI) Conc. (mg/l)	T/K	pH	Dose (g/L)	$q_{e,exp}$ (mg/g)	Pseudo-first order kinetic model			Pseudo-second order kinetic model			Kinetic model	Ref
								$q_{e,cal}^{I}$ (mg/g)	k_1 (1/min)	R^2	$q_{e,cal}^{II}$ (mg/g)	k_2 (g/mg·min)	R^2		
			60	303	2	10	3.60	3.41	0.014	0.9857	3.64	0.003	0.9357	PFO	[212]
			80	303	2	10	5.00	4.49	0.010	0.9610	6.78	0.001	0.9078	PFO	[212]
			100	303	2	10	6.70	5.38	0.008	0.9668	7.59	0.002	0.9915	PSO	[212]
		Walnut Shell Powder	40	303	2	0.5	–	10.186	0.014	0.926	71.429	0.0002	0.999	PSO	[213]
		Powdered pistachio hull (PHP)	85.5	–	3.2	1	–	–	–	–	–	0.004	0.991	PSO	[214]
			85.5	–	3.2	2	–	–	–	–	–	0.006	0.993	PSO	[214]
			85.5	–	3.2	3	–	–	–	–	–	0.013	0.997	PSO	[214]
			85.5	–	3.2	4	–	–	–	–	–	0.015	0.994	PSO	[214]
			85.5	–	3.2	5	–	–	–	–	–	0.030	0.997	PSO	[214]
		Aspergillus niger fungal biosorbent	20	303	2	1	19.23	14.35	0.043	0.970	20.83	0.0049	0.999	PSO	[216]
		Corn straw biochar	112	298	3	1	98.48	19.45	0.36[b]	0.8300	98.91	0.08[c]	0.9995	PSO	[219]
Electroplating wastewater	Biomass-derived activated carbon	Aspergillus niger	100	301	1.5	1[a]	–	–	–	–	–	–	–	PFO	[217]
		H$_2$SO$_4$ treated Aspergillus niger	100	301	1.5	1[a]	–	–	–	–	–	–	–	PFO	[217]
		NaOH-treated Aspergillus niger	100	301	1.5	1[a]	–	–	–	–	–	–	–	PFO	[217]
		NaOH treated corncob based activated (CAC)	72	298	4.5	15	–	4.32	0.0119	0.9951	4.87	0.00054	0.999	PSO	[220]
		KOH-treated peanut shell-based activated carbon (PAC)	100	298	3	1	97.73	21.10	24.3	0.765	98.04	6.42	1.000	PSO	[221]
		Magnetic KOH-treated peanut shell-based activated carbon (MPAC)	100	298	3	2	98.88	13.98	21.5	0.629	99.01	10.52	1.000	PSO	[221]
		Powdered Activated Carbon (PAC)	85.5	–	3.2	1	–	–	–	–	–	0.001	0.994	PSO	[214]
			85.5	–	3.2	2	–	–	–	–	–	0.002	0.976	PSO	[214]
			85.5	–	3.2	3	–	–	–	–	–	0.005	0.994	PSO	[214]
			85.5	–	3.2	4	–	–	–	–	–	0.014	0.992	PSO	[214]
			85.5	–	3.2	5	–	–	–	–	–	0.028	0.998	PSO	[214]
		Commercial Activated Carbon (CAC)	100	298	3	1	87.69	42.23	13.6	0.848	89.93	1.26	0.999	PSO	[221]
Electroplating wastewater	Nanocomposite	Amino-functionalized vermiculite-supported nanoscale zero-valent iron (AVT-nZVI)	10	303	5	0.625	–	–	0.8629	0.9965	16.07	0.9354	1	PSO	[223]
			20	303	5	0.625	–	–	0.1201	0.9564	32.91	0.0154	0.9998	PSO	[223]
			30	303	5	0.625	–	–	0.0437	0.8830	47.35	0.0070	0.9993	PSO	[223]
			40	303	5	0.625	–	–	0.0246	0.7665	53.02	0.0071	0.9989	PSO	[223]
			50	303	5	0.625	–	–	0.0203	0.7194	60.94	0.0059	0.9949	PSO	[223]
		γ-Fe$_2$O$_3$ nanoparticles	50	298	2.5	5	17	–	–	–	–	–	–	–	[224]
Petroleum refinery wastewater	Nanocomposite	G nanosheets	1–1500	298	1–10	1[a]–6[a]	–	24.72	3.76	0.9834	48.17	3.23	0.9993	PSO	[225]
		GO nanosheets	1–1500	298	1–10	1[a]–6[a]	–	35.1	8.5	0.9587	86.12	7.33	0.9990	PSO	[225]
		CdO NPs	1–1500	298	1–10	1[a]–6[a]	–	44.53	4.9	0.9323	168.39	3.61	0.9994	PSO	[225]
		G-CdO nanocomposite	1–1500	298	1–10	1[a]–6[a]	–	119.86	12.89	0.9767	249	2.33	0.9995	PSO	[225]
		CdO-GO nanocomposites	1–1500	298	1–10	1[a]–6[a]	–	51.27	54.2	0.7231	311.40	3.83	0.9995	PSO	[225]

a = Adsorbent Dosage units in g; b = k_1 units in 1/h; c = k_2 units in g/mg·h; * = $q_{e,cal}^{I}$ units in mol/g; PFO= Pseudo-first-order kinetic model; PSO= Pseudo-second-order kinetic model.
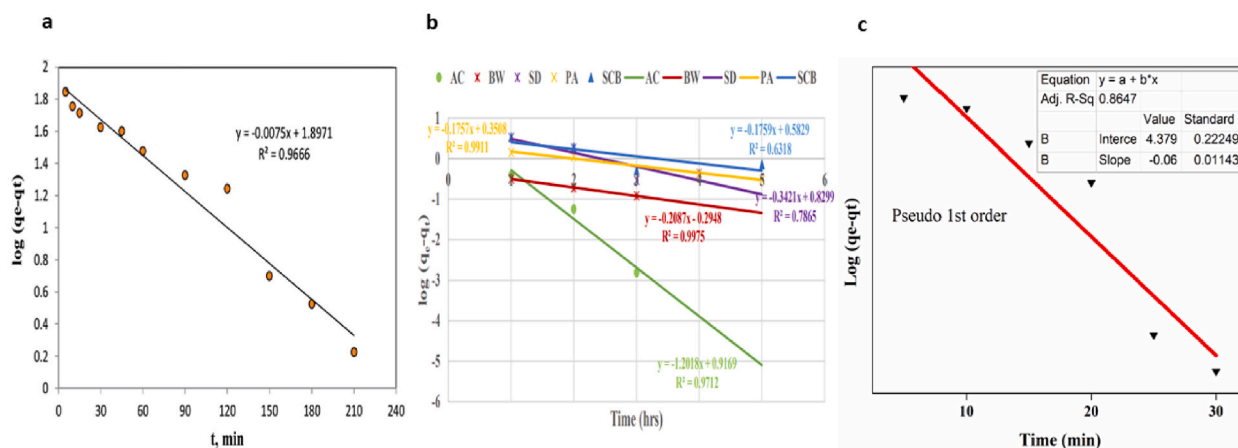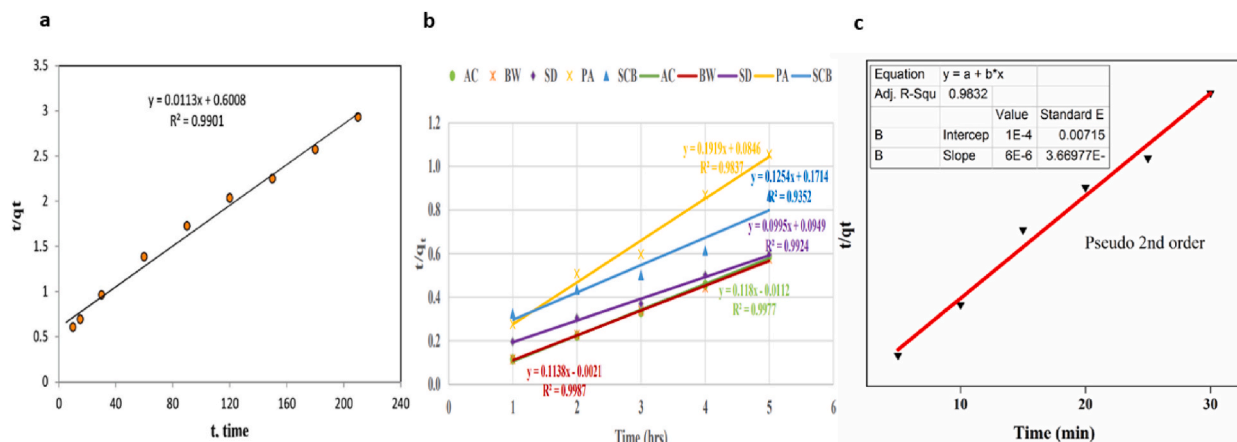
Fig. 28. Pseudo-first-order kinetic model of Cr(VI) removal for Tannery industrial wastewater using **(a)** Tea waste [197], **(b)** Tannery wastewater using Banana waste (BW), Sawdust (SD), Phragmites Australis (PA), Sugarcane Bagasse (SCB), and Charcoal activated carbon (AC) [204], and **(c)** MNPs/rGO/PMMA nanocomposite [208].

based, Cu-based, and graphene-based), and PANI are shown in Fig. 19 which is discussed in detail below:

The study found that fruit waste biosorbents demonstrated an exponential increase in the maximum adsorption capacity as the initial Cr(VI) concentration increased [112,117,118]. On the other hand, biochar biosorbents showed an increase in maximum adsorption capacity with initial Cr(VI) concentration [116,125]. Fungal biosorbents had a smooth rising peak, followed by a decline in maximum adsorption capacity [106,113,119–121]. Similarly, leaf biosorbents showed a slowly declining peak followed by a slow increase in maximum adsorption capacity with initial Cr(VI) concentration [114,115,122–124]. Therefore, the data suggest that an increase in initial Cr(VI) concentration results in higher maximum adsorption capacity in the case of fruit waste and biochar bio-sorbents [112,116–118,125].

For acid-treated activated carbons, multiple peaks of incline and decline in maximum adsorption capacity with increased initial Cr (VI) concentration [107,130–137]. In contrast, base-treated and acid/base-treated activated carbon demonstrated an increase in maximum adsorption capacity with an increase in initial Cr(VI) concentration [125,130,138,139]. Thus, the effect of initial Cr(VI) concentration on the maximum adsorption capacity of activated carbons depends on the type of treatment applied.

Fe-based nanocomposite showed a parabolic decline followed by increased maximum adsorption capacity as the initial Cr(VI) concentration increased [150–154]. Conversely, Mn-based nanocomposite adsorbents demonstrated an exponential rise in maximum adsorption capacity with increasing Cr(VI) concentration [155,156]. Graphene-based nanocomposite adsorbents showed multiple peaks of maximum adsorption capacity, increasing with initial Cr(VI) concentration [150,159–169]. Therefore, the findings suggest that the functional group or component attached to the nanocomposite adsorbents significantly alters the effect of initial Cr(VI) concentration on maximum adsorption capacity.

Similarly, PANI-based adsorbents demonstrated multiple peaks of maximum adsorption capacity, increasing and declining with increasing initial Cr(VI) concentration [154,185–188,190–195]. Hence, it could be interpreted that the functional group or component attached to the PANI-based adsorbents plays a significant role in the impact of initial Cr(VI) concentration on maximum adsorption capacity.

Therefore, it could be interpreted from the data that the effect of initial Cr(VI) concentration on the maximum adsorption capacity of adsorbents depends on the type of adsorbent used, the attached component/functional group, and the chemical treatments (acid, base, combination of acid/base) applied to the adsorbents.

5.2. Effect of temperature

The effect of temperature on the maximum adsorption capacity of various types of adsorbents such as biosorbents (fruit waste, fungus, leaf, and biochar), activated carbon (acid-treated, base-treated, and acid/base-treated), nanocomposite (Fe-based, Mn-based, Cu-based, and graphene-based), and PANI are shown in Fig. 20 which is discussed in detail below:

The results show that fruit waste bio sorbents show a decline in the maximum adsorption capacity due to pomegranate peel (fruit waste biosorbent) and then a rise in maximum adsorption capacity at higher temperatures [112,117,118]. Fungal and leaf biosorbents, on the other hand, have a peak followed by a decline in maximum adsorption capacity with increased temperature [106,113–115, 119–124]. However, biochar biosorbents showed little increase in maximum adsorption capacity with increased temperature [116, 125]. Therefore, the data suggest that an increase in the temperature of biosorbents results in higher maximum adsorption capacity in the case of fruit waste and biochar biosorbents [112,116–118,125].

Acid-treated activated carbons show inclined and declined peaks [107,130–137], while base-treated activated carbon shows a linear rise in the maximum adsorption capacity at higher temperatures [130,138]. Acid/base-treated activated carbon exhibit a decline in maximum adsorption capacity with increasing temperature [125,139]. Thus, the effect of temperature on the maximum adsorption

Fig. 29. Pseudo-second-order kinetic model of Cr(VI) removal for Tannery industrial wastewater using **(a)** Tea waste [197], **(b)** Tannery waste-water using Banana waste (BW), Sawdust (SD), Phragmites Australis (PA), Sugarcane Bagasse (SCB), and Charcoal activated carbon (AC) [204], and **(c)** MNPs/rGO/PMMA nanocomposite [208].
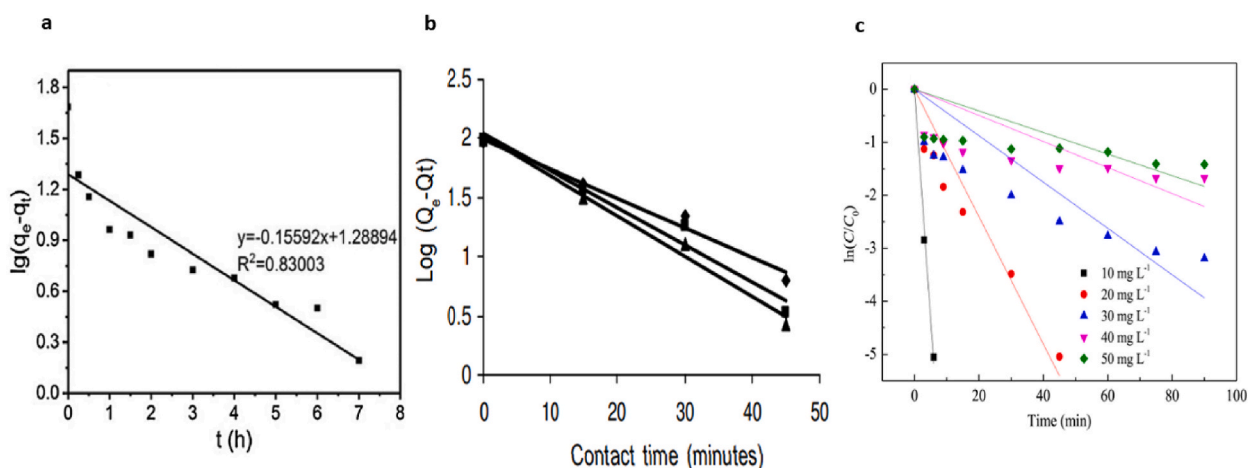
Fig. 30. Pseudo-first-order kinetic model of Cr(VI) removal for Electroplating industrial wastewater using (a) Corn straw biochar at 298 K [219], (b) H2SO4 treated Aspergillus niger fungal biosorbent (represented as ◆), NaOH treated Aspergillus niger fungal biosorbent (represented as ▲), and Aspergillus niger fungal biosorbent (represented as ■) [217], and (c) Amino-functionalized vermiculite-supported nanoscale zero-valent iron (AVT-nZVI) [223].

capacity of activated carbons depends on the type of treatment applied.

Fe-based and Mn-based nanocomposites show a rapid rise and a broader rise peak followed by declining peaks in the maximum adsorption capacity with increased temperature [150–156]. Cu-based nanocomposite adsorbents exhibit a linear rise in maximum adsorption capacity [158]. In contrast, graphene-based nanocomposite adsorbents show multiple sharp rising and declining peaks of maximum adsorption capacity with increased temperature [150,159–169].

Finally, PANI-based adsorbents exhibit multiple rise and decline peaks of maximum adsorption capacity with increased temperature [154,185–188,190–195]. Hence, the effect of temperature on maximum adsorption capacity depends on the type of adsorbent, the source of adsorbent, the element/component/functional group attached to the adsorbent, and chemical treatments (acid, base, combination of acid/base) of adsorbents.

5.3. Effect of pH

The effect of pH on the maximum adsorption capacity of various types of adsorbents such as biosorbents (fruit waste, fungus, leaf, and biochar), activated carbon (acid-treated, base-treated, and acid/base-treated), nanocomposite (Fe-based, Mn-based, Cu-based, and graphene-based), and PANI are shown in Fig. 21 which is discussed in detail below:

The fruit waste biosorbents show a rise in maximum adsorption capacity in the pH range (2–3). However, beyond pH 5, the
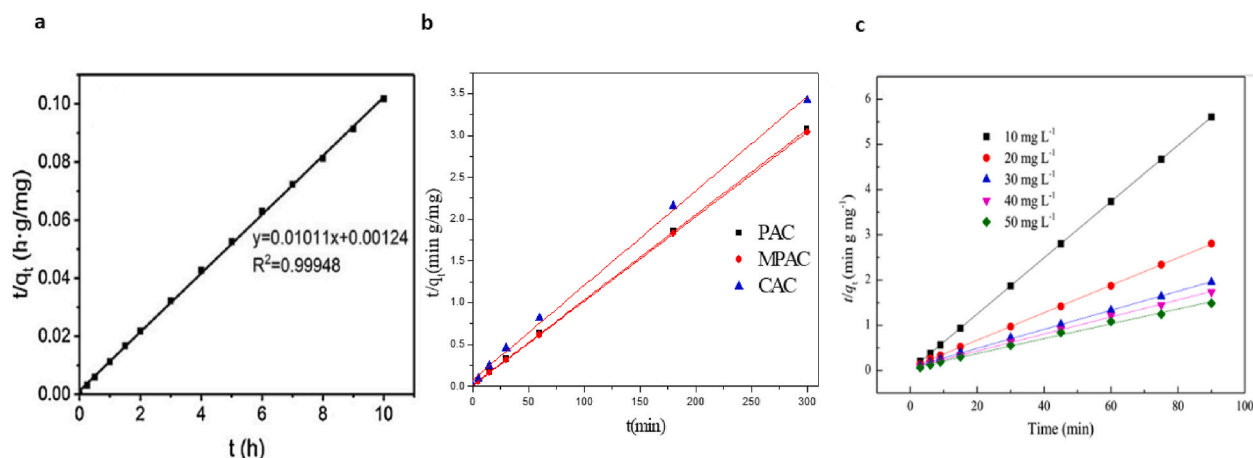
Fig. 31. Pseudo-second-order kinetic model of Cr(VI) removal for Electroplating industrial wastewater using **(a)** Corn straw biochar at 298 K [219], **(b)** KOH treated peanut shell based activated carbon (PAC), Magnetic KOH treated peanut shell based activated carbon (MPAC), and Commercial Activated Carbon (CAC) [221], and **(c)** Amino-functionalized vermiculite-supported nanoscale zero-valent iron (AVT-nZVI) [223].

maximum adsorption capacity declined [112,117,118]. Fungal biosorbents, on the other hand, show a decline in maximum adsorption capacity with an increase in the acidic pH range (1–5.5) [106,113,119–121]. However, leaf and biochar biosorbents show a little rise in maximum adsorption capacity with an increase in the acidic pH ranges (2–5.5 and 1.5–2) [114–116,122–125]. Therefore, it could be interpreted that within the acidic pH range (2), the biosorbents showed a maximum adsorption capacity.

Acid-treated activated carbons decline maximum adsorption capacity with an increased pH range (2–7) [107,130–137]. However, base-treated activated carbon showed a linear decrease in the maximum adsorption capacity with increased pH (6.8–8) [130,138]. Moreover, acid/base treated activated carbon increased maximum adsorption capacity in an acidic pH range [125,139]. However, it could be interpreted that the maximum adsorption capacity increases within the acidic pH range and decreases in the basic pH range. Hence, acid-treated activated carbon adsorbents have the maximum adsorption capacity compared to base-treated activated carbon and acid/base-treated activated carbon.

Fe-based nanocomposite showed a rapid decline and then a rise in maximum adsorption capacity on the increase in pH range (within the acidic region) and declines rapidly in the basic pH range [150–154]. Furthermore, Mn-based nanocomposite showed a linear increase in maximum adsorption capacity at a constant pH (2) [155,156]. Moreover, the Cu-based nanocomposite adsorbent showed a linear increase in the maximum adsorption capacity at a stable pH (3) [158]. Graphene-based nanocomposite adsorbent showed a rapid decline and a slight rise in maximum adsorption capacity with increased pH within the acidic range [150,159–169]. So, it could be interpreted that within the acidic pH range (2–6.8), the nanocomposite adsorbents show a higher maximum adsorption capacity.

PANI-based adsorbents showed a rise in maximum adsorption capacity with an increase in pH within the acid region (1–3) and then rapidly declined to a further rise in pH value. So, it could be interpreted that within the acidic pH range (1–3), the PANI-based adsorbents show a higher maximum adsorption capacity of PANI-based adsorbents [154,185–188,190–195].

Therefore, it could be stated that the effect of pH on the maximum adsorption capacity of adsorbents depends on the type of adsorbent used and the chemical treatments (acid, base, combination of acid/base) of adsorbents. The adsorbents show the highest maximum adsorption capacity within the acidic pH (1–3). Hence, an acidic pH range would be preferred for the adsorbents.

5.4. Effect of contact time

The effect of contact time on the maximum adsorption capacity of various types of adsorbents such as biosorbents (fruit waste, fungus, leaf, and biochar), activated carbon (acid-treated, base-treated, and acid/base-treated), nanocomposite (Fe-based, Mn-based, Cu-based, and graphene-based), and PANI are shown in Fig. 22 which is discussed in detail below:

The fruit waste biosorbents show an exponential decline in the maximum adsorption capacity with increased contact time [112, 117,118]. Fungal biosorbents, on the other hand, show a decline in maximum adsorption capacity with an increase in contact time of around 240 minutes, followed by an increase in maximum adsorption capacity with a further increase in contact time [106,113, 119–121]. Leaf biosorbents show a gradual declining and rising peak of the maximum adsorption capacity with increased contact time [114,115,122–124]. However, biochar biosorbents showed little increase in maximum adsorption capacity with increased contact time [116,125]. Therefore, it could be interpreted that the biosorbents showed a decline in the maximum adsorption capacity with the increase in contact time.

Acid-treated activated carbons show inclined and declined peaks with the increase in contact time and a rapid ready peak at a contact time of 600nullmin on further growth in contact time [107,130–137]. However, base-treated activated carbon showed a linear rise in the maximum adsorption capacity with increased contact time [130,138]. Moreover, acid/base treated activated carbon declined maximum adsorption capacity with increased contact time [125,139]. However, it could be interpreted that the effect of

contact time on the maximum adsorption capacity depends on whether the activated carbon is acid-treated or base treated, or a combination of both.

Fe-based nanocomposite showed a rapid increase in maximum adsorption capacity on increasing contact time [150–154]. Furthermore, Mn-based nanocomposite showed a rise in the maximum adsorption capacity with increased contact time [155,156]. Graphene-based nanocomposite showed increasing peaks of maximum adsorption capacity with increased contact time [150, 159–169]. So, it could be interpreted that the functional group or component attached to the nanocomposite significantly alters the effect of contact time on the maximum adsorption capacity.

PANI-based adsorbents showed multiple rise and decline peaks of maximum adsorption capacity with increased contact time. So, it could be interpreted that the functional group or component attached to the PANI-based adsorbents significantly alters the effect of contact time on the maximum adsorption capacity [154,185–188,190–195]. Overall, it could be stated that the effect of contact time on the maximum adsorption capacity of adsorbents depends on the type of adsorbent used, the component/functional group attached to the adsorbent, and chemical treatments (acid, base, the combination of acid/base) of adsorbents.

5.5. Effect of adsorbent dosage

The effect of adsorbent dosage on the maximum adsorption capacity of various types of adsorbents such as biosorbents (fruit waste, fungus, leaf, and biochar), activated carbon (acid-treated, base-treated, and acid/base-treated), nanocomposite (Fe-based, Mn-based, Cu-based, and graphene-based), and PANI are shown in Fig. 23 which is discussed in detail below:

The fruit waste and fungal biosorbents show a decline in maximum adsorption capacity with increased adsorbent dosage [106,112, 113,117–121]. Contrarily, the leaf biosorbents showed an exponential rise in the maximum adsorption capacity up to an adsorbent dosage of $5 \, g \, L^{-1}$ and a decline on further increase in adsorbent dosage [114,115,122–124]. However, biochar biosorbents show a little rise in maximum adsorption capacity with increased dosage [116,125]. Therefore, it could be interpreted that the effect of adsorbent dosage of bio sorbents depends on the type of biosorbent.

Acid-treated activated carbons show multiple rise and decline peaks of maximum adsorption capacity with increased adsorbent dosage [107,130–137]. However, base-treated activated carbon showed a linear decline in the maximum adsorption capacity with increased adsorbent dosage [130,138]. Moreover, acid/base treated activated carbon increased maximum adsorption capacity with increased adsorbent dosage [125,139]. However, it could be interpreted that the effect of adsorbent dosage on maximum adsorption capacity depends on the type of chemically treated activated carbon adsorbent, i.e., acid-treated activated carbon, base-treated activated carbon and acid/base-treated activated carbon.

Fe-based nanocomposite showed a rapid decline and then a rise and decline peak in maximum adsorption capacity on the increase in adsorbent dosage [150–154]. Furthermore, Mn-based nanocomposite showed a linear decline in the maximum adsorption capacity with increased adsorbent dosage [155,156]. Moreover, Cu-based nanocomposite adsorbent showed a linear increase in maximum adsorption capacity at a constant adsorbent dosage ($1.6 \, \text{nullg} \, L^{-1}$) [158]. Graphene-based nanocomposite adsorbent showed an increase and decline peaks till adsorbent dosage ($3 \, g \, L^{-1}$) and then a rapid rise in maximum adsorption capacity with an increase in adsorbent dosage [150,159–169]. So, it could be interpreted that the effect of the adsorbent dosage of the nanocomposite adsorbents on maximum adsorption capacity depends on the functional group or component attached to the nanocomposite adsorbent.

PANI-based adsorbents showed a decline in maximum adsorption capacity with increased adsorbent dosage. So, it could be interpreted that the PANI-based adsorbents show a higher maximum adsorption capacity of PANI-based adsorbents at less adsorbent dosage [154,185–188,190–195].

Therefore, it could be stated that the effect of adsorbent dosage on the maximum adsorption capacity of adsorbents depends on the type of adsorbent used and chemical treatments (acid, base, combination of acid/base) of adsorbents.

6. Chromium (VI) adsorption in industrial wastewater

Cr(VI) is an important naturally occurring metal widely used in various areas, including leather tanning, electroplating, petroleum refinery, metal finishing, mining, wood preservation, paint pigments, and textile [196]. Table 10 shows the Langmuir and Freundlich isotherm constants obtained for Cr(VI) adsorption for industrial wastewater treatment in the tannery, electroplating, and petroleum refinery using several adsorbents.

Several adsorbents have been used in Tannery industrial wastewater treatment for Cr(VI) adsorption, such as biosorbents (Tea waste [197] (Fig. 24 (a)), Syzygium cumini bark [198], corn cob [199], avocado kernel seeds (AKS) [200], Juniperus procera sawdust (JPS) [200], papaya peels (PP) [200], banana peel [201], orange (citrus cinensis) peel adsorbent [202], coconut Coirpith [203], banana waste (BW) [204], sugarcane bagasse (SCB) [204], sawdust (SD) [204], Phragmites Australis (PA) [204], teak sawdust [203], rice husks [203], and cactus [205]), biomass-derived activated carbons (H_3PO_4 treated rice husk (RH-AC) (Fig. 24 (b)) [206], H_3PO_4 treated potato peel (PP-AC) [206], charcoal activated carbon (AC) [204], and granular activated carbon [207]), nanocomposites (MNPs/rGO/PMMA nanocomposite [208], and GO-Fe_3O_4 [209]), and PANI (Fe_3O_4@PANI/IA magnetic nanocomposite [210]) as shown in Table 10.

Fig. 24 shows the Langmuir isotherm Cr(VI) removal model for Tannery industrial wastewater using different adsorbents.

Fig. 25 shows the Freundlich isotherm Cr(VI) removal model for Tannery industrial wastewater using different adsorbents.

It has been observed that the Syzygium cumini bark biosorbent showed the highest maximum adsorption capacity following Freundlich adsorption isotherm representing heterogeneous adsorption surfaces of Syzygium cumini bark biosorbent and multilayer adsorption of Cr(VI) on Syzygium cumini bark biosorbent as shown in Fig. 25 (a) among other biosorbents and biomass-derived

activated carbons, nanocomposite, and PANI-based adsorbents [198]. However, charcoal-activated carbon (AC) and Fe_3O_4@PANI/IA magnetic nanocomposite showed the highest adsorption capacities following Freundlich adsorption isotherms representing heterogeneous adsorption surfaces of charcoal-activated carbon (AC) and Fe_3O_4@PANI/IA magnetic nanocomposite and multilayer adsorption of Cr(VI) on charcoal activated carbon (AC) and Fe_3O_4@PANI/IA magnetic nanocomposite as shown in Fig. 25 (b-c) among other biomass-derived activated carbons and PANI-based adsorbents [204,210]. MNPs/rGO/PMMA nanocomposite showed the highest adsorption capacity following Langmuir adsorption isotherm representing homogeneous adsorption surfaces of MNPs/rGO/PMMA nanocomposite and mono-layer adsorption of Cr(VI) on MNPs/rGO/PMMA nanocomposite as shown in Fig. 25 (c) among other nanocomposites [208].

Several adsorbents have been used in Electroplating industrial wastewater treatment for Cr(VI) adsorption such as biosorbents (coconut coir pith [211], leechi (Litchi chinensis) fruit peel [212], walnut shell powder (Fig. 26 (a)) [212], powdered pistachio hull (PHP) [214], Aspergillus niger fungal biosorbent [215], Penicillium janthinellum fungal biosorbent [215], Aspergillus niger fungal biosorbent [216], Aspergillus niger fungal biosorbent [217], *P. orientalis* bark [218], and corn straw biochar (Fig. 27 (a)) [219]), biomass-derived activated carbons (HNO_3-treated *P. orientalis* bark activated carbon [218], H_2SO_4 treated Aspergillus niger fungal biosorbent [217], NaOH treated Aspergillus niger fungal biosorbent [217], NaOH treated corncob based activated (CAC) [220], KOH treated peanut shell based activated carbon (PAC) [221], magnetic KOH treated peanut shell based activated carbon (MPAC) [221], commercial activated carbon (CAC) (Fig. 26 (b) and Fig. 27 (b)) [221], commercial activated carbon based on coconut coir pith [211], and powdered activated carbon (PAC) [214]), and nanocomposites (thioacetamide (TAA) sulfur precursor based Bi_2S_3 nanostructures [222], L-cysteine (L-Cys) sulfur precursor based Bi_2S_3 nanostructures [222], amino-functionalized vermiculite-supported nanoscale zero-valent iron (AVT-nZVI) (Fig. 26 (c) and Fig. 27 (c)) [223], and γ-Fe_2O_3 nanoparticles [224]) as shown in Table 10.

Fig. 26 shows the Langmuir isotherm Cr(VI) removal model for Electroplating industrial wastewater using different adsorbents.

Fig. 27 shows the Freundlich isotherm Cr(VI) removal model for Electroplating industrial wastewater using different adsorbents.

It has been observed that the coconut coir pith biosorbent showed the highest adsorption capacity following Langmuir adsorption isotherm representing homogeneous adsorption surfaces of coconut coir pith biosorbent and mono-layer adsorption of Cr(VI) on coconut coir pith biosorbent among other biosorbents, biomass-derived activated carbons, and nanocomposites [211]. However, commercial activated carbon based on coconut coir pith and L-cysteine (L-Cys) sulfur precursor-based Bi2S3 nanostructures showed the highest adsorption capacities following Langmuir adsorption isotherms representing homogeneous adsorption surfaces of coconut coir pith and L-cysteine (L-Cys) sulfur precursor based Bi2S3 nanostructures and mono-layer adsorption of Cr(VI) on coconut coir pith and L-cysteine (L-Cys) sulfur precursor based Bi2S3 nanostructures among other biomass-derived activated carbons and nanocomposites adsorbents [211,222].

In the case of Cr(VI) adsorption in petroleum refinery wastewater treatment using nanocomposites, CdO-GO nanocomposites showed the highest adsorption capacity following Freundlich adsorption isotherm representing heterogeneous adsorption surfaces of CdO-GO nanocomposite and multilayer adsorption of Cr(VI) on CdO-GO nanocomposite [225] among other nanocomposites used such as G nanosheets [225], GO nanosheets [225], CdO NPs [225], G-CdO nanocomposite [225], and CdO-GO nanocomposites [225].

Overall, it can be concluded that the Tannery wastewater treatment for Cr(VI) adsorption using Syzygium cumini bark biosorbent resulted in the highest maximum adsorption capacity among other adsorbents and other sources of industrial wastewater due to the higher initial Cr(VI) concentration while following Freundlich adsorption isotherm and pseudo-second-order kinetic model indicating the multi-layer adsorption, Syzygium cumini bark biosorbent heterogeneity, and Cr(VI) chemisorption.

Table 11 shows the pseudo-first-order and pseudo-second-order kinetic model constants obtained for Cr(VI) adsorption for industrial wastewater treatment in the tannery, electroplating, and petroleum refinery using several adsorbents.

Several adsorbents have been used in Tannery industrial wastewater treatment for Cr(VI) adsorption, such as biosorbents (Tea waste [197], Syzygium cumini bark [198], corn cob [199], avocado kernel seeds (AKS) [200], Juniperus procera sawdust (JPS) [200], papaya peels (PP) [200], banana peel [201], orange (citrus cinensis) peel adsorbent [202], coconut Coirpith [203], banana waste (BW) [204], sugarcane bagasse (SCB) [204], sawdust (SD) [204], Phragmites Australis (PA) [204], teak sawdust [203], rice husks [203], and cactus [205]), biomass-derived activated carbons (H_3PO_4 treated rice husk (RH-AC) [206], H_3PO_4 treated potato peel (PP-AC) [206], charcoal activated carbon (AC) [204], and granular activated carbon [207]), nanocomposites (MNPs/rGO/PMMA nanocomposite [208], and GO-Fe_3O_4 [209]), and PANI (Fe_3O_4@PANI/IA magnetic nanocomposite [210]) as shown in Table 11.

Fig. 28 shows the Pseudo-first-order kinetic Cr(VI) removal model for Tannery industrial wastewater using different adsorbents.

Fig. 29 shows the Pseudo-second-order kinetic model of Cr(VI) removal for Tannery industrial wastewater using different adsorbents.

Several adsorbents have been used in Electroplating industrial wastewater treatment for Cr(VI) adsorption, such as biosorbents (leechi (Litchi chinensis) fruit peel [212], walnut shell powder [212], powdered pistachio hull (PHP) [214], Aspergillus niger fungal biosorbent [216], corn straw biochar [219], and Aspergillus niger (Fig. 30 (b)) [217]), biomass-derived activated carbons (H_2SO_4 treated Aspergillus niger (Fig. 30 (b)) [217], NaOH treated Aspergillus niger (Fig. 30 (b)) [217], NaOH treated corncob based activated (CAC) [220], KOH treated peanut shell based activated carbon (PAC) [221], Magnetic KOH treated peanut shell based activated carbon (MPAC) [221], powdered activated carbon (PAC) [214], and commercial activated carbon (CAC) [221]), and nanocomposites (amino-functionalized vermiculite-supported nanoscale zero-valent iron (AVT-nZVI) [223], and γ-Fe_2O_3 nanoparticles [224]) as shown in Table 11.

Fig. 30 shows the Pseudo-first-order kinetic model of Cr(VI) removal for Electroplating industrial wastewater using different adsorbents.

Fig. 31 shows the Pseudo-second-order kinetic model of Cr(VI) removal for Electroplating industrial wastewater using different adsorbents.

It has been observed that the corn straw biochar showed the highest calculated amounts of Cr(VI) adsorbed at equilibrium ($q^{I}_{e,cal}$, and $q^{II}_{e,cal}$), as shown in Fig. 30 (a) and Fig. 31 (a) among other biosorbents while following pseudo-second-order kinetic model indicating chemical sorption involving valence forces through sharing or exchange of electrons between the corn straw biochar and Cr (VI) [219]. However, magnetic KOH-treated peanut shell-based activated carbon (MPAC) showed the highest experimental and calculated amounts of Cr(VI) adsorbed at equilibrium ($q_{e,exp}$, and $q^{II}_{e,cal}$) among biosorbents, biomass-derived activated carbons, and nanocomposites as shown in Fig. 31 (b) [221]. However, the highest calculated amounts of Cr(VI) adsorbed at equilibrium by the pseudo-first-order kinetic model ($q^{I}_{e,cal}$) is shown by the Commercial Activated Carbon (CAC) among other activated carbons, biosorbents, and nanocomposites, while following pseudo-second-order kinetic model indicating chemical sorption between the CAC and Cr(VI) [221]. Amino-functionalized vermiculite-supported nanoscale zero-valent iron (AVT-nZVI) exhibited the highest calculated amounts of Cr(VI) adsorbed at equilibrium ($q^{II}_{e,cal}$) with an increase in initial Cr(VI) concentration among other nanocomposites while following pseudo-second-order kinetic model (Fig. 31 (c)) as compared to pseudo-first-order kinetic model (Fig. 30 (c)) indicating chemical sorption between the AVT-nZVI and Cr(VI) [223]. The lowest calculated amounts of Cr(VI) adsorbed at equilibrium by pseudo-first-order and pseudo-second-order kinetic models ($q^{I}_{e,cal}$, $q^{II}_{e,cal}$) is shown by the Leechi (Litchi chinensis) fruit peel among other biosorbents, activated carbons, and nanocomposites while following pseudo-first-order kinetic model indicating Cr(VI) adsorption using Leechi (Litchi chinensis) fruit peel is not chemisorption [212].

In the case of Cr(VI) adsorption in petroleum refinery wastewater treatment using nanocomposites, G-CdO nanocomposite showed the highest calculated amounts of Cr(VI) adsorbed at equilibrium by the pseudo-first-order kinetic model ($q^{I}_{e,cal}$) [225] as compared to other nanocomposites including CdO-GO [225], G nanosheets [225], GO nanosheets [225], CdO NPs [225], and CdO-GO nanocomposites [225]. However, the highest calculated amounts of Cr(VI) adsorbed at equilibrium by pseudo-second-order kinetic models ($q^{II}_{e,cal}$) is observed in CdO-GO nanocomposites, while following pseudo-second-order kinetic model indicating chemical sorption between the CdO-GO nanocomposite and Cr(VI) [225].

Overall, it can be concluded that the Petroleum refinery wastewater treatment for Cr(VI) adsorption using CdO-GO nanocomposites resulted in the highest calculated amounts of Cr(VI) adsorbed at equilibrium by the pseudo-second-order kinetic model ($q^{II}_{e,cal}$) among other adsorbents and other sources of industrial wastewater due to the higher initial Cr(VI) concentration while following pseudo-second-order kinetic model and Freundlich adsorption isotherm indicating the Cr(VI) chemisorption, multi-layer adsorption, and CdO-GO nanocomposites heterogeneity.

7. Conclusions

Heavy metals in wastewater are a severe concern for human and marine life. Hexavalent chromium in wastewater leads to various diseases, such as cancer, lung tumors, and allergies. Different adsorbents are being used to remove the hexavalent chromium from wastewater, such as biosorbents (fruit waste, leaves, fungus, and biochar), activated carbon (acid-treated, base treated, and acid/base treated), nanocomposites (Fe-based, Mn-based, Cu based, and graphene-based) and PANI. It is observed that the magnetic graphene oxide functionalized amino acid and PANI functionalized transition metal adsorbents have been found to have the highest Langmuir's maximum adsorption capacity. Furthermore, the magnetic graphene oxide functionalized amino acid has been found to have the highest experimental and pseudo-second-order kinetic model equilibrium adsorption capacities while following the multilayer adsorption and chemisorption. The highest heterogenous adsorption capacity is found in iron oxide functionalized calcium carbonate nanocomposites following mono-layer adsorption and chemisorption.

It is important to consider operational parameters such as initial Cr(VI) concentration, temperature, pH, contact time, and adsorbent dosage for optimal results in adsorption experiments. These operational parameters play a vital role in Langmuir's maximum adsorption capacity.

The Langmuir isotherm plays a significant role in determining the adsorption mechanism of the adsorbents by correlation co-efficients (R^2). It has been observed that the source of the adsorbent significantly highlights the monolayer and multilayer adsorption mechanisms. Several adsorbents showed monolayer adsorption, such as biosorbent, activated carbon adsorbent, nanocomposite, and PANI-based adsorbent.

Hexavalent chromium is an important naturally occurring metal extensively found in several industrial wastewaters, including leather tanning and electroplating. Tannery wastewater treatment for hexavalent chromium adsorption using syzygium cumini bark biosorbent has the highest Langmuir's maximum adsorption capacity among other adsorbents and other sources of industrial wastewaters due to the higher initial hexavalent chromium concentration, while following Freundlich adsorption isotherm and pseudo-second-order kinetic model indicating multi-layer adsorption, heterogeneity of syzygium cumini bark biosorbent, and chemisorption.

Funding

Author contribution statement

All authors listed have significantly contributed to the development and the writing of this article.

Data availability statement

Data will be made available on request.

Declaration of competing interest

The authors declare that they have no known competing financial interests or personal relationships that could have appeared to influence the work reported in this paper.

References

[1] S. Chowdhury, R. Balasubramanian, Recent advances in the use of graphene-family nanoadsorbents for removal of toxic pollutants from wastewater, Adv. Colloid Interface Sci. 204 (2014) 35–56, https://doi.org/10.1016/j.cis.2013.12.005.

[2] H. Wang, X. Yuan, Y. Wu, H. Huang, X. Peng, G. Zeng, H. Zhong, J. Liang, M. Ren, Graphene-based materials: fabrication, characterization and application for the decontamination of wastewater and wastegas and hydrogen storage/generation, Adv. Colloid Interface Sci. 195–196 (2013) 19–40, https://doi.org/10.1016/j.cis.2013.03.009.

[3] X. Li, K. Schneider, Control-flow guided clause generation for property directed reachability, in: 2016 IEEE Int. High Lev. Des. Valid. Test Work., 2016, pp. 17–24, https://doi.org/10.1109/HLDVT.2016.7748250.

[4] K.S. Rao, M. Mohapatra, S. Anand, P. Venkateswarlu, Review on cadmium removal from aqueous solutions, Int. J. Eng. Sci. Technol. 2 (2010).

[5] S.K. Gunatilake, Methods of removing heavy metals from industrial wastewater, Methods 1 (2015) 14.

[6] S. Mehdipour, V. Vatanpour, H.-R. Kariminia, Influence of ion interaction on lead removal by a polyamide nanofiltration membrane, Desalination 362 (2015) 84–92, https://doi.org/10.1016/j.desal.2015.01.030.

[7] M. Bhaumik, K. Setshedi, A. Maity, M.S. Onyango, Chromium(VI) removal from water using fixed bed column of polypyrrole/Fe3O4 nanocomposite, Sep. Purif. Technol. 110 (2013) 11–19, https://doi.org/10.1016/j.seppur.2013.02.037.

[8] N.H. Kera, M. Bhaumik, N. Ballav, K. Pillay, S.S. Ray, A. Maity, Selective removal of Cr(VI) from aqueous solution by polypyrrole/2,5-diaminobenzene sulfonic acid composite, J. Colloid Interface Sci. 476 (2016) 144–157, https://doi.org/10.1016/j.jcis.2016.05.011.

[9] H. Huang, X. Yuan, G. Zeng, H. Zhu, H. Li, Z. Liu, H. Jiang, L. Leng, W. Bi, Quantitative evaluation of heavy metals' pollution hazards in liquefaction residues of sewage sludge, Bioresour. Technol. 102 (2011) 10346–10351, https://doi.org/10.1016/j.biortech.2011.08.117.

[10] J. Belagyi, M. Pas, P. Raspor, M. Pesti, T. Páli, Effect of hexavalent chromium on eukaryotic plasma membrane studied by EPR spectroscopy, Biochim. Biophys. Acta Biomembr. 1421 (1999) 175–182.

[11] H. Oliveira, T.M. Santos, J. Ramalho-Santos, M. de Lourdes Pereira, Histopathological effects of hexavalent chromium in mouse kidney, Bull. Environ. Contam. Toxicol. 76 (2006) 977–983.

[12] K.K. Deepali, K. Gangwar, Metals concentration in textile and tannery effluents, associated soils and ground water, N. Sci. J 3 (2010) 82–89.

[13] E.O. Ugoji, O.O. Aboaba, Biological treatments of textile industrial effluents in Lagos metropolis, Nigeria, J. Environ. Biol. 25 (2004) 497–502.

[14] K. Gopalakrishnan, T. Jeyadoss, Comparative Study on Biosorption of Zn (II), Cu (II) and Cr (VI) from Textile Dye Effluent Using Activated Rice Husk and Activated Coconut Fibre, 2011.

[15] B. Saha, C. Orvig, Biosorbents for hexavalent chromium elimination from industrial and municipal effluents, Coord. Chem. Rev. 254 (2010) 2959–2972.

[16] A.P. Das, S. Mishra, Hexavalent chromium (VI): environment pollutant and health hazard, J. Environ. Res. Dev. 2 (2008) 386–392.

[17] J. Burger, M. Gochfeld, D. Kosson, C.W. Powers, B. Friedlander, J. Eichelberger, D. Barnes, L.K. Duffy, S.C. Jewett, C.D. Volz, Science, policy, and stakeholders: developing a consensus science plan for Amchitka Island, Aleutians, Alaska, Environ. Manag. 35 (2005) 557–568.

[18] S.S. Vutukuru, Acute effects of hexavalent chromium on survival, oxygen consumption, hematological parameters and some biochemical profiles of the Indian major carp, Labeo rohita, Int. J. Environ. Res. Publ. Health 2 (2005) 456–462.

[19] A.K. Mishra, B. Mohanty, Acute toxicity impacts of hexavalent chromium on behavior and histopathology of gill, kidney and liver of the freshwater fish, Channa punctatus (Bloch), Environ. Toxicol. Pharmacol. 26 (2008) 136–141.

[20] K. Salnikow, A. Zhitkovich, Genetic and epigenetic mechanisms in metal carcinogenesis and cocarcinogenesis: nickel, arsenic, and chromium, Chem. Res. Toxicol. 21 (2008) 28–44.

[21] S. Kawanishi, Y. Hiraku, M. Murata, S. Oikawa, The role of metals in site-specific DNA damage with reference to carcinogenesis, Free Radic. Biol. Med. 32 (2002) 822–832.

[22] R. Von Burg, D. Liu, Chromium and hexavalent chromium, J. Appl. Toxicol. 13 (1993) 225–230.

[23] K.C. Tagliari, R. Cecchini, J.A.V. Rocha, V.M.F. Vargas, Mutagenicity of sediment and biomarkers of oxidative stress in fish from aquatic environments under the influence of tanneries, Mutat. Res. Toxicol. Environ. Mutagen. 561 (2004) 101–117.

[24] M.K. Aroua, F.M. Zuki, N.M. Sulaiman, Removal of chromium ions from aqueous solutions by polymer-enhanced ultrafiltration, J. Hazard Mater. 147 (2007) 752–758, https://doi.org/10.1016/j.jhazmat.2007.01.120.

[25] M. Bhaumik, A. Maity, V. V Srinivasu, M.S. Onyango, Removal of hexavalent chromium from aqueous solution using polypyrrole-polyaniline nanofibers, Chem. Eng. J. 181–182 (2012) 323–333, https://doi.org/10.1016/j.cej.2011.11.088.

[26] I.A. for R. on Cancer, IARC monographs on the evaluation of carcinogenic risk of chemicals to man, Asbestos, IARC Monogr. Eval. Carcinog. Risk Chem. Man 14 (1977).

[27] J. Kotaś, Z. Stasicka, Chromium occurrence in the environment and methods of its speciation, Environ. Pollut. 107 (2000) 263–283, https://doi.org/10.1016/S0269-7491(99)00168-2.

[28] T. Mahmood, I.Z. Qureshi, M.S. Nadeem, M.A. Khan, Hexavalent chromium toxicity in pituitary and thyroid glands, Pakistan J. Zool. 40 (2008).

[29] W.H. Organization, Health criteria and other supporting information, Guidel. Drink. Qual. 2 (1996) 796–803. https://cir.nii.ac.jp/crid/1570009750921445760.bib?lang=en. (Accessed 6 March 2023).

[30] G.Z. Kyzas, K.A. Matis, Nanoadsorbents for pollutants removal: a review, J. Mol. Liq. 203 (2015) 159–168, https://doi.org/10.1016/j.molliq.2015.01.004.

[31] S. Wang, Y. Peng, Natural zeolites as effective adsorbents in water and wastewater treatment, Chem. Eng. J. 156 (2010) 11–24, https://doi.org/10.1016/j.cej.2009.10.029.

[32] X. Hu, J. Wang, Y. Liu, X. Li, G. Zeng, Z. Bao, X. Zeng, A. Chen, F. Long, Adsorption of chromium (VI) by ethylenediamine-modified cross-linked magnetic chitosan resin: isotherms, kinetics and thermodynamics, J. Hazard Mater. 185 (2011) 306–314, https://doi.org/10.1016/j.jhazmat.2010.09.034.

[33] X. Tan, Y. Liu, G. Zeng, X. Wang, X. Hu, Y. Gu, Z. Yang, Application of biochar for the removal of pollutants from aqueous solutions, Chemosphere 125 (2015) 70–85, https://doi.org/10.1016/j.chemosphere.2014.12.058.

[34] X. Tan, Y. Liu, Y. Gu, Y. Xu, G. Zeng, X. Hu, S. Liu, X. Wang, S. Liu, J. Li, Biochar-based nano-composites for the decontamination of wastewater: a review, Bioresour. Technol. 212 (2016) 318–333, https://doi.org/10.1016/j.biortech.2016.04.093.

[35] L. Hu, Z. Yang, L. Cui, Y. Li, H.H. Ngo, Y. Wang, Q. Wei, H. Ma, L. Yan, B. Du, Fabrication of hyperbranched polyamine functionalized graphene for high-efficiency removal of Pb(II) and methylene blue, Chem. Eng. J. 287 (2016) 545–556, https://doi.org/10.1016/j.cej.2015.11.059.

[36] C.J. Madadrang, H.Y. Kim, G. Gao, N. Wang, J. Zhu, H. Feng, M. Gorring, M.L. Kasner, S. Hou, Adsorption behavior of EDTA-graphene oxide for Pb (II) removal, ACS Appl. Mater. Interfaces 4 (2012) 1186–1193, https://doi.org/10.1021/am201645g.

[37] B. Volesky, Z.R. Holan, Biosorption of heavy metals, Biotechnol. Prog. 11 (1995) 235–250.

[38] H.S. Lee, B. Volesky, Interaction of light metals and protons with seaweed biosorbent, Water Res. 31 (1997) 3082–3088.

[39] D. Kratochvil, P. Pimentel, B. Volesky, Removal of trivalent and hexavalent chromium by seaweed biosorbent, Environ. Sci. Technol. 32 (1998) 2693–2698.

[40] D. Kratochvil, B. Volesky, Advances in the biosorption of heavy metals, Trends Biotechnol. 16 (1998) 291–300.

[41] M.C. Basso, E.G. Cerrella, A.L. Cukierman, Lignocellulosic materials as potential biosorbents of trace toxic metals from wastewater, Ind. Eng. Chem. Res. 41 (2002) 3580–3585.

[42] F. Pagnanelli, S. Mainelli, F. Vegliò, L. Toro, Heavy metal removal by olive pomace: biosorbent characterisation and equilibrium modelling, Chem. Eng. Sci. 58 (2003) 4709–4717.

[43] B. Volesky, Sorption and Biosorption, Montreal-St. Lambert, Quebec, vol. 11, Canada, BV Sorbex Inc., 2003, pp. 258–263.

[44] D. Park, Y.-S. Yun, J.H. Jo, J.M. Park, Biosorption process for treatment of electroplating wastewater containing Cr (VI): laboratory-scale feasibility test, Ind. Eng. Chem. Res. 45 (2006) 5059–5065.

[45] L.C. Maremeni, S.J. Modise, F.M. Mtunzi, M.J. Klink, V.E. Pakade, Adsorptive removal of hexavalent chromium by diphenylcarbazide-grafted Macadamia nutshell powder, Bioinorgan. Chem. Appl. 2018 (2018).

[46] S. Dawood, T.K. Sen, Removal of anionic dye Congo red from aqueous solution by raw pine and acid-treated pine cone powder as adsorbent: equilibrium, thermodynamic, kinetics, mechanism and process design, Water Res. 46 (2012) 1933–1946, https://doi.org/10.1016/j.watres.2012.01.009.

[47] M. Omidvar Borna, M. Pirsaheb, M. Vosoughi Niri, R. Khosravi Mashizie, B. Kakavandi, M.R. Zare, A. Asadi, Batch and column studies for the adsorption of chromium(VI) on low-cost Hibiscus Cannabinus kenaf, a green adsorbent, J. Taiwan Inst. Chem. Eng. 68 (2016) 80–89, https://doi.org/10.1016/j.jtice.2016.09.022.

[48] A.B. Albadarin, S. Solomon, T.A. Kurniawan, C. Mangwandi, G. Walker, Single, simultaneous and consecutive biosorption of Cr(VI) and Orange II onto chemically modified masau stones, J. Environ. Manag. 204 (2017) 365–374, https://doi.org/10.1016/j.jenvman.2017.08.042.

[49] C. Raji, T.S. Anirudhan, Batch Cr(VI) removal by polyacrylamide-grafted sawdust: kinetics and thermodynamics, Water Res. 32 (1998) 3772–3780, https://doi.org/10.1016/S0043-1354(98)00150-X.

[50] N. Nasseh, L. Taghavi, B. Barikbin, A.R. Harifi-Mood, The removal of Cr(VI) from aqueous solution by almond green hull waste material: kinetic and equilibrium studies, J. Water Reuse Desalin. 7 (2016) 449–460, https://doi.org/10.2166/wrd.2016.047.

[51] E. Rosales, J. Meijide, T. Tavares, M. Pazos, M.A. Sanromán, Grapefruit peelings as a promising biosorbent for the removal of leather dyes and hexavalent chromium, Process Saf. Environ. Protect. 101 (2016) 61–71, https://doi.org/10.1016/j.psep.2016.03.006.

[52] N.M. Rane, S. V Admane, R.S. Sapkal, in: S.K. Ghosh (Ed.), Adsorption of Hexavalent Chromium from Wastewater by Using Sweetlime and Lemon Peel Powder by Batch Studies BT - Waste Management and Resource Efficiency, Springer Singapore, Singapore, 2019, pp. 1207–1220.

[53] P. Suksabye, P. Thiravetyan, Cr(VI) adsorption from electroplating plating wastewater by chemically modified coir pith, J. Environ. Manag. 102 (2012) 1–8, https://doi.org/10.1016/j.jenvman.2011.10.020.

[54] D. Park, Y.-S. Yun, J. Hye Jo, J.M. Park, Mechanism of hexavalent chromium removal by dead fungal biomass of Aspergillus Niger, Water Res. 39 (2005) 533–540, https://doi.org/10.1016/j.watres.2004.11.002.

[55] P. Chingombe, B. Saha, R.J. Wakeman, Surface modification and characterisation of a coal-based activated carbon, Carbon N. Y. 43 (2005) 3132–3143.

[56] G. Qin, M.J. McGuire, N.K. Blute, C. Seidel, L. Fong, Hexavalent chromium removal by reduction with ferrous sulfate, coagulation, and filtration: a pilot-scale study, Environ. Sci. Technol. 39 (2005) 6321–6327, https://doi.org/10.1021/es050486p.

[57] A. Kumar, H.M. Jena, Adsorption of Cr(VI) from aqueous solution by prepared high surface area activated carbon from Fox nutshell by chemical activation with H3PO4, J. Environ. Chem. Eng. 5 (2017) 2032–2041, https://doi.org/10.1016/j.jece.2017.03.035.

[58] K.M. Doke, E.M. Khan, Equilibrium, kinetic and diffusion mechanism of Cr(VI) adsorption onto activated carbon derived from wood apple shell, Arab. J. Chem. 10 (2017), https://doi.org/10.1016/j.arabjc.2012.07.031. S252–S260.

[59] M.K. Rai, G. Shahi, V. Meena, R. Meena, S. Chakraborty, R.S. Singh, B.N. Rai, Removal of hexavalent chromium Cr (VI) using activated carbon prepared from mango kernel activated with H3PO4, Resour. Technol. 2 (2016), https://doi.org/10.1016/j.reffit.2016.11.011. S63–S70.

[60] C.A. Demarchi, B.S. Michel, N. Nedelko, A. Ślawska-Waniewska, P. Dłużewski, A. Kaleta, R. Minikayev, T. Strachowski, L. Lipińska, J. Dal Magro, C. A. Rodrigues, Preparation, characterization, and application of magnetic activated carbon from termite feces for the adsorption of Cr(VI) from aqueous solutions, Powder Technol. 354 (2019) 432–441, https://doi.org/10.1016/j.powtec.2019.06.020.

[61] J.C. Almeida, C.E.D. Cardoso, D.S. Tavares, R. Freitas, T. Trindade, C. Vale, E. Pereira, Chromium removal from contaminated waters using nanomaterials – a review, TrAC, Trends Anal. Chem. 118 (2019) 277–291, https://doi.org/10.1016/j.trac.2019.05.005.

[62] S. Kalidhasan, M. Ganesh, S. Sricharan, N. Rajesh, Extractive separation and determination of chromium in tannery effluents and electroplating waste water using tribenzylamine as the extractant, J. Hazard Mater. 165 (2009) 886–892.

[63] A. Senol, Amine extraction of chromium (VI) from aqueous acidic solutions, Sep. Purif. Technol. 36 (2004) 63–75.

[64] H.H. Someda, E.A. El-Shazly, R.R. Sheha, The role of some compounds on extraction of chromium (VI) by amine extractants, J. Hazard Mater. 117 (2005) 213–219.

[65] S. Kalidhasan, S. Sricharan, M. Ganesh, N. Rajesh, Liquid– liquid extraction of chromium (VI) with tricaprylmethylammonium chloride using isoamylalcohol as the diluent and its application to industrial effluents, J. Chem. Eng. Data 55 (2010) 5627–5633.

[66] P. Venkateswaran, K. Palanivelu, Solvent extraction of hexavalent chromium with tetrabutyl ammonium bromide from aqueous solution, Sep. Purif. Technol. 40 (2004) 279–284.

[67] A. Suresh, C.V.S.B. Rao, B. Srinivasulu, N.L. Sreenivasan, S. Subramaniam, K.N. Sabharwal, N. Sivaraman, T.G. Srinivasan, R. Natarajan, P.R.V. Rao, Development of alternate extractants for separation of actinides, Energy Proc. 39 (2013) 120–126.

[68] W.S.W. Ngah, M.A.K.M. Hanafiah, Removal of heavy metal ions from wastewater by chemically modified plant wastes as adsorbents: a review, Bioresour. Technol. 99 (2008) 3935–3948.

[69] A. Leudjo Taka, K. Pillay, X. Yangkou Mbianda, Nanosponge cyclodextrin polyurethanes and their modification with nanomaterials for the removal of pollutants from waste water: a review, Carbohydr. Polym. 159 (2017) 94–107, https://doi.org/10.1016/j.carbpol.2016.12.027.

[70] H.A. Alalwan, M.A. Kadhom, A.H. Alminshid, Removal of heavy metals from wastewater using agricultural byproducts, J. Water Supply Res. Technol. - Aqua 69 (2020) 99–112, https://doi.org/10.2166/aqua.2020.133.

[71] S. Sharma, S. Tiwari, A. Hasan, V. Saxena, L.M. Pandey, Recent advances in conventional and contemporary methods for remediation of heavy metal-contaminated soils, 3 Biotech 8 (2018) 1–18, https://doi.org/10.1007/s13205-018-1237-8.

[72] Z. Song, W. Li, W. Liu, Y. Yang, N. Wang, H. Wang, H. Gao, Novel magnetic lignin composite sorbent for chromium (VI) adsorption, RSC Adv. 5 (2015) 13028–13035.

[73] J. Zhang, T. Shang, X. Jin, J. Gao, Q. Zhao, Study of chromium (VI) removal from aqueous solution using nitrogen-enriched activated carbon based bamboo processing residues, RSC Adv. 5 (2015) 784–790.

[74] S.R.J. Oliver, Cationic inorganic materials for anionic pollutant trapping and catalysis, Chem. Soc. Rev. 38 (2009) 1868–1881.

[75] S. Babel, T.A. Kurniawan, Low-cost adsorbents for heavy metals uptake from contaminated water: a review, J. Hazard Mater. 97 (2003) 219–243.

[76] K. Mesuere, W. Fish, Chromate and oxalate adsorption on goethite. 1. Calibration of surface complexation models, Environ. Sci. Technol. 26 (1992) 2357–2364.

[77] E. Vasileva, K. Hadjiivanov, P. Mandjukov, Adsorption of Cr6+ oxo anions on pure and peroxide-modified TiO2 (anatase), Colloids Surfaces A Physicochem. Eng. Asp. 90 (1994) 9–15.

[78] S.-H. Huang, D.-H. Chen, Rapid removal of heavy metal cations and anions from aqueous solutions by an amino-functionalized magnetic nano-adsorbent, J. Hazard Mater. 163 (2009) 174–179, https://doi.org/10.1016/j.jhazmat.2008.06.075.

[79] R. Karthik, S. Meenakshi, Synthesis, characterization and Cr(VI) uptake study of polyaniline coated chitin, Int. J. Biol. Macromol. 72 (2015) 235–242, https://doi.org/10.1016/j.ijbiomac.2014.08.022.

[80] M.R. Muthumareeswaran, M. Alhoshan, G.P. Agarwal, Ultrafiltration membrane for effective removal of chromium ions from potable water, Sci. Rep. 7 (2017) 1–12.

[81] M. Owlad, M.K. Aroua, W.A.W. Daud, S. Baroutian, Removal of hexavalent chromium-contaminated water and wastewater: a review, water, Air. Soil Pollut. 200 (2009) 59–77, https://doi.org/10.1007/s11270-008-9893-7.

[82] E. Punrat, C. Maksuk, S. Chuanuwatanakul, W. Wonsawat, O. Chailapakul, Polyaniline/graphene quantum dot-modified screen-printed carbon electrode for the rapid determination of Cr(VI) using stopped-flow analysis coupled with voltammetric technique, Talanta 150 (2016) 198–205, https://doi.org/10.1016/j.talanta.2015.12.016.

[83] S. Debnath, A. Maity, K. Pillay, Magnetic chitosan–GO nanocomposite: synthesis, characterization and batch adsorber design for Cr(VI) removal, J. Environ. Chem. Eng. 2 (2014) 963–973, https://doi.org/10.1016/j.jece.2014.03.012.

[84] G.Z. Kyzas, D.N. Bikiaris, M. Seredych, T.J. Bandosz, E.A. Deliyanni, Removal of dorzolamide from biomedical wastewaters with adsorption onto graphite oxide/poly(acrylic acid) grafted chitosan nanocomposite, Bioresour. Technol. 152 (2014) 399–406, https://doi.org/10.1016/j.biortech.2013.11.046.

[85] Z.-F. Liu, G.-M. Zeng, H. Zhong, X.-Z. Yuan, L. Jiang, H.-Y. Fu, X. Ma, J.-C. Zhang, Effect of saponins on cell surface properties of Penicillium simplicissimum: performance on adsorption of cadmium(II), Colloids Surf. B Biointerfaces 86 (2011) 364–369, https://doi.org/10.1016/j.colsurfb.2011.04.021.

[86] B. Shao, Z. Liu, H. Zhong, G. Zeng, G. Liu, M. Yu, Y. Liu, X. Yang, Z. Li, Z. Fang, J. Zhang, C. Zhao, Effects of rhamnolipids on microorganism characteristics and applications in composting: a review, Microbiol. Res. 200 (2017) 33–44, https://doi.org/10.1016/j.micres.2017.04.005.

[87] X. Xue, J. Xu, S.A. Baig, X. Xu, Synthesis of graphene oxide nanosheets for the removal of Cd(II) ions from acidic aqueous solutions, J. Taiwan Inst. Chem. Eng. 59 (2016) 365–372, https://doi.org/10.1016/j.jtice.2015.08.019.

[88] E. Repo, J.K. Warchoł, A. Bhatnagar, A. Mudhoo, M. Sillanpää, Aminopolycarboxylic acid functionalized adsorbents for heavy metals removal from water, Water Res. 47 (2013) 4812–4832, https://doi.org/10.1016/j.watres.2013.06.020.

[89] X. Li, W. Cao, Y. Liu, G. Zeng, W. Zeng, L. Qin, T. Li, Property variation of magnetic mesoporous carbon modified by aminated hollow magnetic nanospheres: synthesis, characterization, and sorption, ACS Sustain. Chem. Eng. 5 (2017) 179–188.

[90] F. Fu, Q. Wang, Removal of heavy metal ions from wastewaters: a review, J. Environ. Manag. 92 (2011) 407–418, https://doi.org/10.1016/j.jenvman.2010.11.011.

[91] Z. Liu, Z. Zeng, Z. Zeng, G. Li, H. Zhong, X. Yuan, Y. Liu, J. Zhang, M. Chen, Y. Liu, G. Xie, Influence of rhamnolipids and Triton X-100 on adsorption of phenol by Penicillium simplicissimum, Bioresour. Technol. 110 (2012) 468–473, https://doi.org/10.1016/j.biortech.2012.01.092.

[92] Z. Liu, M. Yu, G. Zeng, M. Li, J. Zhang, H. Zhong, Y. Liu, B. Shao, Z. Li, Z. Zhang, G. Liu, X. Yang, Investigation on the reaction of phenolic pollution to mono-rhamnolipid micelles using MEUF, Environ. Sci. Pollut. Res. 24 (2017) 1230–1240, https://doi.org/10.1007/s11356-016-7851-2.

[93] D. Mohan, C.U. Pittman, Activated carbons and low cost adsorbents for remediation of tri- and hexavalent chromium from water, J. Hazard Mater. 137 (2006) 762–811, https://doi.org/10.1016/j.jhazmat.2006.06.060.

[94] S. Agrawal, N.B. Singh, Removal of toxic hexavalent chromium from aqueous solution by nickel ferrite-polyaniline nanocomposite, Desalination Water Treat. 57 (2016) 17757–17766, https://doi.org/10.1080/19443994.2015.1086700.

[95] J. Chen, X. Hong, Y. Zhao, Y. Xia, D. Li, Q. Zhang, Preparation of flake-like polyaniline/montmorillonite nanocomposites and their application for removal of Cr(VI) ions in aqueous solution, J. Mater. Sci. 48 (2013) 7708–7717, https://doi.org/10.1007/s10853-013-7591-3.

[96] N. Fellenz, F.J. Perez-Alonso, P.P. Martin, J.L. García-Fierro, J.F. Bengoa, S.G. Marchetti, S. Rojas, Chromium (VI) removal from water by means of adsorption-reduction at the surface of amino-functionalized MCM-41 sorbents, Microporous Mesoporous Mater. 239 (2017) 138–146, https://doi.org/10.1016/j.micromeso.2016.10.012.

[97] J.N. Sahu, J. Acharya, B.C. Meikap, Response surface modeling and optimization of chromium(VI) removal from aqueous solution using Tamarind wood activated carbon in batch process, J. Hazard Mater. 172 (2009) 818–825, https://doi.org/10.1016/j.jhazmat.2009.07.075.

[98] N. Ilankoon, Use of iron oxide magnetic nanosorbents for Cr (VI) removal from aqueous solutions: a review, J. Eng. Res. Appl. 4 (2014) 55–63.

[99] M.S. El-Geundi, Homogeneous surface diffusion model for the adsorption of basic dyestuffs onto natural clay in batch adsorbers, Adsorpt. Sci. Technol. 8 (1991) 217–225.

[100] F. Gimbert, N. Morin-Crini, F. Renault, P.-M. Badot, G. Crini, Adsorption isotherm models for dye removal by cationized starch-based material in a single component system: error analysis, J. Hazard Mater. 157 (2008) 34–46.

[101] G. Özsin, M. Kılıç, E. Apaydın-Varol, A.E. Pütün, Chemically activated carbon production from agricultural waste of chickpea and its application for heavy metal adsorption: equilibrium, kinetic, and thermodynamic studies, Appl. Water Sci. 9 (2019) 56, https://doi.org/10.1007/s13201-019-0942-8.

[102] I. Langmuir, The constitution and fundamental properties of solids and liquids. II. Liquids, J. Am. Chem. Soc. 39 (1917) 1848–1906.

[103] I. Langmuir, The adsorption of gases on plane surfaces of glass, mica and platinum, J. Am. Chem. Soc. 40 (1918) 1361–1403.

[104] N. Ayawei, S.S. Angaye, D. Wankasi, E.D. Dikio, Synthesis, characterization and application of Mg/Al layered double hydroxide for the degradation of Congo red in aqueous solution, Open J. Phys. Chem. 5 (2015) 56.

[105] N. Ayawei, A.T. Ekubo, D. Wankasi, E.D. Dikio, Adsorption of Congo red by Ni/Al-CO3: equilibrium, thermodynamic and kinetic studies, Orient, J. Chem. 31 (2015) 1307.

[106] M.T. Garza-González, J.E. Ramírez-Vázquez, M.D.L.Á. García-Hernández, M.E. Cantú-Cárdenas, A. Liñan-Montes, J.F. Villarreal-Chiu, Reduction of chromium (VI) from aqueous solution by biomass of *Cladosporium cladosporioides*, Water Sci. Technol. 76 (2017) 2494–2502, https://doi.org/10.2166/wst.2017.427.

[107] I.H. Ali, M.K. Al Mesfer, M.I. Khan, M. Danish, M.M. Alghamdi, Exploring adsorption process of lead (II) and chromium (VI) ions from aqueous solutions on acid activated carbon prepared from Juniperus procera leaves, Processes 7 (2019), https://doi.org/10.3390/pr7040217.

[108] K.A. Shroff, V.K. Vaidya, Kinetics and equilibrium studies on biosorption of nickel from aqueous solution by dead fungal biomass of Mucor hiemalis, Chem. Eng. J. 171 (2011) 1234–1245, https://doi.org/10.1016/j.cej.2011.05.034.

[109] H. Qiu, L. Lv, B. Pan, Q. Zhang, W. Zhang, Q. Zhang, Critical review in adsorption kinetic models, J. Zhejiang Univ. A. 10 (2009) 716–724, https://doi.org/10.1631/jzus.A0820524.

[110] D. Kučić, I. Ćosić, M. Vuković, F. Briški, Sorption kinetic studies of ammonium from aqueous solution on different inorganic and organic media, Acta Chim. Slov. 60 (No 1) (2013). https://journals.matheo.si/index.php/ACSi/article/view/24.

[111] S. Yadav, V. Srivastava, S. Banerjee, C.-H. Weng, Y.C. Sharma, Adsorption characteristics of modified sand for the removal of hexavalent chromium ions from aqueous solutions: kinetic, thermodynamic and equilibrium studies, Catena 100 (2013) 120–127, https://doi.org/10.1016/j.catena.2012.08.002.

[112] M. Akram, H.N. Bhatti, M. Iqbal, S. Noreen, S. Sadaf, Biocomposite efficiency for Cr(VI) adsorption: kinetic, equilibrium and thermodynamics studies, J. Environ. Chem. Eng. 5 (2017) 400–411, https://doi.org/10.1016/j.jece.2016.12.002.

[113] B. Dhal, Abhilash, B.D. Pandey, Mechanism elucidation and adsorbent characterization for removal of Cr(VI) by native fungal adsorbent, Sustain. Environ. Res. 28 (2018) 289–297, https://doi.org/10.1016/j.serj.2018.05.002.

[114] S. E, S.N.C. Patra, L.A. Varghese, S. N, Biosorption potential of Gliricidia sepium leaf powder to sequester hexavalent chromium from synthetic aqueous solution, J. Environ. Chem. Eng. 7 (2019), 103112, https://doi.org/10.1016/j.jece.2019.103112.

[115] A. Sharma, K.G. Bhattacharyya, Adsorption of chromium (VI) on Azadirachta Indica (neem) leaf powder, Adsorption 10 (2005) 327–338, https://doi.org/10.1007/s10450-005-4818-x.

[116] D. Mohan, S. Rajput, V.K. Singh, P.H. Steele, C.U. Pittman, Modeling and evaluation of chromium remediation from water using low cost bio-char, a green adsorbent, J. Hazard Mater. 188 (2011) 319–333, https://doi.org/10.1016/j.jhazmat.2011.01.127.

[117] S. Rafiaee, M.R. Samani, D. Toghraie, Removal of hexavalent chromium from aqueous media using pomegranate peels modified by polymeric coatings: effects of various composite synthesis parameters, Synth. Met. 265 (2020), https://doi.org/10.1016/j.synthmet.2020.116416.

[118] D. Kucic, M. Simonic, L. Furac, Batch adsorption of Cr(VI) ions on zeolite and agroindustrial waste, Chem. Biochem. Eng. Q. 31 (2018) 497–507, https://doi.org/10.15255/CABEQ.2017.1100.

[119] M.A. Espinoza-Sánchez, K. Arévalo-Niño, I. Quintero-Zapata, I. Castro-González, V. Almaguer-Cantú, Cr(VI) adsorption from aqueous solution by fungal bioremediation based using Rhizopus sp, J. Environ. Manag. 251 (2019), 109595, https://doi.org/10.1016/j.jenvman.2019.109595.

[120] S. Pourkarim, F. Ostovar, M. Mahdavianpour, M. Moslemzadeh, Adsorption of chromium(VI) from aqueous solution by Artist's Bracket fungi, Separ. Sci. Technol. 52 (2017) 1733–1741, https://doi.org/10.1080/01496395.2017.1299179.

[121] R. Majumder, L. Sheikh, A. Naskar, Vineeta, M. Mukherjee, S. Tripathy, Depletion of Cr(VI) from aqueous solution by heat dried biomass of a newly isolated fungus Arthrinium malaysianum: a mechanistic approach, Sci. Rep. 7 (2017), 11254, https://doi.org/10.1038/s41598-017-10160-0.

[122] S. Kuppusamy, P. Thavamani, M. Megharaj, K. Venkateswarlu, Y.B. Lee, R. Naidu, Potential of Melaleuca diosmifolia leaf as a low-cost adsorbent for hexavalent chromium removal from contaminated water bodies, Process Saf. Environ. Protect. 100 (2016) 173–182, https://doi.org/10.1016/j. psep.2016.01.009.

[123] N.K. Mondal, A. Samanta, P. Roy, B. Das, Optimization study of adsorption parameters for removal of Cr(VI) using Magnolia leaf biomass by response surface methodology, Sustain. Water Resour. Manag. 5 (2019) 1627–1639, https://doi.org/10.1007/s40899-019-00322-5.

[124] T. Sathish, N. V Vinithkumar, G. Dharani, R. Kirubagaran, Efficacy of mangrove leaf powder for bioremediation of chromium (VI) from aqueous solutions: kinetic and thermodynamic evaluation, Appl. Water Sci. 5 (2015) 153–160, https://doi.org/10.1007/s13201-014-0174-x.

[125] H. Deveci, Y. Kar, Adsorption of hexavalent chromium from aqueous solutions by bio-chars obtained during biomass pyrolysis, J. Ind. Eng. Chem. 19 (2013) 190–196, https://doi.org/10.1016/j.jiec.2012.08.001.

[126] A. Jusoh, L. Su Shiung, N. Ali, M.J.M.M. Noor, A simulation study of the removal efficiency of granular activated carbon on cadmium and lead, Desalination 206 (2007) 9–16, https://doi.org/10.1016/j.desal.2006.04.048.

[127] K.C. Kang, S.S. Kim, J.W. Choi, S.H. Kwon, Sorption of Cu2+ and Cd2+ onto acid- and base-pretreated granular activated carbon and activated carbon fiber samples, J. Ind. Eng. Chem. 14 (2008) 131–135, https://doi.org/10.1016/j.jiec.2007.08.007.

[128] O. Ioannidou, A. Zabaniotou, Agricultural residues as precursors for activated carbon production—a review, Renew. Sustain. Energy Rev. 11 (2007) 1966–2005, https://doi.org/10.1016/j.rser.2006.03.013.

[129] V.E. Pakade, N.T. Tavengwa, L.M. Madikizela, Recent advances in hexavalent chromium removal from aqueous solutions by adsorptive methods, RSC Adv. 9 (2019) 26142–26164.

[130] Y. Ma, W.J. Liu, N. Zhang, Y.S. Li, H. Jiang, G.P. Sheng, Polyethylenimine modified biochar adsorbent for hexavalent chromium removal from the aqueous solution, Bioresour. Technol. 169 (2014) 403–408, https://doi.org/10.1016/j.biortech.2014.07.014.

[131] A. Verma, S. Chakraborty, J.K. Basu, Adsorption study of hexavalent chromium using tamarind hull-based adsorbents, Sep. Purif. Technol. 50 (2006) 336–341, https://doi.org/10.1016/j.seppur.2005.12.007.

[132] K. Malwade, D. Lataye, V. Mhaisalkar, S. Kurwadkar, D. Ramirez, Adsorption of hexavalent chromium onto activated carbon derived from Leucaena leucocephala waste sawdust: kinetics, equilibrium and thermodynamics, Int. J. Environ. Sci. Technol. 13 (2016) 2107–2116, https://doi.org/10.1007/s13762-016-1042-z.

[133] I.H. Ali, H.A. Alrafai, Kinetic, isotherm and thermodynamic studies on biosorption of chromium(VI) by using activated carbon from leaves of Ficus nitida, Chem. Cent. J. 10 (2016) 1–7, https://doi.org/10.1186/S13065-016-0180-1.

[134] J. Anandkumar, B. Mandal, Adsorption of chromium(VI) and Rhodamine B by surface modified tannery waste: kinetic, mechanistic and thermodynamic studies, J. Hazard Mater. 186 (2011) 1088–1096, https://doi.org/10.1016/j.jhazmat.2010.11.104.

[135] M. Jain, V.K. Garg, K. Kadirvelu, Adsorption of hexavalent chromium from aqueous medium onto carbonaceous adsorbents prepared from waste biomass, J. Environ. Manag. 91 (2010) 949–957, https://doi.org/10.1016/j.jenvman.2009.12.002.

[136] J. Anandkumar, B. Mandal, Removal of Cr(VI) from aqueous solution using Bael fruit (Aegle marmelos correa) shell as an adsorbent, J. Hazard Mater. 168 (2009) 633–640, https://doi.org/10.1016/j.jhazmat.2009.02.136.

[137] S. Gupta, B. V Babu, Adsorption of chromium (VI) by a low-cost adsorbent prepared from tamarind seeds (n.d.) 1–6, http://discovery.bits-pilani.ac.in/~bvbabu/AD_SG_BVB_Chemcon-2006_FullPaper.pdf.

[138] G. Özsin, M. Kılıç, E. Apaydın-Varol, A.E. Pütün, Chemically activated carbon production from agricultural waste of chickpea and its application for heavy metal adsorption: equilibrium, kinetic, and thermodynamic studies, Appl. Water Sci. 9 (2019), https://doi.org/10.1007/s13201-019-0942-8.

[139] M. Chaudhuri, N.K. Bin Azizan, Adsorptive removal of chromium(VI) from aqueous solution by an agricultural waste-based activated carbon, Water Air Soil Pollut. 223 (2012) 1765–1771, https://doi.org/10.1007/s11270-011-0981-8.

[140] U.O. Aigbe, R. Das, W.H. Ho, V. Srinivasu, A. Maity, A novel method for removal of Cr(VI) using polypyrrole magnetic nanocomposite in the presence of unsteady magnetic fields, Sep. Purif. Technol. 194 (2018) 377–387, https://doi.org/10.1016/j.seppur.2017.11.057.

[141] R. Nithya, T. Gomathi, P.N. Sudha, J. Venkatesan, S. Anil, S.-K. Kim, Removal of Cr(VI) from aqueous solution using chitosan-g-poly(butyl acrylate)/silica gel nanocomposite, Int. J. Biol. Macromol. 87 (2016) 545–554, https://doi.org/10.1016/j.ijbiomac.2016.02.076.

[142] V. Sureshkumar, S.C.G. Kiruba Daniel, K. Ruckmani, M. Sivakumar, Fabrication of chitosan–magnetite nanocomposite strip for chromium removal, Appl. Nanosci. 6 (2016) 277–285, https://doi.org/10.1007/s13204-015-0429-3.

[143] H. Zhu, S. Jia, T. Wan, Y. Jia, H. Yang, J. Li, L. Yan, C. Zhong, Biosynthesis of spherical Fe3O4/bacterial cellulose nanocomposites as adsorbents for heavy metal ions, Carbohydr. Polym. 86 (2011) 1558–1564, https://doi.org/10.1016/j.carbpol.2011.06.061.

[144] S.-J. Wu, T.-H. Liou, F.-L. Mi, Synthesis of zero-valent copper–chitosan nanocomposites and their application for treatment of hexavalent chromium, Bioresour. Technol. 100 (2009) 4348–4353, https://doi.org/10.1016/j.biortech.2009.04.013.

[145] L. Leng, X. Yuan, G. Zeng, J. Shao, X. Chen, Z. Wu, H. Wang, X. Peng, Surface characterization of rice husk bio-char produced by liquefaction and application for cationic dye (Malachite green) adsorption, Fuel 155 (2015) 77–85, https://doi.org/10.1016/j.fuel.2015.04.019.

[146] D.-L. Huang, G.-M. Zeng, C.-L. Feng, S. Hu, X.-Y. Jiang, L. Tang, F.-F. Su, Y. Zhang, W. Zeng, H.-L. Liu, Degradation of lead-contaminated lignocellulosic waste by phanerochaete chrysosporium and the reduction of lead toxicity, Environ. Sci. Technol. 42 (2008) 4946–4951, https://doi.org/10.1021/es800072c.

[147] P.O. Boamah, Y. Huang, M. Hua, Q. Zhang, J. Wu, J. Onumah, L.K. Sam-Amoah, P.O. Boamah, Sorption of heavy metal ions onto carboxylate chitosan derivatives—a mini-review, Ecotoxicol. Environ. Saf. 116 (2015) 113–120, https://doi.org/10.1016/j.ecoenv.2015.01.012.

[148] R. Karthik, S. Meenakshi, Removal of Pb(II) and Cd(II) ions from aqueous solution using polyaniline grafted chitosan, Chem. Eng. J. 263 (2015) 168–177, https://doi.org/10.1016/j.cej.2014.11.015.

[149] Y.-Z. Long, M.-M. Li, C. Gu, M. Wan, J.-L. Duvail, Z. Liu, Z. Fan, Recent advances in synthesis, physical properties and applications of conducting polymer nanotubes and nanofibers, Prog. Polym. Sci. 36 (2011) 1415–1442, https://doi.org/10.1016/j.progpolymsci.2011.04.001.

[150] N. Subedi, A. Lähde, E. Abu-Danso, J. Iqbal, A. Bhatnagar, A comparative study of magnetic chitosan (Chi@Fe3O4) and graphene oxide modified magnetic chitosan (Chi@Fe3O4GO) nanocomposites for efficient removal of Cr(VI) from water, Int. J. Biol. Macromol. 137 (2019) 948–959, https://doi.org/10.1016/j.ijbiomac.2019.06.151.

[151] R. Khosravi, G. Moussavi, M.T. Ghaneian, M.H. Ehrampoush, B. Barikbin, A.A. Ebrahimi, G. Sharifzadeh, Chromium adsorption from aqueous solution using novel green nanocomposite: adsorbent characterization, isotherm, kinetic and thermodynamic investigation, J. Mol. Liq. 256 (2018) 163–174, https://doi.org/10.1016/j.molliq.2018.02.033.

[152] M.S. Islam, W.S. Choi, B. Nam, C. Yoon, H.J. Lee, Needle-like iron oxide@CaCO3 adsorbents for ultrafast removal of anionic and cationic heavy metal ions, Chem. Eng. J. 307 (2017) 208–219, https://doi.org/10.1016/j.cej.2016.08.079.

[153] X. Lv, J. Xu, G. Jiang, J. Tang, X. Xu, Highly active nanoscale zero-valent iron (nZVI)-Fe 3O 4 nanocomposites for the removal of chromium(VI) from aqueous solutions, J. Colloid Interface Sci. 369 (2012) 460–469, https://doi.org/10.1016/j.jcis.2011.11.049.

[154] A.E. Chávez-Guajardo, J.C. Medina-Llamas, L. Maqueira, C.A.S. Andrade, K.G.B. Alves, C.P. de Melo, Efficient removal of Cr (VI) and Cu (II) ions from aqueous media by use of polypyrrole/maghemite and polyaniline/maghemite magnetic nanocomposites, Chem. Eng. J. 281 (2015) 826–836, https://doi.org/10.1016/j.cej.2015.07.008.

[155] K.L. Bhowmik, A. Debnath, R.K. Nath, B. Saha, Synthesis of MnFe2O4 and Mn3O4 magnetic nano-composites with enhanced properties for adsorption of Cr (VI): artificial neural network modeling, Water Sci. Technol. 76 (2017) 3368–3378, https://doi.org/10.2166/wst.2017.501.

[156] C. Luo, Z. Tian, B. Yang, L. Zhang, S. Yan, Manganese dioxide/iron oxide/acid oxidized multi-walled carbon nanotube magnetic nanocomposite for enhanced hexavalent chromium removal, Chem. Eng. J. 234 (2013) 266–275, https://doi.org/10.1016/j.cej.2013.08.084.

[157] S. Wadhawan, A. Jain, J. Nayyar, S.K. Mehta, Role of nanomaterials as adsorbents in heavy metal ion removal from waste water: a review, J. Water Process Eng. 33 (2020), 101038, https://doi.org/10.1016/j.jwpe.2019.101038.

[158] V.K. Gupta, R. Chandra, I. Tyagi, M. Verma, Removal of hexavalent chromium ions using CuO nanoparticles for water purification applications, J. Colloid Interface Sci. 478 (2016) 54–62, https://doi.org/10.1016/j.jcis.2016.05.064.

[159] J.H. Lee, J.A. Park, H.G. Kim, J.H. Lee, S.H. Cho, K. Choi, K.W. Jung, S.Y. Lee, J.W. Choi, Most suitable amino silane molecules for surface functionalization of graphene oxide toward hexavalent chromium adsorption, Chemosphere 251 (2020), 126387, https://doi.org/10.1016/j.chemosphere.2020.126387.

[160] R.S. Zambare, P.R. Nemade, l P. re of, Colloids Surfaces A Physicochem. Eng. Asp. (2020), 125657, https://doi.org/10.1016/j.colsurfa.2020.125657.

[161] M.E. Mahmoud, M.M. Osman, H. Abdel-aal, G.M. Nabil, Microwave-assisted adsorption of Cr (VI), Cd (II) and Pb (II) in presence of magnetic graphene oxide-covalently functionalized-tryptophan nanocomposite, J. Alloys Compd. 823 (2020), 153855, https://doi.org/10.1016/j.jallcom.2020.153855.

[162] N. Kumar, M. Samarpita, Adsorption of Cr (VI) from aqueous solution on graphene oxide (GO) prepared from graphite : equilibrium , kinetic and thermodynamic studies, Appl. Water Sci. 10 (2020) 1–10, https://doi.org/10.1007/s13201-020-1142-2.

[163] S. Periyasamy, P. Manivasakan, C. Jeyaprabha, S. Meenakshi, N. Viswanathan, Fabrication of nano-graphene oxide assisted hydrotalcite/chitosan biocomposite: an efficient adsorbent for chromium removal from water, Int. J. Biol. Macromol. 132 (2019) 1068–1078, https://doi.org/10.1016/j.ijbiomac.2019.03.232.

[164] M.S. Samuel, J. Bhattacharya, S. Raj, N. Santhanam, H. Singh, N.D. Pradeep Singh, Efficient removal of Chromium(VI) from aqueous solution using chitosan grafted graphene oxide (CS-GO) nanocomposite, Int. J. Biol. Macromol. 121 (2019) 285–292, https://doi.org/10.1016/j.ijbiomac.2018.09.170.

[165] A. Sheikhmohammadi, S.M. Mohseni, B. Hashemzadeh, E. Asgari, R. Sharafkhani, M. Sardar, M. Sarkhosh, M. Almasiane, Fabrication of magnetic graphene oxide nanocomposites functionalized with a novel chelating ligand for the removal of Cr(VI): modeling, optimization, and adsorption studies, Desalination Water Treat. 160 (2019) 297–307, https://doi.org/10.5004/dwt.2019.24381.

[166] M. Serhan, M. Sprowls, D. Jackemeyer, M. Long, I.D. Perez, W. Maret, N. Tao, E. Forzani, Total iron measurement in human serum with a smartphone, AIChE Annu. Meet. Conf. Proc. (2019), https://doi.org/10.1039/x0xx00000x, 2019-Novem.

[167] M.E.A. Ali, Synthesis and adsorption properties of chitosan-CDTA-GO nanocomposite for removal of hexavalent chromium from aqueous solutions, Arab. J. Chem. 11 (2018) 1107–1116, https://doi.org/10.1016/j.arabjc.2016.09.010.

[168] P. Janik, B. Zawisza, E. Talik, R. Sitko, Selective adsorption and determination of hexavalent chromium ions using graphene oxide modified with amino silanes, Microchim. Acta 185 (2018) 1–8, https://doi.org/10.1007/s00604-017-2640-2.

[169] K. Zhang, H. Li, X. Xu, H. Yu, Synthesis of reduced graphene oxide/NiO nanocomposites for the removal of Cr(VI) from aqueous water by adsorption, Microporous Mesoporous Mater. 255 (2018) 7–14, https://doi.org/10.1016/j.micromeso.2017.07.037.

[170] M.E. Mahmoud, M.M. Osman, H. Abdel-Aal, G.M. Nabil, Microwave-assisted adsorption of Cr(VI), Cd(II) and Pb(II) in presence of magnetic graphene oxide-covalently functionalized-tryptophan nanocomposite, J. Alloys Compd. 823 (2020), 153855, https://doi.org/10.1016/j.jallcom.2020.153855.

[171] X. Lv, J. Xu, G. Jiang, J. Tang, X. Xu, Highly active nanoscale zero-valent iron (nZVI)–Fe3O4 nanocomposites for the removal of chromium(VI) from aqueous solutions, J. Colloid Interface Sci. 369 (2012) 460–469, https://doi.org/10.1016/j.jcis.2011.11.049.

[172] M.R. Samani, D. Toghraie, Removal of hexavalent chromium from water using polyaniline/wood sawdust/poly ethylene glycol composite: an experimental study, J. Environ. Heal. Sci. Eng. 17 (2019) 53–62, https://doi.org/10.1007/s40201-018-00325-y.

[173] M.S. Islam, W.S. Choi, B. Nam, C. Yoon, H.-J. Lee, Needle-like iron oxide@CaCO3 adsorbents for ultrafast removal of anionic and cationic heavy metal ions, Chem. Eng. J. 307 (2017) 208–219, https://doi.org/10.1016/j.cej.2016.08.079.

[174] N. Subedi, A. Lähde, E. Abu-Danso, J. Iqbal, A. Bhatnagar, A comparative study of magnetic chitosan (Chi@Fe3O4) and graphene oxide modified magnetic chitosan (Chi@Fe3O4GO) nanocomposites for efficient removal of Cr(VI) from water, Int. J. Biol. Macromol. 137 (2019) 948–959, https://doi.org/10.1016/j.ijbiomac.2019.06.151.

[175] R. Khosravi, G. Moussavi, M.T. Ghaneian, M.H. Ehrampoush, B. Barikbin, A.A. Ebrahimi, G. Sharifzadeh, Chromium adsorption from aqueous solution using novel green nanocomposite: adsorbent characterization, isotherm, kinetic and thermodynamic investigation, J. Mol. Liq. 256 (2018) 163–174, https://doi.org/10.1016/j.molliq.2018.02.033.

[176] A.E. Chávez-Guajardo, J.C. Medina-Llamas, L. Maqueira, C.A.S. Andrade, K.G.B. Alves, C.P. de Melo, Efficient removal of Cr (VI) and Cu (II) ions from aqueous media by use of polypyrrole/maghemite and polyaniline/maghemite magnetic nanocomposites, Chem. Eng. J. 281 (2015) 826–836, https://doi.org/10.1016/j.cej.2015.07.008.

[177] C. Luo, Z. Tian, B. Yang, L. Zhang, S. Yan, Manganese dioxide/iron oxide/acid oxidized multi-walled carbon nanotube magnetic nanocomposite for enhanced hexavalent chromium removal, Chem. Eng. J. 234 (2013) 256–265.

[178] R.S. Zambare, P.R. Nemade, Ionic liquid-modified graphene oxide sponge for hexavalent chromium removal from water, Colloids Surfaces A Physicochem. Eng. Asp. 609 (2021), 125657, https://doi.org/10.1016/j.colsurfa.2020.125657.

[179] Y. Tadjenant, N. Dokhan, A. Barras, A. Addad, R. Jijie, S. Szunerits, R. Boukherroub, Graphene oxide chemically reduced and functionalized with KOH-PEI for efficient Cr(VI) adsorption and reduction in acidic medium, Chemosphere 258 (2020), 127316, https://doi.org/10.1016/j.chemosphere.2020.127316.

[180] D. Zhai, B. Liu, Y. Shi, L. Pan, Y. Wang, W. Li, R. Zhang, G. Yu, Highly sensitive glucose sensor based on Pt nanoparticle/polyaniline hydrogel heterostructures, ACS Nano 7 (2013) 3540–3546, https://doi.org/10.1021/nn400482d.

[181] L. Tang, G.-M. Zeng, G.-L. Shen, Y.-P. Li, Y. Zhang, D.-L. Huang, Rapid detection of picloram in agricultural field samples using a disposable immunomembrane-based electrochemical sensor, Environ. Sci. Technol. 42 (2008) 1207–1212, https://doi.org/10.1021/es7024593.

[182] D. Saikia, Y.-H. Chen, Y.-C. Pan, J. Fang, L.-D. Tsai, G.T.K. Fey, H.-M. Kao, A new highly conductive organic-inorganic solid polymer electrolyte based on a di-ureasil matrix doped with lithium perchlorate, J. Mater. Chem. 21 (2011) 10542–10551.

[183] P.P. Deshpande, N.G. Jadhav, V.J. Gelling, D. Sazou, Conducting polymers for corrosion protection: a review, J. Coating Technol. Res. 11 (2014) 473–494, https://doi.org/10.1007/s11998-014-9586-7.

[184] V. Singh, D. Joung, L. Zhai, S. Das, S.I. Khondaker, S. Seal, Graphene based materials: past, present and future, Prog. Mater. Sci. 56 (2011) 1178–1271, https://doi.org/10.1016/j.pmatsci.2011.03.003.

[185] N. Wang, Y. Chen, J. Ren, X. Huang, X. Chen, G. Li, D. Liu, Electrically conductive polyaniline/polyimide microfiber membrane prepared via a combination of solution blowing and subsequent in situ polymerization growth, J. Polym. Res. 24 (2017), https://doi.org/10.1007/s10965-017-1198-3.

[186] A. Maity, Selective removal of toxic Cr (VI) from aqueous solution by adsorption combined with reduction at a magnetic nanocomposite surface, J. Colloid Interface Sci. (2017), https://doi.org/10.1016/j.jcis.2017.05.018.

[187] Y. Tian, H. Li, Y. Liu, G. Cui, Z. Sun, S. Yan, Morphology-dependent enhancement of template-guided tunable polyaniline nanostructures for the removal of Cr (VI), RSC Adv. 6 (2016) 10478–10486, https://doi.org/10.1039/c5ra25630e.

[188] D. Xu, S. Yan, W. Weng, R. Xiao, Cost effective nanofiber composite membranes for Cr(VI) adsorption with high durability, RSC Adv. 6 (2016) 44723–44731, https://doi.org/10.1039/c6ra00355a.

[189] Y. Gao, C. Chen, X. Tan, H. Xu, K. Zhu, Polyaniline-modified 3D-flower-like molybdenum disulfide composite for efficient adsorption/photocatalytic reduction of Cr(VI), J. Colloid Interface Sci. 476 (2016) 62–70, https://doi.org/10.1016/j.jcis.2016.05.022.

[190] K. Zhu, Y. Gao, X. Tan, C. Chen, Polyaniline-modified Mg/Al layered double hydroxide composites and their application in efficient removal of Cr(VI), ACS Sustain. Chem. Eng. 4 (2016) 4361–4369, https://doi.org/10.1021/acssuschemeng.6b00922.

[191] T. Wen, Q. Fan, X. Tan, Y. Chen, C. Chen, A. Xu, X. Wang, A core-shell structure of polyaniline coated protonic titanate nanobelt composites for both Cr(VI) and humic acid removal, Polym. Chem. 7 (2016) 785–794, https://doi.org/10.1039/c5py01721a.

[192] R. Karthik, S. Meenakshi, Adsorption study on removal of Cr(VI) ions by polyaniline composite, Desalination Water Treat. 54 (2015) 3083–3093, https://doi.org/10.1080/19443994.2014.909330.

[193] R. Karthik, S. Meenakshi, Removal of Cr(VI) ions by adsorption onto sodium alginate-polyaniline nanofibers, Int. J. Biol. Macromol. 72 (2015) 711–717, https://doi.org/10.1016/j.ijbiomac.2014.09.023.

[194] J. Wang, X. Yin, W. Tang, H. Ma, Combined adsorption and reduction of Cr(VI) from aqueous solution on polyaniline/multiwalled carbon nanotubes composite, Kor. J. Chem. Eng. 32 (2015) 1889, https://doi.org/10.1007/s11814-014-0395-6. –1895.

[195] J. Wang, X. Han, Y. Ji, H. Ma, Adsorption of Cr(VI) from aqueous solution onto short-chain polyaniline/palygorskite composites, Desalination Water Treat. 56 (2015) 356–365, https://doi.org/10.1080/19443994.2014.935805.

[196] M.A. Islam, M.J. Angove, D.W. Morton, Recent innovative research on chromium (VI) adsorption mechanism, Environ. Nanotechnol. Monit. Manag. 12 (2019), 100267, https://doi.org/10.1016/j.enmm.2019.100267.

[197] M. Nigam, S. Rajoriya, S.R. Singh, P. Kumar, Adsorption of Cr (VI) ion from tannery wastewater on tea waste: kinetics, equilibrium and thermodynamics studies, J. Environ. Chem. Eng. 7 (2019), 103188.

[198] M.A. Hashem, M.A. Momen, M. Hasan, M.S. Nur-A-Tomal, M.H.R. Sheikh, Chromium removal from tannery wastewater using Syzygium cumini bark adsorbent, Int. J. Environ. Sci. Technol. 16 (2019) 1395–1404.

[199] Q. Manzoor, A. Sajid, T. Hussain, M. Iqbal, M. Abbas, J. Nisar, Efficiency of immobilized Zea mays biomass for the adsorption of chromium from simulated media and tannery wastewater, J. Mater. Res. Technol. 8 (2019) 75–86, https://doi.org/10.1016/j.jmrt.2017.05.016.

[200] E. Mekonnen, M. Yitbarek, T.R. Soreta, Kinetic and thermodynamic studies of the adsorption of Cr (VI) onto some selected local adsorbents, S. Afr. J. Chem. 68 (2015) 45–52.

[201] J.R. Memon, S.Q. Memon, M.I. Bhanger, A. El-Turki, K.R. Hallam, G.C. Allen, Banana peel: a green and economical sorbent for the selective removal of Cr(VI) from industrial wastewater, Colloids Surf. B Biointerfaces 70 (2009) 232–237, https://doi.org/10.1016/j.colsurfb.2008.12.032.

[202] T. Dagnew, Z. Bantie, Process optimization of Cr (VI) removal from aqueous solution using activated orange peel for treatment of tannery wastewater, Ethiop. J. Sci. Technol. 16 (2023) 51–75.

[203] K.M.S. Sumathi, S. Mahimairaja, R. Naidu, Use of low-cost biological wastes and vermiculite for removal of chromium from tannery effluent, Bioresour. Technol. 96 (2005) 309–316, https://doi.org/10.1016/j.biortech.2004.04.015.

[204] A.A. El-Baz, I. Hendy, A.M. Dohdoh, M.I. Srour, Adsorption of high chromium concentrations from industrial wastewater using different agricultural residuals, J. Environ. Treat. Tech. 9 (2021) 122–138.

[205] G.M. Temesgen, G.S. Gebrie, Assessment of Cactus Biosorption Potential of Cr (VI) Ions Removal from Synthetic and Tannery Wastewater, 2022.

[206] E. Vunain, J.B. Njewa, T.T. Biswick, A.K. Ipadeola, Adsorption of chromium ions from tannery effluents onto activated carbon prepared from rice husk and potato peel by H3PO4 activation, Appl. Water Sci. 11 (2021) 150, https://doi.org/10.1007/s13201-021-01477-3.

[207] M. Barkat, D. Nibou, S. Chegrouche, A. Mellah, Kinetics and thermodynamics studies of chromium(VI) ions adsorption onto activated carbon from aqueous solutions, Chem. Eng. Process. Process Intensif. 48 (2009) 38–47, https://doi.org/10.1016/j.cep.2007.10.004.

[208] R. Ullah, W. Ahmad, M. Yaseen, M. Khan, M. Iqbal Khattak, B. Mohamed Jan, R. Ikram, G. Kenanakis, Fabrication of MNPs/rGO/PMMA composite for the removal of hazardous Cr(VI) from tannery wastewater through batch and continuous mode adsorption, Materials 14 (2021), https://doi.org/10.3390/ma14226923.

[209] A. Moges, T.T.I. Nkambule, J. Fito, The application of GO-Fe3O4 nanocomposite for chromium adsorption from tannery industry wastewater, J. Environ. Manag. 305 (2022), 114369, https://doi.org/10.1016/j.jenvman.2021.114369.

[210] E. Parthiban, N. Kalaivasan, S. Sudarsan, Dual responsive (pH and magnetic) nanocomposites based on Fe3O4@Polyaniline/itaconic acid: synthesis, characterization and removal of toxic hexavalent chromium from tannery wastewater, J. Inorg. Organomet. Polym. Mater. 30 (2020) 4677–4690, https://doi.org/10.1007/s10904-020-01602-w.

[211] P. Suksabye, P. Thiravetyan, W. Nakbanpote, S. Chayabutra, Chromium removal from electroplating wastewater by coir pith, J. Hazard Mater. 141 (2007) 637–644, https://doi.org/10.1016/j.jhazmat.2006.07.018.

[212] R. Ali Khan Rao, F. Rehman, M. Kashifuddin, Removal of Cr(VI) from electroplating wastewater using fruit peel of Leechi (Litchi chinensis), Desalination Water Treat. 49 (2012) 136–146, https://doi.org/10.1080/19443994.2012.708211.

[213] A.M. Farhan, M. Ahlam, Nida M. Salem, Al-Dujaili, H. Ammar, Awwad, biosorption studies of Cr(VI) ions from electroplating wastewater by walnut shell powder, Am. J. Environ. Eng. 2 (2012) 188–195, https://doi.org/10.5923/j.ajee.20120206.07.

[214] G. Moussavi, S. Talebi, Comparing the efficacy of a novel waste-based adsorbent with PAC for the simultaneous removal of chromium (VI) and cyanide from electroplating wastewater, Chem. Eng. Res. Des. 90 (2012) 960–966, https://doi.org/10.1016/j.cherd.2011.10.014.

[215] R. Kumar, N.R. Bishnoi, K. Bishnoi, Biosorption of chromium (VI) from aqueous solution and electroplating wastewater using fungal biomass, Chem. Eng. J. 135 (2008) 202–208.

[216] R. Kumar, D. Bhatia, R. Singh, N.R. Bishnoi, Metal tolerance and sequestration of Ni(II), Zn(II) and Cr(VI) ions from simulated and electroplating wastewater in batch process: kinetics and equilibrium study, Int. Biodeterior. Biodegrad. 66 (2012) 82–90, https://doi.org/10.1016/j.ibiod.2011.11.006.

[217] S. Chhikara, R. Dhankhar, Biosorption of Cr (VI) ions from electroplating industrial effluent using immobilized Aspergillus Niger biomass, J. Environ. Biol. 29 (2008) 773–778.

[218] S. Akar, B. Lorestani, S. Sobhanardakani, M. Cheraghi, O. Moradi, Surveying the efficiency of Platanus orientalis bark as biosorbent for Ni and Cr(VI) removal from plating wastewater as a real sample, Environ. Monit. Assess. 191 (2019) 373, https://doi.org/10.1007/s10661-019-7479-z.

[219] H. Ma, J. Yang, X. Gao, Z. Liu, X. Liu, Z. Xu, Removal of chromium (VI) from water by porous carbon derived from corn straw: influencing factors, regeneration and mechanism, J. Hazard Mater. 369 (2019) 550–560, https://doi.org/10.1016/j.jhazmat.2019.02.063.

[220] K.K. Garg, P. Rawat, B. Prasad, Removal of Cr (VI) and COD from electroplating wastewater by corncob based activated carbon, Int. J. Water Wastewater Treat. 1 (2015) 1. https://dx.doi.org/10.16966/ijwwt.102.

[221] W. Cai, Z. Li, J. Wei, Y. Liu, Synthesis of peanut shell based magnetic activated carbon with excellent adsorption performance towards electroplating wastewater, Chem. Eng. Res. Des. 140 (2018) 23–32, https://doi.org/10.1016/j.cherd.2018.10.008.

[222] X. Tao, X. Hu, Z. Wen, Y. Ming, J. Li, Y. Liu, R. Chen, Highly efficient Cr(VI) removal from industrial electroplating wastewater over Bi2S3 nanostructures prepared by dual sulfur-precursors: insights on the promotion effect of sulfate ions, J. Hazard Mater. 424 (2022), 127423, https://doi.org/10.1016/j.jhazmat.2021.127423.

[223] R. Zhao, Z. Zhou, X. Zhao, G. Jing, Enhanced Cr(VI) removal from simulated electroplating rinse wastewater by amino-functionalized vermiculite-supported nanoscale zero-valent iron, Chemosphere 218 (2019) 458–467, https://doi.org/10.1016/j.chemosphere.2018.11.118.

[224] J. Hu, G. Chen, I.M.C. Lo, Selective removal of heavy metals from industrial wastewater using maghemite nanoparticle: performance and mechanisms, J. Environ. Eng. 132 (2006) 709–715.

[225] A. Bukhari, I. Ijaz, H. Zain, U. Mehmood, M. Mudassir Iqbal, E. Gilani, A. Nazir, Introduction of CdO nanoparticles into graphene and graphene oxide nanosheets for increasing adsorption capacity of Cr from wastewater collected from petroleum refinery, Arab. J. Chem. 16 (2023), 104445, https://doi.org/10.1016/j.arabjc.2022.104445.